Ancient TL

www.ancienttl.org · ISSN: 2693-0935

Issue 37(2) - December 2019
https://doi.org/10.26034/la.atl.v37.i2

ISSN 0735-1348

Ancient TL

A periodical devoted to Luminescence and ESR dating

Department of Physics, East Carolina University, 1000 East 5th Street, Greenville, NC 27858, USA
http://ancienttl.org

December 2019, Volume 37 No.2

Ancient TL

Started by the late David Zimmerman in 1977

Ancient TL

'RCarb': Dose Rate Modelling of Carbonate-Rich Samples - an Implementation of *Carb* in R -

Sebastian Kreutzer,[1,*], Barbara Mauz,[2,3], Loïc Martin[1], Norbert Mercier[1]
[1]IRAMAT-CRP2A, UMR 5060, CNRS - Université Bordeaux Montaigne, France
[2]Department of Geography and Geology, University of Salzburg, Salzburg, Austria
[3]School of Environmental Sciences, University of Liverpool, Liverpool, United Kingdom

[*]Corresponding Author: sebastian.kreutzer@u-bordeaux-montaigne.fr

Received: July 30, 2019; in final form: November 21, 2019

Abstract

Geochemical conditions (e.g., pH-value, temperature, availability of CO_2) in carbonate-rich sedimentary environments lead to cementation processes, i.e., air or water in the pore space are substituted by mineral phases. Consequently, in such environments the conventional formalism of estimating the environmental dose rate from U, Th and K concentrations (pores are filling by air or water) cannot be overall correct. In 2008, Nathan & Mauz (2008) presented a model to account for dose-rate changes occurring when carbonate minerals replace air and water in the pore space between mineral grains. The underlying MATLAB® code (*Carb*) was later published by Mauz & Hoffmann (2014). Here we present an implementation of this tool using the statistical programming environment R. Our implementation does not alter the underlying model and its assumption but comes with an updated code basis published as R package under GPL-3 licence conditions.

Keywords: Luminescence dating; Dose rate; R

1. Motivation

Over the last decades the luminescence dating community has developed various software tools (cf. Kreutzer et al., 2017) to facilitate automised analytical workflows and processing of data from samples originating from sedimentary environments that underwent post-depositional changes with consequences for the dose-rate estimation. Some of these tools are likely to be used only occasionally, but nevertheless carefully collected and archived for the moment when they are needed. In contrast to good Bordeaux wine, sadly, software does not mature with age: Software that had worked perfectly in the past eventually renders itself unusable when needed. It was such an event that revealed the need for the creation of 'RCarb' (Kreutzer et al., 2019).

At the IRAMAT-CRP2A in Bordeaux, we processed carbonate-rich sediment samples using routine luminescence dating techniques (e.g., optically stimulated luminescence, Huntley et al., 1985), for which the ages were not in stratigraphic order. We hypothesised that this was caused by the replacement of pore water by carbonate minerals, which promotes dose-rate changes through time. To test this hypothesis, the work by Nathan & Mauz (2008) and Mauz & Hoffmann (2014) and the published MATLAB® software *Carb* seemed to offer a convenient starting point without the need to run a full simulation in *DosiVox* (Martin et al., 2015), which would be further complicated by the assumed post-depositional dose-rate alterations. Problems with running the code in an updated version of MATLAB® motivated us to translate it into **R** (R Core Team, 2019) and deploy it to the trapped-charge dating community as **R** package; henceforth named 'RCarb'. The implementation of 'RCarb' aimed at:

- Providing a version of *Carb* based on open-source software and published under GPL-3,
- updating and refitting the code basis to extend its availability to the community by another 5 to 10 years,
- supplementing *Carb* with an updated documentation of the code for developers as well as for end-users to facilitate the usage of the software,
- enabling future, community driven, developments by using the open-source repositories such as GitHub (https://github.com).

In the following, we outline the main implementation aspects of 'RCarb' and provide **R** code snippets (typed in monospace letters). *Carb* was designed to model dose rate through time for quartz grains $> 100\,\mu$m. Typically, these grains are etched in concentrated HF and, thereby, the external α-dose contribution is removed (Fleming, 1966, 1970) and does not need be considered for the modelling. However, not in all cases an etching of the grains is feasible or desired (e.g., a limited amount of material). To be able to consider the full radiation field for special sample cases, we additionally discuss the impact of α-radiation on the dose-rate modelling, simulated for grain diameters of $4\,\mu$m and $250\,\mu$m.

2. Implementation

The original MATLAB® program (Mauz & Hoffmann, 2014, their supplement) consists of 51 individual files in a single folder. These files represent the code necessary to run the model and to provide a graphical user interface (GUI). The files further comprise reference and example data, tests scripts and cached graphical and numerical output. MATLAB® and **R** are both numerical computation environments which mainly evaluate code during runtime. With some knowledge of the syntax differences, MATLAB® code can be translated easily into **R**. However, translating non-**R** code into a full **R** package requires substantial effort to meet the basic requirements of the Comprehensive R Archive Network (CRAN, https://cran.r-project.org) which is the central **R** package repository. In the following, we detail the implementation of *Carb* in 'RCarb' to provide a better understanding of the package structure and to highlight similarities and differences between the two programs.

2.1. Central premise and code structure

'RCarb' was designed with the intention to keep the original code recognisable, notwithstanding more efficient or elegant solutions would exist in **R**. The names of variables as well as large parts of the code structure remained almost identical to that presented in Nathan & Mauz (2008); Mauz & Hoffmann (2014). Basic MATLAB® functions were replaced by **R** equivalents and, consequently, a new syntax had to be adopted. Comments were added where they appeared to be necessary for the understanding of the code. Likewise, the code structure (Fig. 1) was modified and broken down into separate functions. Three of these functions are for internal use only and not accessible by the user (see below).

2.2. Reference and example data

In a first step, the file structure was reorganised to meet the CRAN **R** package requirements. Reference data, which are (1) water/carbonate correction factors for β and γ-radiation after Nathan & Mauz (2008), (2) β-dose attenuation factors after Mejdahl (1979), (3) and example data taken from Mauz & Hoffmann (2014), were imported into **R** and integrated as package (example) data. In the **R** terminal they are now accessible via, e.g., data(Example_Data). Additionally, appropriate documentation was added for the reference as well as the example data. The reference data are used extensively by the internal functions, while the example data serve as test dataset to the user.

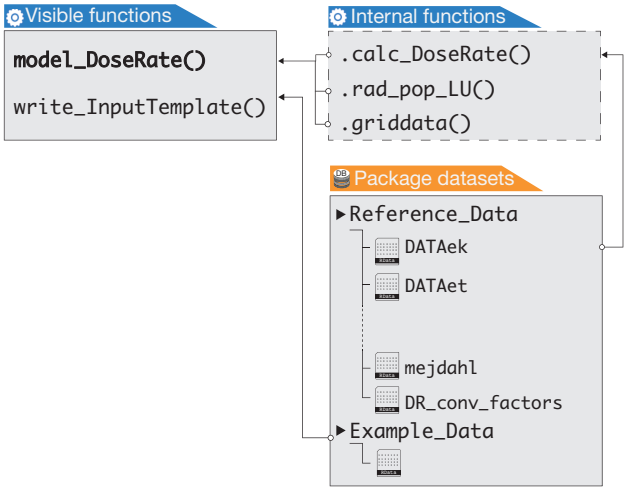

Figure 1: The threefold structure of the R package 'RCarb'. In its current state, the package has only two visible functions. Additional internal functions (e.g., .calc_DoseRate()) are not meant for user interaction. These functions are not displayed to the user and they show no documentation (but are supplied with comments in the code). Package datasets are (1) reference data needed for the calculation, e.g., mejdahl, which refers to the β-dose attenuation dataset published by Mejdahl (1979) and (2) example datasets from *Carb*. For further details see main text.

2.3. The modelling core

The second step consisted of a line by line translation of the MATLAB® code and removal of unused code lines. *Carb* is started in MATLAB® by executing carb_2007a.m which then internally calls the files daterlu1.m and rad_pop_LU.m. Other files, e.g., those preceding with the word 'test', are not needed to run the program and have been removed. In 'RCarb', the internal workhorse function is called .calc_DoseRate() and it is based on the file daterlu1.m from *Carb*. The function rad_pop_LU() is the **R** equivalent of rad_pop_LU.m and .griddata(), and provides a match to the MATLAB® function griddata for the interpolation of irregular gridded data. Actually, an equivalent does not exist in base **R** so that we had to implement the package 'interp' (Gebhardt et al., 2019). All three functions are not exported, i.e. they do not appear in the help page index and are not directly visible to the user.[1] The new

[1]Such internal functions in **R** packages mainly serve the package developers and do not usually provide a documented interface. Although such functions can still be called, e.g., RCarb:::.calc_DoseRate(), they should not be employed by the user without having a profound reason (and knowledge). Besides, CRAN itself does not allow calling such "non-exported" functions from inside other packages.

entry point for the user is the function `model_DoseRate()`. This function has a full documentation and provides terminal and graphical output very similar to *Carb* (see Sec. 3 for examples).

2.4. Graphical user interface and miscellaneous

In a third step, the MATLAB® code providing the GUI was removed. This code only works in MATLAB® and cannot be translated easily into **R**. As a consequence, `'RCarb'` is light-weighted, uses base **R** syntax and does not depend heavily on other **R** packages. The reduced overhead may simplify and encourage the code inspection by others. However, to improve the usability, in particular for users not familiar with **R**, we provide a new (separate) GUI to `'RCarb'` through the **R** `'RLumShiny'` package (Burow et al., 2016, 2019) (cf. Fig. 3, see below).

In the last step, code example and reference data were compiled as **R** package and submitted to CRAN. Although `'RCarb'` does not depend on other packages of the 'RLum' family (e.g., `'RLumShiny'`), it is hosted and developed through the same version control hosting service GitHub (https://github.com/R-Lum/RCarb). Thereby, `'RCarb'` benefits from established development workflows and testing routines ensuring robust and smooth execution on the three major platforms (*Windows*®, *Linux*™, *macOS*®) as detailed by Kreutzer et al. (2017).

2.5. Enhancements and code modifications

Besides code structure alterations required by the translation from MATLAB® to **R**, two additional modifications slightly changed the calculation output in comparison to *Carb*. The first difference concerns a bug: In case values for ^{238}U and ^{234}U/^{238}U activity ratios were provided, erroneously the same water correction factor (for the concept of those factors cf. Zimmerman, 1971) applied to correct the β-dose rate was also used for the γ-dose rate. `'RCarb'` now applies the correct factors, i.e. the β-dose correction factors to the β-dose rate and the γ-correction factors to the γ-dose rate.

The second modification relates to the dose-rate conversion factors. The latest version of *Carb* uses dose-rate conversion factors downloaded from the ENSDF database as of January 16, 2002 (Roger Nathan, personal communication, July 24, 2019; archived database versions available at http://www.nndc.bnl.gov/ensarchivals/). These factors are slightly different to published values used by the trapped-charge dating community (e.g., Adamiec & Aitken, 1998). Considering the overall uncertainties of the dose-rate modelling for carbonate-rich samples, the differences are, however, negligible. Nevertheless, to provide a consistent and up-to-date approach, `'RCarb'` supports, on top of the dataset from *Carb*, now named `'Carb2007'`, the selection of dose-rate conversion factors published by Adamiec & Aitken (1998), Guérin et al. (2011), and Liritzis et al. (2013). These datasets are part of the package reference data (cf., `Reference_Data`, Fig. 1). The default setting is `'Carb2007'` to yield modelling results consistent with the original *Carb*. To see the implemented datasets type `RCarb::Reference_Data$DR_conv_factors` in your **R** terminal.

3. Running examples

Before outlining two examples for how to run `'RCarb'` in the **R** terminal, we wish to remind the reader that these software examples can provide only a first impression. The manuscript remains static, while `'RCarb'` may evolve. Consequently, our examples are kept short and we point the reader to the always up-to-date HTML-document shipped alongside the package (a so called 'vignette') via CRAN.

3.1. Example 1 - example dataset

Users who are not familiar with **R** should first look at the example section in the package manual. It provides a good start (type `?model_DoseRate` in the **R** terminal) and `'RCarb'` includes the example data of *Carb*. The code lines in listing 1 first load the package itself before loading the example data into the working environment. Subsequently, line 6 (listing 1) calls row 14 from the table with the example data (without modifying the function arguments). This example is similar to the one shown in Mauz & Hoffmann (2014) (their Fig. 4).

Listing 1: Running 'RCarb' using the package example dataset.

```
1 ##load example data and example data
2 library(RCarb)
3 data("Example_Data", envir = environment())
4
5 ##model dose rate for sample LV107
6 model_DoseRate(data = Example_Data[14,])
```

The terminal and graphical output (Fig. 2) is very similar to the one provided by *Carb*. Our example output (listing 2) shows that the conventional age calculation, i.e. without considering the pore filling by carbonate, overestimates the age by ca 15 %.

Listing 2: Typical 'RCarb' terminal output.

```
[model_DoseRate()]

Sample ID:              LV107
Equivalent dose:        53 ± 2 Gy
Diameter:               215 µm
MC runs error estim.: 100
------------------------------------------------
Age (conv.):        149.73 ± 10.667 ka
Age (new):          130.642 ± 7.754 ka

Dose rate (conv.): 0.354 ± 0.018 Gy/ka
Dose rate (onset): 0.499 ± 0.027 Gy/ka
Dose rate (final): 0.361 ± 0.017 Gy/ka
------------------------------------------------
```

3.2. Example 2 - own dataset

Using own data requires the replacement of the input data (in listing 1: `data = Example_Data[14,]`) by an own `data.frame`. Because this particular user interaction likely increases the chance to crash the function and then becoming a frustrating experience, we aimed at minimising the probability of such events. In the next example (listing 3), after loading `'RCarb'`, the function `write_InputTemplate()` first generates a template CSV-file (if the argument `file` is left blanc, a template `data.frame` is returned to the **R** terminal). The CSV-file can be filled easily with every spreadsheet software (e.g., *Excel*®) and re-imported into **R** (code lines 9–12). In the final call of `model_DoseRate()`, `data = Example_Data[14,]` it is replaced by `data = own_data`. The subsequent calculation does not require user interaction but may take a while.

Listing 3: Working with own data.

```
1  ##load package
2  library(RCarb)
3
4  ##write template CSV
5  write_InputTemplate(
6         file = 'YOUR PATH/MyData.csv')
7
8  ##import after filled with external program
9  own_data <- read.table(
10        file = 'YOUR PATH/MyData.csv',
11        header = TRUE,
12        sep = ',')
13
14 ##run model
15 model_DoseRate(data = own_data)
```

3.3. Remarks

If the input table has more than one row, `model_DoseRate()` automatically iterates over all rows, i.e. multiple samples. Entries leading the function to fail are skipped and removed from the output. The uncertainties are estimated using a resampling approach similar to *Carb*. By default, the function uses 100 Monte Carlo (MC) runs (argument `n.MC`). More MC runs likely increase the quality of the error estimate but also the computation time.

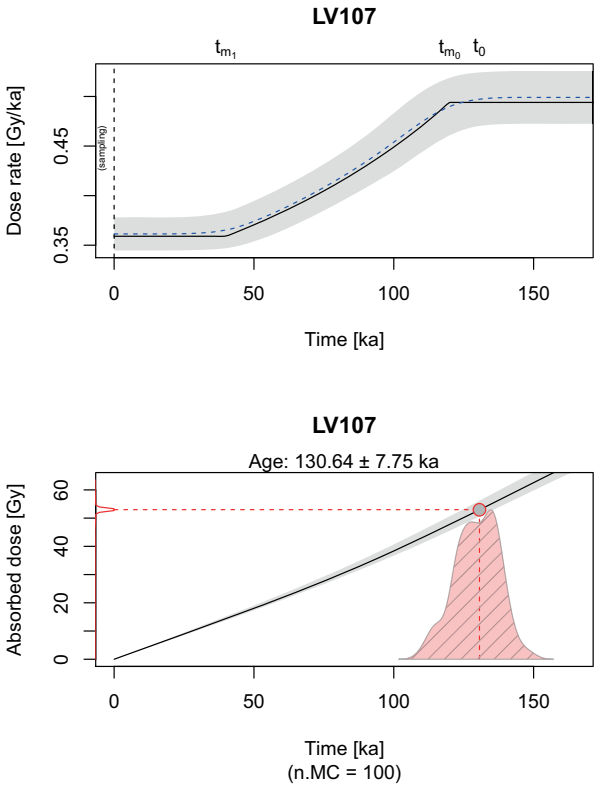

Figure 2: Graphical output of 'RCarb' for a sample from the example dataset (here: HD107, which corresponds to the sample LV107 shown in Mauz & Hoffmann 2014, their Fig. 4).

The *upper plot* reads from right to left and displays the dose-rate evolution over time with t_0 the burial time, t_{m_0} the inset of the cementation and t_{m_1} the completion of the cementation. The grey shaded error indicates the error margins determined by MC runs. The dashed blue line provides a quality measure for the number of the MC runs. If the dashed blue line closely matches the solid line, the number of MC runs have been sufficient. Please note that the match will be never perfect.

The *lower plot* shows the absorbed dose over time indicating the resulting age (red lines). Dashed lines and grey shaded area indicate error margins. The superlinear evolution of the absorbed dose is a consequence of the modelling and no display error.

4. Limitations and further considerations

Carb (and so `'RCarb'`) does not model the dose-rate effect of α-radiation. Instead, *Carb* was written to model post-depositional dose-rate alteration by which the sediment is subject to gradual infilling of carbonate in the pore space. Within the range of sedimentary deposits suitable for luminescence dating, those containing sand-sized components are most likely to be affected by this process. As a consequence, *Carb* was designed for sand-sized quartz grains and these are usually treated with HF (cf. Porat et al., 2015; Duval et al., 2018, for recent discussions) in order to remove the α-radiation affected outer rim of the grains. However, what can we do with a sample that has not been etched?

The travel range of (natural) α-particles in silicate-rich sediments is a few micrometres so that only those grains situated in close vicinity to the emitter receive an external α-dose. If the pore space between the grain and emitter, typically occupied by air or water, is gradually filled with carbonate instead of air or water, the α-dose changes over time. Therefore, we provide additional information on the α-correction factors needed to estimate the environmental dose rate and calculate the luminescence age. In the appendix (Tables A1–A4) we list α-correction factors following the style

Figure 3: Screenshot of the Shiny app 'RCarb App' providing a graphical user interface to the package 'RCarb'. (1) Data import and calculation menu, (2) central data table with input and output data and (3) graphical output similar to Fig. 2.

of Table 1 in Mauz & Hoffmann (2014) for different water- and carbonate-mass fractions for a grain size of 250 μm (Tables A1–A2) and 4 μm (Tables A3–A4). Values for the U-series and the Th-series are quoted for each grain size, and the lower rows of each table list the corresponding 2σ uncertainties.

These new α-correction factors were determined by simulations with the software *GEANT4* (Agostinelli et al., 2003) with a setup similar to Martin et al. (2014). Our sediment composition used for the simulation followed Nathan & Mauz (2008) who relied on Garrels & Mackenzie (1971). Thus, the sediment was dominated by quartz with a significant contribution of feldspar represented by the following chemical composition: SiO_2 (66 %), Al_2O_3 (18 %), Fe_2O_3 (6 %) and $KAlSi_3O_8$ (10 %)[2]. The initial density (without water and carbonate) was set to 1.8 g cm^{-3}. $CaCO_3$ was used to simulate carbonate.

The obtained values seem to show a similar trend for both silt and sand (simulated grain diameters: 4 μm and 250 μm) but are characterised by increasing uncertainty with decreasing grain size owing to the very low probability for an α-particle to hit the (simulated) grain. Additional simulations would improve the precision of the quoted values. Unfortunately, this would require access to a large computer cluster over several months. Such resources were not available for this article and, besides, more precise factors do not necessarily improve the overall accuracy of the dose-rate modelling.

Additionally, we performed simulations (data not shown) for the case of detrital carbonate, i.e. the carbonate is part of the sediment components (i.e., no cementation). The resulting α-correction factors, averaged for U- and Th-series, estimate at 1.36–1.37 for reasonable water contents inferior or equal to 20 %. Such values are close to the values reported by Martin et al. (2014) for a clay sediment matrix. We did not include those correction factors into `'RCarb'` since it would require extensive modification of the code basis, unjustified by the significant uncertainties of the correction factors (cf. Tables A1–A4). Instead, if needed, the listed factors can be used to roughly estimate the impact of the pore filling process on the luminescence ages in particular environments.

[2]We tested different feldspar phases but found no significant differences.

5. Graphical user interface (GUI)

We provide a simple GUI via the **R** `'RLumShiny'` (cf. Burow et al., 2016). To run the GUI the user needs to install the two packages `'RCarb'` and `'RLumShiny'`. Alternatively, an installation of `'RLumShiny'` will force `'RCarb'` to install, but not *vice versa*. The GUI can be started in the **R** terminal via (listing 4):

Listing 4: Starting the Shiny app 'RCarb'.

```
##load package
library(RLumShiny)

##start app
app_RLum(app = 'RCarb')
```

In case a valued colleague runs a local *Shiny* server (`https://shiny.rstudio.com/`) in your institution, the 'RCarb App' can be started like every other web-based application. We do not provide the 'RCarb App' via the *Shiny* hosting service (`http://www.shinyapps.io`), since

the few free calculation hours would be quickly exhausted by a few users and the commercial service is rather costly.

'RCarb App' (Fig. 3) is split into three sub-windows: (1) The import and settings panel, (2) the modifiable spreadsheet and (3) a graphical output similar to the one presented in Fig. 2. Clicking on the table rows (Fig. 3-2) switches the graphical output, i.e. (3) shows the figures corresponding to the selection in (2). The central table supports various standard user interactions such as copy & paste, deletion and insertion of rows. Please note that the modelling feature set of `'RCarb'` determines the functionality of "RCarb App".

6. Conclusion and outlook

We presented a new **R** package called `'RCarb'`. This package is a translation of the MATLAB® software *Carb* introduced by Nathan & Mauz (2008) and Mauz & Hoffmann (2014). While the package is new, it does not enhance or substantially modify the features set by *Carb*. However, with `'RCarb'`, we provide a refitted open-source and open-access solution to the community. The code is maintained via the platform GitHub and we invite interested readers to contribute to further developments. A graphical user interface to `'RCarb'` is available through the **R** package `'RLumShiny'`.

Finally, we wish to remind the reader about limits and assumptions underpinning the *Carb* model. They are detailed in Nathan & Mauz (2008) and Mauz & Hoffmann (2014).

`'RCarb'` is available

- as **R** package via CRAN: https://CRAN.R-project.org/package=RCarb,
- as development version under https://github.com/R-Lum/RCarb,
- and we host a package webpage at https://r-lum.github.io/RCarb/.

Acknowledgments

We are grateful to André Oliveira Sawakuchi for a constructive review. This work would not have been possible without Roger Nathan and his pioneering work on *Carb*. Roger also provided valuable remote support to this manuscript to clarify technical details. The LaScArBx financed the work of SK, LM and NM. LaScArBx is a research programme supported by the ANR (ANR-10-LABX-52).

References

Adamiec, G. and Aitken, M. J. *Dose-rate conversion factors: update*. Ancient TL, 16(2): 37–50, 1998. URL http://ancienttl.org/ATL_16-2_1998/ATL_16-2_Adamiec_p37-50.pdf.

Agostinelli, S., Allison, J., Amako, K., Apostolakis, J., Araujo, H., Arce, P., Asai, M., Axen, D., Banerjee, S., Barrand, G., Behner, F., Bellagamba, L., Boudreau, J., Broglia, L., Brunengo, A., Burkhardt, H., Chauvie, S., Chuma, J., Chytracek, R., Cooperman, G., Cosmo, G., Degtyarenko, P., Dell'Acqua, A., Depaola, G., Dietrich, D., Enami, R., Feliciello, A., Ferguson, C., Fesefeldt, H., Folger, G., Foppiano, F., Forti, A., Garelli, S., Giani, S., Giannitrapani, R., Gibin, D., Gómez Cadenas, J. J., González, I., Gracia Abril, G., Greeniaus, G., Greiner, W., Grichine, V., Grossheim, A., Guatelli, S., Gumplinger, P., Hamatsu, R., Hashimoto, K., Hasui, H., Heikkinen, A., Howard, A., Ivanchenko, V., Johnson, A., Jones, F. W., Kallenbach, J., Kanaya, N., Kawabata, M., Kawabata, Y., Kawaguti, M., Kelner, S., Kent, P., Kimura, A., Kodama, T., Kokoulin, R., Kossov, M., Kurashige, H., Lamanna, E., Lampén, T., Lara, V., Lefebure, V., Lei, F., Liendl, M., Lockman, W., Longo, F., Magni, S., Maire, M., Medernach, E., Minamimoto, K., Mora de Freitas, P., Morita, Y., Murakami, K., Nagamatu, M., Nartallo, R., Nieminen, P., Nishimura, T., Ohtsubo, K., Okamura, M., O'Neale, S., Oohata, Y., Paech, K., Perl, J., Pfeiffer, A., Pia, M. G., Ranjard, F., Rybin, A., Sadilov, S., Di Salvo, E., Santin, G., Sasaki, T., Savvas, N., Sawada, Y., Scherer, S., Sei, S., Sirotenko, V., Smith, D., Starkov, N., Stoecker, H., Sulkimo, J., Takahata, M., Tanaka, S., Tcherniaev, E., Safai Tehrani, E., Tropeano, M., Truscott, P., Uno, H., Urban, L., Urban, P., Verderi, M., Walkden, A., Wander, W., Weber, H., Wellisch, J. P., Wenaus, T., Williams, D. C., Wright, D., Yamada, T., Yoshida, H., and Zschiesche, D. *Geant4—a simulation toolkit*. Nuclear Instruments and Methods in Physics Research Section A: Accelerators, Spectrometers, Detectors and Associated Equipment, 506(3): 250–303, 2003. doi: 10.1016/S0168-9002(03)01368-8.

Burow, C., Wolpert, U. T., and Kreutzer, S. *RLumShiny: 'Shiny' Applications for the R Package 'Luminescence'*. CRAN, version 0.2.2, 2019. URL https://CRAN.R-project.org/package=RLumShiny. Developer version on GitHub: https://github.com/tzerk/RLumShiny.

Burow, C., Kreutzer, S., Dietze, M., Fuchs, M. C., Fischer, M., Schmidt, C., and Brückner, H. *RLumShiny - A graphical user interface for the R Package 'Luminescence'*. Ancient TL, 34: 22–32, 2016. URL http://author.ecu.edu/cs-cas/physics/Ancient-Timeline/upload/ATL_34-2_Burow_p22-32.pdf.

Duval, M., Guilarte, V., Campa n a, I., Arnold, L. J., Miguens, L., Iglesias, J., and Gonz a lez Sierra, S. *Quantifying hydrofluoric acid etching of quartz and feldspar coarse grains based on weight loss estimates: implication for ESR and luminescence dating studies*. Ancient TL, 36: 1–14, 2018. URL http://ancienttl.org/ATL_36-1_2018/ATL_36-1_Duval_p1-14.pdf.

Fleming, S. J. *Study of Thermoluminescence of Crystalline Extracts From Pottery*. Archaeometry, 9(1): 170–173, 1966. doi: 10.1111/j.1475-4754.1966.tb00916.x.

Fleming, S. J. *Thermoluminescent dating: refinement of the quartz inclusion method*. Archaeometry, 12(2): 133–143, 1970. doi: 10.1111/j.1475-4754.1970.tb00016.x.

Garrels, R. M. and Mackenzie, F. T. *Evolution of Sedimentary Rocks*, 1971.

Gebhardt, A., Bivand, R., and Sinclair, D. *interp: Interpolation Methods*, 2019. URL https://CRAN.R-project.org/package=interp. R package version 1.0-32.

Guérin, G., Mercier, N., and Adamiec, G. *Dose-rate conversion factors: update*. Ancient TL, 29(1): 5–9, 2011. URL http://ancienttl.org/ATL_29-1_2011/ATL_29-1_Guerin_p5-8.pdf.

Huntley, D. J., Godfrey-Smith, D. I., and Thewalt, M. L. W. *Optical dating of sediments*. Nature, 313(5998): 105–107, 1985. doi: 10.1038/313105a0.

Kreutzer, S., Burow, C., Dietze, M., Fuchs, M. C., Fischer, M., and Schmidt, C. *Software in the context of luminescence dating: status, concepts and suggestions exemplified by the R package 'Luminescence'*. Ancient TL, 35(2): 1–11, 2017. URL http://author.ecu.edu/cs-cas/physics/Ancient-Timeline/upload/ATL_35-2_Kreutzer_p1-11.pdf.

Kreutzer, S., Nathan, R. P., and Mauz, B. *RCarb: Dose Rate Modelling of Carbonate-Rich Samples*. CRAN, version 0.1.3, 2019. URL https://CRAN.R-project.org/package=RCarb. Developer version on GitHub: https://github.com/R-Lum/RCarb.

Liritzis, I., Stamoulis, K., Papachristodoulou, C., and Ioannides, K. *A Re-Evaluation of Radiation Dose-Rate Conversion Factors*. Mediterranean Arhaeology and Archaeometry, 12: 1–15, 2013.

Martin, L., Mercier, N., and Incerti, S. *Geant4 simulations for sedimentary grains in infinite matrix conditions: The case of alpha dosimetry*. Radiation Measurements, 70: 39–47, 2014. doi: 10.1016/j.radmeas.2014.09.003.

Martin, L., Incerti, S., and Mercier, N. *DosiVox: Implementing Geant 4-based software for dosimetry simulations relevant to luminescence and ESR dating techniques* . Ancient TL, 33(1): 1–10, 2015. URL http://ancienttl.org/ATL_33-1_2015/ATL_33-1_Martin_p1-10.pdf.

Mauz, B. and Hoffmann, D. *What to do when carbonate replaced water: Carb, the model for estimating the dose rate of carbonate-rich samples*. Ancient TL, 32(2): 24–32, 2014. URL http://www.ecu.edu/cs-cas/physics/Ancient-Timeline/upload/ATL_32_2_Mauz.pdf.

Mejdahl, V. *Thermoluminescence dating: beta-dose attenuation in quartz grains*. Archaeometry, 21: 61–72, 1979. doi: 10.1111/j.1475-4754.1979.tb00241.x.

Nathan, R. P. and Mauz, B. *On the dose-rate estimate of carbonate-rich sediments for trapped charge dating*. Radiation Measurements, 43(1): 14–25, 2008. doi: 10.1016/j.radmeas.2007.12.012.

Porat, N., Faerstein, G., Medialdea, A., and Murray, A. S. *Re-examination of common extraction and purification methods of quartz and feldspar for luminescence dating*. Ancient TL, 33 (1): 22–30, 2015. URL http://ancienttl.org/ATL_33-1_2015/ATL_33-1_Porat_p22-30.pdf.

R Core Team. *R: A Language and Environment for Statistical Computing*. Vienna, Austria, 2019. URL https://r-project.org.

Zimmerman, D. W. *Thermoluminescent dating using fine grains from pottery.* Archaeometry, 13(1): 29–52, 1971. doi: 10.1111/j.1475-4754.1971.tb00028.x.

Reviewer

André Oliveira Sawakuchi

Appendix

A1: α-radiation correction factors - 250 μm

Table A1: U-series correction factor x for α-radiation for water and carbonate to sediment mass ratios (m_s: sediment mass; m_c: carbonate mass; m_w: water mass). Values in *italic* do not exist in nature. The lower table quotes corresponding 2σ uncertainties.

U-series — α-radiation — 250 μm

m_w/m_s	m_c/m_s			
	0.00	**0.04**	**0.20**	**1.00**
0	-	0.99	1.03	1.02
0.04	1.36	1.18	1.08	*1.03*
0.20	1.38	1.31	1.19	*1.07*
1.00	1.37	*1.36*	*1.32*	*1.19*
corresponding 2σ uncertainty				
0	-	38.2 %	5.8 %	2.5 %
0.04	29.6 %	15.7 %	4.8 %	*2.1 %*
0.20	8.7 %	4.4 %	3.0 %	*2.2 %*
1.00	3.0 %	*2.2 %*	*2.0 %*	*2.1 %*

Table A2: Th-series correction factor x for α-radiation for water and carbonate to sediment mass ratios (m_s: sediment mass; m_c: carbonate mass; m_w: water mass). Values in *italic* do not exist in nature. The lower table quotes corresponding 2σ uncertainties.

Th-series — α-radiation — 250 μm

m_w/m_s	m_c/m_s			
	0.00	**0.04**	**0.20**	**1.00**
0	-	0.96	1.01	1.01
0.04	1.38	1.17	1.07	*1.03*
0.20	1.36	1.29	1.18	*1.07*
1.00	1.36	*1.34*	*1.30*	*1.19*
corresponding 2σ uncertainty				
0	-	36.0 %	8.9 %	2.5 %
0.04	18.0 %	18.5 %	4.6 %	*3.9 %*
0.20	6.3 %	5.4 %	4.1 %	*3.2 %*
1.00	3.5 %	*3.8 %*	*4.5 %*	*3.4 %*

A2: α-radiation correction factors - 4 μm

Table A3: U-series correction factor x for α-radiation for water and carbonate to sediment mass ratios (m_s: sediment mass; m_c: carbonate mass; m_w: water mass). Values in *italic* do not exist in nature. The lower table quotes corresponding 2σ uncertainties.

U-series — α-radiation — 4 μm

m_w/m_s	m_c/m_s			
	0.00	**0.04**	**0.20**	**1.00**
0	-	1.38	0.99	1.03
0.04	1.62	1.00	1.36	*1.06*
0.20	1.43	1.42	1.12	*1.04*
1.00	1.42	*1.41*	*1.37*	*1.20*
corresponding 2σ uncertainty				
0	-	240.0 %	68.8 %	27.8 %
0.04	256.6 %	183.2 %	45.9 %	*22.0 %*
0.20	69.1 %	48.5 %	37.6 %	*23.9 %*
1.00	37.6 %	*21.9 %*	*20.0 %*	*19.3 %*

Table A4: Th-series correction factor x for α-radiation for water and carbonate to sediment mass ratios (m_s: sediment mass; m_c: carbonate mass; m_w: water mass). Values in *italic* do not exist in nature. The lower table quotes corresponding 2σ uncertainties.

Th-series — α-radiation — 4 μm

m_w/m_s	m_c/m_s			
	0.00	**0.04**	**0.20**	**1.00**
0	-	0.88	1.08	1.06
0.04	1.41	0.97	1.04	*1.05*
0.20	1.43	1.33	1.19	*1.07*
1.00	1.36	*1.36*	*1.34*	*1.21*
corresponding 2σ uncertainty				
0	-	313.9 %	56.5 %	20.5 %
0.04	212.5 %	149.8 %	49.8 %	*22.1 %*
0.20	62.7 %	40.6 %	30.6 %	*18.7 %*
1.00	27.6 %	*17.2 %*	*18.5 %*	*17.1 %*

Ancient TL

Luminescence as a Relative Dating Tool: Part A – Theory

Edmund G. Highcock,[1,2] Amber G.E. Hood,[3,*] Jean-Luc Schwenninger[4]

[1] Department of Physics, Chalmers University of Technology, Gothenburg, Sweden
[2] Research & Development, Greenbyte, Östra Hamngaten 16, Gothenburg, Sweden
[3] Department of Geology, Lund University, Lund, Sweden
[4] Research Laboratory for Archaeology and the History of Art, University of Oxford, Oxford, UK

[*]Corresponding Author: amber.hood@geol.lu.se

Received: June 14, 2019; in final form: December 12, 2019

Abstract

A formula is derived for calculating relative numerical ages of ceramic vessels using optically stimulated luminescence (OSL). These relative numerical ages may be generated when the standard absolute numerical ages cannot be determined; this is usually because a component of the dose rate such as the external dose rate cannot be measured or deduced. The error associated with this relative age formula is derived. It is shown that, where external dose rate information is unavailable, the error in the relative age that results from this lack of information is much smaller than the equivalent error in the absolute age.

Keywords: OSL dating, relative dating, museum material, ceramics, archaeology

1. Introduction

An undisputed accomplishment of luminescence dating has been the calculation of numerical ages for archaeological assemblages, most frequently based upon ceramic or sediment dating. Indeed, the application of luminescence dating has significantly impacted how we look at, and understand, past human activity. Yet luminescence can also be used as a *relative* numerical dating technique, whence it is possible to establish typological and chronological sequences within archaeological material and create a floating, relative typological framework for the material studied.

In general, numerical dating (whether OSL, radiocarbon, or other) produces an *absolute* age; that is, it results in an age which is a known number of years before the present day, and which allows the associated event (e.g. use/manufacture) to be assigned a calendar date. By contrast, relative dating (e.g. stratigraphy) does not produce a numerical age (absolute or otherwise), unless it is linked to another chronology, whether derived by historical or scientific methods. In this paper we discuss the creation of a *relative numerical* chronology. Like a traditional relative chronology, this numerical relative chronology allows us to assign a sequence to ancient events, without placing them on a calendar. Like a standard numerical chronology, we calculate a numerical age for each sample; this numerical age does not measure the number of years before present, but it does allow the formulation of statements like "this sample is twice as old as that one". Throughout this paper, we will refer to numerical methods that produce a calendar age (radiocarbon, standard OSL) as "absolute" methods, and to any methods (numerical or otherwise) that do not produce a calendar age as "relative" methods. To distinguish between the relative numerical method presented here and methods such as stratigraphy, we refer to the latter as "non-numerical relative dating" or "traditional relative dating" methods.

Previously, relative OSL dating has not been carried out for two reasons: first, in cases where access to recently excavated field material is forthcoming for luminescence dating, using the technique as a relative dating method is not necessary as the additional components required to calculate an absolute age will be available. Secondly, owing to the associated costs of luminescence analysis as a relative dating technique, alternative relative dating techniques, such as seriation, would be the more accepted option in many cases. However, there are clear areas of research where using luminescence as a relative dating tool would be of benefit to the archaeologist: for example, ceramic assemblages

in museums, whose provenance and chronology are uncertain (particularly when used in combination with the minimum extraction technique (MET) which is a method for obtaining optically stimulated luminescence (OSL) dates from museum materials; Hood & Schwenninger, 2015). For such material, a set of relative luminescence dates might well provide significant new insights, and perhaps even be the only robust way of establishing their relative chronology. The reasons for needing to rely upon museum material, rather than recently excavated material are varied, but include political and geographical disruptions which render access to an original excavation site impossible.

Many museum pieces were acquired in an era when detailed recording of provenance and archaeological context was rare, often with specimens being bought from antiquities dealers with no indication of the true find-spot of a piece, other than a broad regional location. Often this would happen to entire classes of vessels, those that were the more prized, probably owing to a particular characteristic of the ware, and in turn significant information was lost. A particular case in point is the Predynastic Egyptian Decorated Ware, or D-Ware, one of nine wares classified by Petrie in his Corpus of Prehistoric Pottery (Petrie, 1921). Although Petrie (whose recording methods were arguably the best of his generation) along with his peers excavated a large number of such vessels for museum collections, a large number were also acquired by museums through other means (e.g purchase) to add to their collections, and often without verified provenance.

Without their origin being known (and having been well cleaned prior to display), these vessels lack a crucial piece of information for determining an absolute luminescence date: the external dose rate ($\dot{D}_{ext}$), which can be obtained using original sediment adhering to the vessel. Without the $\dot{D}_{ext}$ measurement, only a relative date can be achieved by taking the equivalent dose (D_e) and dividing it by the internal dose rate ($\dot{D}_{int}$), rather than dividing it by the sum of $\dot{D}_{ext}$ and $\dot{D}_{int}$. While the lack of information about $\dot{D}_{ext}$ will mean that this relative date can deviate significantly from the true absolute age of the pot, the relative date may be used to determine the relative sequence of the ceramics in a manner similar to traditional relative dating techniques such as seriation, that is, these dates will help determine the sequence of the vessels. This relative date would depend on the assumptions that $\dot{D}_{ext}$ is both small compared to $\dot{D}_{int}$ (often the case for ceramic material) and similar for all the ceramics being studied. The second assumption may be justified on a variety of grounds, for example the ceramics come from one context; the ceramics come from contexts constructed from common building materials; the ceramics come from contexts with the same geology; the ceramics comes from a region where the natural background radiation has been measured across that region and shown to have little variation. The merit of this assumption must be argued on a case-by-case basis; in this paper we study a group of ceramics from several similar (radiometrically speaking) contexts at a single site.

This paper is accompanied by a second paper (Hood et al., 2019), which we refer to as Part B. This work, Part A, presents a derivation of the formulae for obtaining both a relative luminescence age and the associated relative error. Part B, which follows directly, presents a case study on determining the relative age using OSL dating, carried out on a group of ancient Egyptian ceramics.

2. Formal derivation of a relative age formula and associated error

In order to accurately apply luminescence as a relative dating technique, it is essential to determine how to calculate the approximate relative age of vessels using only the D_e and $\dot{D}_{int}$ measurements, as well as how to construct an estimate of the error associated with this calculation, which results from the fact that $\dot{D}_{ext}$ is neglected.

To derive the approximation and associated error, we must start from a mathematical expression for the relative age. To formulate such an expression we temporarily assume knowledge of all the parameters, including the external dose rate, that are required to derive hypothetical (absolute) numerical ages for each vessel. We then define the relative age of two vessels to be the hypothetical (absolute) numerical age of one divided by the hypothetical (absolute) numerical age of the other.

Having defined this relative age, we make an approximation of it by using asymptotic theory, and identifying certain parameters which we expect to be small (we will estimate them and verify that they are small subsequently). In common with standard asymptotic approaches, we wish to derive an approximation that tends to the original expression in the limit that the parameters become infinitely small. When (as is typically the case) the parameters are finite, there is an error associated with the approximation whose size we can estimate.

Mathematically, the relative age, R, of two vessels is defined as:

$$R \equiv \frac{A_1}{A_2}, \tag{1}$$

where A_1 and A_2 are the hypothetical (absolute) numerical ages of the two individual vessels respectively. Now,

$$A_1 = \frac{D_{e,1}}{\dot{D}_{int,1} + \dot{D}_{ext,1}} \tag{2}$$

and

$$A_2 = \frac{D_{e,2}}{\dot{D}_{int,2} + \dot{D}_{ext,2}}, \tag{3}$$

where $D_{e,1}$, $\dot{D}_{int,1}$ and $\dot{D}_{ext,1}$ are the equivalent dose, the internal dose rate and the external dose rate, respectively, for the first vessel and $D_{e,2}$, $\dot{D}_{int,2}$ and $\dot{D}_{ext,2}$ are the same measurements for the second vessel. Therefore,

$$\frac{A_1}{A_2} = \frac{D_{e,1}}{D_{e,2}} \frac{\dot{D}_{int,2} + \dot{D}_{ext,2}}{\dot{D}_{int,1} + \dot{D}_{ext,1}}. \tag{4}$$

If $\dot{D}_{ext,1}$ and $\dot{D}_{ext,2}$ (i.e. $\dot{D}_{ext}$) were known, we would know the exact relative age of the two vessels. However,

even though these values are unknown, it is possible to calculate an approximate relative age for both of the vessels, and, additionally, an estimation of the error associated with that approximation. There are three assumptions required: first, that $\dot{D}_{int}$ is similar for both vessels; secondly, that $\dot{D}_{ext}$ is similar for both vessels; thirdly, that for both vessels $\dot{D}_{ext}$ is smaller than $\dot{D}_{int}$.

More formally, we can define three parameters ε_I, ε_E and δ as follows:

$$\varepsilon_I \equiv \dot{D}_{int,2} - \dot{D}_{int,1} \implies \dot{D}_{int,2} = \dot{D}_{int,1} + \varepsilon_I, \tag{5}$$

$$\varepsilon_E \equiv \dot{D}_{ext,2} - \dot{D}_{ext,1} \implies \dot{D}_{ext,2} = \dot{D}_{ext,1} + \varepsilon_E, \tag{6}$$

$$\delta \equiv \frac{\dot{D}_{ext,1}}{\dot{D}_{int,1}} \implies \dot{D}_{ext,1} = \delta \dot{D}_{int,1}, \tag{7}$$

and we further assume that these parameters are small, that is,

$$\left|\frac{\varepsilon_I}{\dot{D}_{int,1}}\right| \ll 1, \left|\frac{\varepsilon_E}{\dot{D}_{ext,1}}\right| \ll 1, \delta \ll 1. \tag{8}$$

The meaning of these parameters, and the justification for assuming that all three are small, will be discussed below.

Now ε_I and ε_E can be substituted directly into the equation for the relative age (4):

$$\frac{A_1}{A_2} = \frac{D_{e,1}}{D_{e,2}} \frac{\dot{D}_{int,1} + \dot{D}_{ext,1} + \varepsilon_I + \varepsilon_E}{\dot{D}_{int,1} + \dot{D}_{ext,1}} \tag{9}$$

$$= \frac{D_{e,1}}{D_{e,2}} \left(1 + \frac{\varepsilon_I + \varepsilon_E}{\dot{D}_{int,1} + \dot{D}_{ext,1}}\right) \tag{10}$$

$$= \frac{D_{e,1}}{D_{e,2}} \left(1 + \frac{\varepsilon_I}{\dot{D}_{int,1} + \dot{D}_{ext,1}} + \frac{\varepsilon_E}{\dot{D}_{int,1} + \dot{D}_{ext,1}}\right). \tag{11}$$

Note that no approximations have been made up to this point, that is, the three assumptions have not yet been utilised.

At this point, it is possible to simply approximate the relative age as $D_{e,1}/D_{e,2}$, in which case the error would be given by the last two terms of equation (11), assuming, of course, that ε_I and ε_E are both small. However, is it possible to improve upon this estimate as follows.

First, the definition of δ is substituted into equation (11):

$$\frac{A_1}{A_2} = \frac{D_{e,1}}{D_{e,2}} \left(1 + \frac{\varepsilon_I}{\dot{D}_{int,1}(1+\delta)} + \frac{\varepsilon_E}{\dot{D}_{int,1}(1+\delta)}\right). \tag{12}$$

The ratio δ is now assumed to be small, which allows the following approximation to be made (using a Taylor series):

$$\frac{1}{1+\delta} \approx 1 - \delta \tag{13}$$

which means that

$$\frac{A_1}{A_2} \approx \frac{D_{e,1}}{D_{e,2}} \left(1 + \frac{\varepsilon_I}{\dot{D}_{int,1}}(1-\delta) + \frac{\varepsilon_E}{\dot{D}_{int,1}}(1-\delta)\right) \tag{14}$$

and therefore

$$\frac{A_1}{A_2} \approx \frac{D_{e,1}}{D_{e,2}} \left(1 + \frac{\varepsilon_I}{\dot{D}_{int,1}} - \frac{\varepsilon_I}{\dot{D}_{int,1}}\delta + \frac{\varepsilon_E}{\dot{D}_{int,1}}(1-\delta)\right). \tag{15}$$

However,

$$1 + \frac{\varepsilon_I}{\dot{D}_{int,1}} = \frac{\dot{D}_{int,2}}{\dot{D}_{int,1}}, \tag{16}$$

so

$$\frac{A_1}{A_2} \approx \frac{D_{e,1}}{D_{e,2}} \left(\frac{\dot{D}_{int,2}}{\dot{D}_{int,1}} - \frac{\varepsilon_I}{\dot{D}_{int,1}}\delta + \frac{\varepsilon_E}{\dot{D}_{int,1}}(1-\delta)\right). \tag{17}$$

It can be seen that the second term in this equation ($\varepsilon_I \delta / \dot{D}_{int,1}$) is second order, being the product of two small parameters. Furthermore, we note also that while δ is positive definite, both ε_I and ε_E can be either positive or negative. Thus, when estimating the error, the second term would have to be added to the third term in quadrature: assuming δ is sufficiently small, we may safely drop this second term, meaning that

$$\frac{A_1}{A_2} \approx \frac{D_{e,1}}{D_{e,2}} \frac{\dot{D}_{int,2}}{\dot{D}_{int,1}} \left(1 + \frac{\varepsilon_E}{\dot{D}_{int,1}} \frac{\dot{D}_{int,1}}{\dot{D}_{int,2}}(1-\delta)\right). \tag{18}$$

Equation (18) demonstrates that the relative age can be approximated by

$$R \equiv \frac{A_1}{A_2} \approx \frac{D_{e,1}}{D_{e,2}} \frac{\dot{D}_{int,2}}{\dot{D}_{int,1}} \tag{19}$$

with a relative error given by:

$$\frac{1}{R} \frac{\varepsilon_E}{\dot{D}_{int,2}}(1-\delta). \tag{20}$$

Rearranging equation (19), it can be seen that

$$R \equiv \frac{A_1}{A_2} \approx \frac{D_{e,1}/\dot{D}_{int,1}}{D_{e,2}/\dot{D}_{int,2}}, \tag{21}$$

and comparing this equation with (4), it can be seen that the approximation of the relative age of two vessels is simply effected by neglecting $\dot{D}_{ext}$, the external dose rate. However, the important point is that the relative error in this relative age is significantly smaller than the relative error in the individual absolute ages that could be calculated by neglecting $\dot{D}_{ext}$.

The relative deviation (which results from neglecting $\dot{D}_{ext}$) in the absolute age (of, for example, the first vessel) is given by

$$\frac{D_{e,1}/\dot{D}_{int,1} - D_{e,1}/\left(\dot{D}_{int,1} + \dot{D}_{ext,1}\right)}{D_{e,1}/\left(\dot{D}_{int,1} + \dot{D}_{ext,1}\right)} \tag{22}$$

$$= \frac{1/\dot{D}_{int,1} - 1/\left(\dot{D}_{int,1}(1+\delta)\right)}{1/\left(\dot{D}_{int,1}(1+\delta)\right)} \tag{23}$$

$$= \delta. \tag{24}$$

3. Estimating the uncertainty of the approximate relative age

The relative deviations in the relative and absolute ages can now be compared by obtaining estimates for the values of δ and $\varepsilon_E/\dot{D}_{int,2}$.

It should be noted that though we are comparing the specific case of two vessels, in general ε_E can be thought of as the variation of $\dot{D}_{ext}$ within a studied ceramic assemblage, and $\dot{D}_{int,2}$ can be considered as an order of magnitude estimate of $\dot{D}_{int}$, and δ is an estimate of the typical ratio between $\dot{D}_{ext}$ and $\dot{D}_{int}$. Thus, if we denote the mean of the internal dose rate measurements as μ_I, the mean of the external dose rate measurements as μ_E, and the uncertainty of the external dose rate measurements as σ_E, we may write:

$$\delta \sim \frac{\mu_E}{\mu_I} \tag{25}$$

and

$$\frac{1}{R}\frac{\varepsilon_E}{\dot{D}_{int,2}}(1-\delta) \sim \frac{1}{R}\frac{\sigma_E}{\mu_I}(1-\delta). \tag{26}$$

The quantity μ_I is easily calculated since the internal dose rates in this analysis are assumed to be known. The value of R will of course vary with each vessel. In contrast, since the external dose rates for the vessels in question are assumed to be unknown, some additional source of information will be necessary to determine μ_E and σ_E. Since these are only required to estimate the error, and do not affect the age calculation itself, order-of-magnitude approximations will be sufficient: a set of values taken from a similar assemblage, or surveys of the region, may be used (e.g. following Zink et al., 2012).

As an example, we consider the first application of this methodology in Part B of this paper (Hood et al., 2019). As no measurements for $\dot{D}_{ext}$ existed for the vessels under consideration, μ_E and σ_E were estimated using existing values from the literature and from measurements taken from material at a different site (of similar age and composition). This was justifiable, because the values for $\dot{D}_{ext}$ measurements across a wide geographical region around the site were very similar to one another. In this work the actual values were $\sigma_E \sim 0.108$, $\mu_I \sim 1.61$, $\mu_E \sim 0.726$, and $R \sim 1$ on average, meaning that the relative error estimates were

$$\frac{1}{R}\frac{\sigma_E}{\mu_I}(1-\delta) \sim 3.6\%, \tag{27}$$

for the relative ages and

$$\delta \sim \frac{\mu_E}{\mu_I} \sim 45\% \tag{28}$$

for the absolute ages.

In summary, this section shows that the relative age of two vessels is obtained (equation 19) by dividing the D_e of one vessel by that of another, and then dividing by the associated ratio of the $\dot{D}_{int}$ measurements for each vessel; effectively, this is calculating the ratio of the two absolute ages while neglecting $\dot{D}_{ext}$. Furthermore, it demonstrates that when neglecting $\dot{D}_{ext}$ the relative error in the *absolute* age for a given vessel is ∼45%, but the relative error in the *relative* age for a given vessel, is only ∼3.6% (an error which is small when added in quadrature to the relative error of the equivalent dose measurement).

4. How to calculate a relative age sequence

In Section 2, we derived a formula for the relative age, R, of two vessels. We now lay out briefly a program for calculating the relative ages of a group of vessels (whose external dose rates satisfy the conditions given in Section 1).

1. For each of the vessels, determine the equivalent dose (D_e) and the internal dose rate ($\dot{D}_{int}$) in the usual way.

2. Select a vessel to be used as a reference vessel. This vessel may be selected for a number of reasons, for example:

   (a) Low uncertainty on its D_e and $\dot{D}_{int}$ measurements (which will reduce the uncertainty across the other relative ages).

   (b) The vessel has a known absolute age, e.g. through a known $\dot{D}_{ext}$, or by associated radiocarbon or historical chronologies.

   (c) The vessel has an age that is central to the sequence.

3. Calculate the relative age of every vessel in the sequence. If we define the equivalent dose of our selected reference vessel to be $D_{e,ref}$ and the internal dose rate of the reference vessel to be $\dot{D}_{int,ref}$, then for all the other vessels, the relative age R of the vessel may be calculated as follows:

$$R = \frac{D_e}{D_{e,ref}}\frac{\dot{D}_{int,ref}}{\dot{D}_{int}} \tag{29}$$

4. The uncertainty in the relative age is composed of two parts: the error that comes from neglecting $\dot{D}_{ext}$, given in equation (26), and the error that comes from uncertainties in $\dot{D}_{int}$ and D_e. These can be combined in quadrature, as they are uncorrelated with each other. Thus if ε_R is defined to be the absolute uncertainty in the relative age, and ε_D the absolute uncertainty in the equivalent dose, we may write:

$$\frac{\varepsilon_R}{R} \sim \sqrt{\left(\frac{\varepsilon_I}{\dot{D}_{int}}\right)^2 + \left(\frac{\varepsilon_{I,ref}}{\dot{D}_{int,ref}}\right)^2 + \left(\frac{\varepsilon_D}{D_e}\right)^2 + \left(\frac{\varepsilon_{D,ref}}{D_{e,ref}}\right)^2 + \left(\frac{1}{R}\frac{\sigma_E}{\mu_I}(1-\delta)\right)^2} \tag{30}$$

where σ_E, the estimated variation in the external dose rate, and μ_I, the average internal dose rate, are defined in the previous section.

5. Discussion

Luminescence dating can be used as a relative dating method to establish a relative chronology for an archaeological assemblage. This paper has outlined the mathematical

formula with which to calculate this age, and the error associated with determining the sequence.

Using OSL dating as a relative dating tool would be most beneficial for work on museum collections, or in any case where the original contextual information for an assemblage is lacking. Additionally, it would be adventageous in detecting forgeries.

It may be the case that some parts of the external dose rate, for example the cosmic dose rate ($\dot{D}_{cos}$), are known, and indeed that there may be other more unusual external doses, coming from, for example, a storage location since excavation, x-ray imaging, CT-scanning, and so on. In this case, the above analysis may be simply adapted as follows: all known doses should be included in the calculation of $\dot{D}_{int,1}$, $\dot{D}_{int,2}$, and of course μ_I, with μ_E and σ_E being the estimated mean and uncertainty of the remaining unknown dose received by each vessel.

Finally, once a relative sequence has been calculated, if one member of the sequence has an associated absolute date calculated by other means (i.e. radiocarbon dating), the whole sequence can then be anchored and the absolute ages of all the vessels can be derived (within error bars). This powerful result seems somewhat counterintuitive; however, it is merely a result, principally, of assuming that the variation in the external dose rate is small compared to the size of the internal dose rate (a condition often true for pottery), and holds as long as this is the case (it should be noted, additionally, that any errors in the single absolute date will apply systematically to the whole sequence).

6. Conclusion

In summary, this paper has provided a framework for implementing luminescence dating as a relative dating method. While the usefulness of this technique will be heavily dependent upon individual assemblages and the quality of available relative dating methods, further potential for this technique is significant in the museum world and further advances in the study of archaeological assemblages can be made as a result.

Acknowledgments

This research was completed owing to the generous support of the G.A. Wainwright Fund; the Clarendon Fund; Merton College, Oxford; and Brasenose College, Oxford.

References

Hood, A. and Schwenninger, J.-L. *The Minimum Extraction Technique: A New Sampling Methodology for Optically Stimulated Luminescence Dating of Museum Ceramics*. Quaternary Geochronology, 30: 381–385, 2015.

Hood, A., Köhler, E., Highcock, E., and Schwenninger, J.-L. *Luminescence as a Relative Dating Tool: Part B – Application*. Ancient TL, 37(2): 14–20, 2019.

Petrie, W. *Corpus of Prehistoric Pottery and Palettes*. British School of Archaeology in Egypt, London, 1921.

Zink, A., Susino, G., Porto, E., and Huffman, T. *Direct OSL Dating of Iron Age Pottery from South Africa: Preliminary Dosimetry Investigations*. Quaternary Geochronology, 8: 1–9, 2012.

Reviewer

Daniel Richter

Ancient TL

Luminescence as a Relative Dating Tool: Part B – Application

Amber G.E. Hood,[1,*] E. Christiana Köhler,[2] Edmund G. Highcock,[3,4] Jean-Luc Schwenninger[5]

[1] Department of Geology, Lund University, Lund, Sweden
[2] Institute for Egyptology, University of Vienna, Vienna, Austria
[3] Department of Physics, Chalmers University of Technology, Gothenburg, Sweden
[4] Research & Development, Greenbyte, Gothenburg, Sweden
[5] Research Laboratory for Archaeology and the History of Art, University of Oxford, Oxford, UK

*Corresponding Author: amber.hood@geol.lu.se

Received: June 14, 2019; in final form: December 13, 2019

Abstract

This paper discusses the applicability of using luminescence as a *relative numerical* dating tool. Examples of when such an application may be useful include the dating of museum materials for which original external dose rate information is no longer obtainable. Without the external dose rate, it is still possible to obtain the relative ages of two or more vessels, which is particularly useful when attempting to ascertain typological sequences or chronological implications of archaeological assemblages. This paper presents a case study on determining the relative numerical age using optically stimulated (OSL) dating, carried out on a group of ancient Egyptian ceramics. This paper is preceded directly by Part A (Highcock et al., 2019) of this article, which presents a derivation of the formulae for obtaining both a relative luminescence age and the associated relative error.

Keywords: OSL dating, relative dating, museum material, Egyptian archaeology, Naqada Culture, Egyptian chronology, Predynastic Egypt, Early Dynastic Egypt, ceramics.

1. Introduction

Luminescence dating can be used to determine relative ages for ceramic assemblages, even in the absence of external dose rate ($\dot{D}_{ext}$) measurements, which may not always be available. The most obvious example of the usefulness of relative dating by luminescence are studies of material from museum collections, for which no original sedimentary material is available for the determination of $\dot{D}_{ext}$; for such (often unprovenanced) museum specimens the knowledge of relative chronological sequences is beneficial.

The companion paper (Part A, Highcock et al., 2019) of this article presents a derivation of the formulae that can be used to obtain relative ages using luminescence, as well as its associated relative error. Here, in Part B, we now present a case study, using an assemblage of wavy-handled vessels and wine jars from the Predynastic and Early Dynastic Periods of Egyptian history (c. 3300 – 3000 BC).

As discussed further in Part A, this new approach necessitates somewhat non-standard nomenclature when referring to ages. To summarise: what is generally known as a numerical age, which is given as a number of years before present or as a calendar date, we refer to as an *absolute* numerical age. What is generally known as a relative age, as determined by, for example, seriation, we continue to refer to as a relative age. The calculation presented in Part A defines a *relative numerical* age. Like a standard (absolute) numerical age, the relative numerical age is expressed as a number, and that number can be used to make quantitative statements like "this vessel is twice as old as that vessel." Like a traditional relative age, the relative numerical age cannot (without additional evidence) be related to a number of years before present, or a calendar date.

2. The data set

To illustrate how OSL can be used as a relative numerical dating technique, and thus be used to further improve

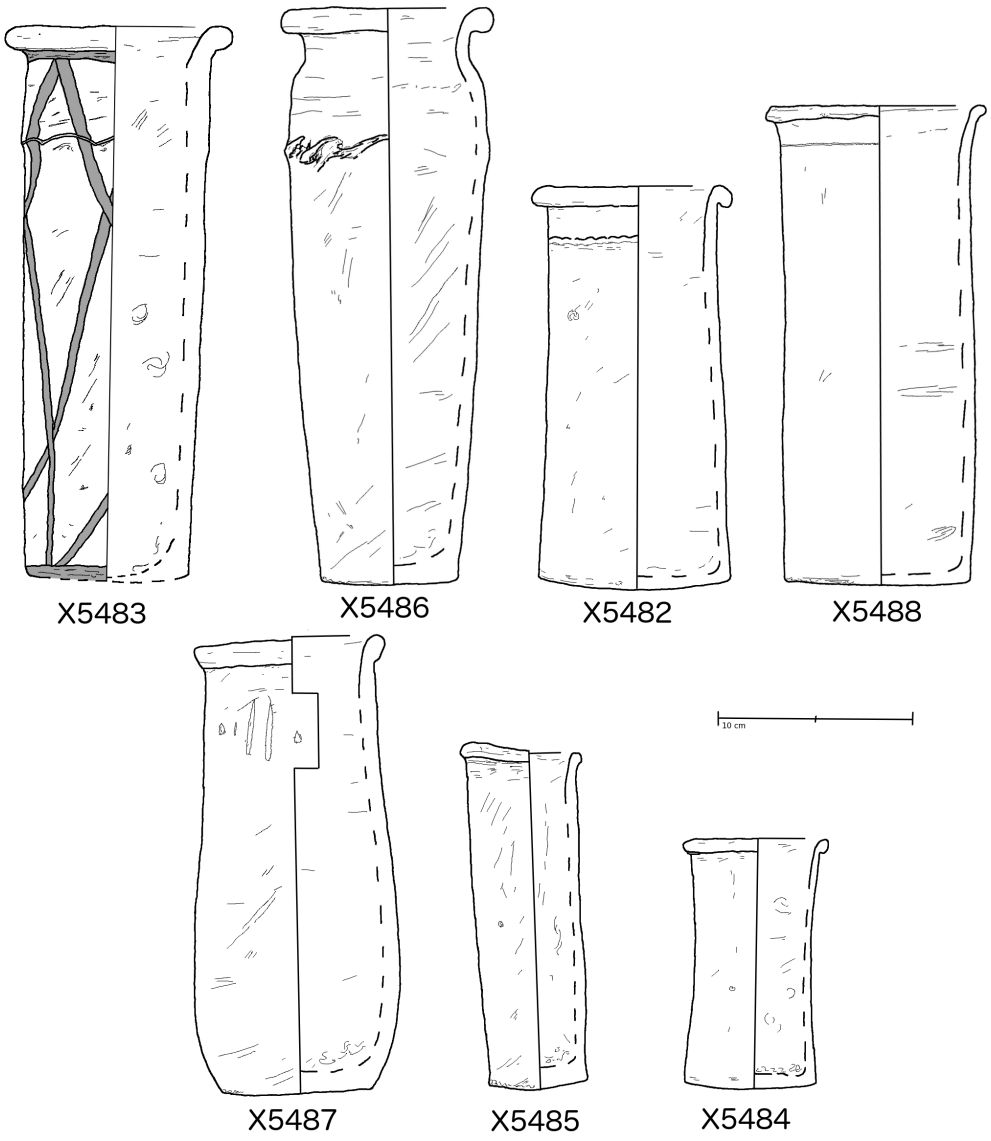

Figure 1. Wavy-handled vessels from Turah used in this study. Vessels appear in their relative chronological order (oldest to youngest left to right and top to bottom).

our understanding of the chronology of archaeological assemblages, two sets of objects were examined: a selection of seven wavy-handled vessels from Predynastic and Early Dynastic Egypt from the site of Turah (Figure 1), and three wine jars—two archaeologically complete specimens from Turah, and one sherd from Hierakonpolis, each inscribed with a *serekh* or pot mark (Figure 2).

The Turah material offered an almost complete relative sequence of wavy-handled vessels for study. This assemblage is a prime set of material on which to demonstrate how OSL can be used as a relative numerical dating technique, because, with regard to ceramic typology, it is one of the most well-understood ceramic assemblages from early Egypt. Wavy-handled vessels provided the backbone of Petrie's ceramic sequencing system, developed in the late 19th century, which is still a tool for relative dating of Egypt's earliest pottery today (Petrie, 1899, 1901). The wavy-handled vessel type is observed across Pre- and Early Dynastic Egypt, and was fundamental in defining the Naqada Culture and establishing the archaeological chronology for the Predynastic and Early Dynastic phases of Egyptian history (here we follow the Naqada Culture as defined in Hendrickx (1996, 2006); see also Kaiser (1957); Köhler (2004); Köhler & Smythe (2004); Köhler (2013) and further discussion of terminological inconsistencies in Köhler & Thalmann (2014) and Hood (2017)). It continues across several archaeological phases spanning the Predynastic and Early Dynastic Periods. While other vessel types came and went, the wavy-handled vessel continued to develop. Petrie originally based his seriation of Predynastic and Early Dynas-

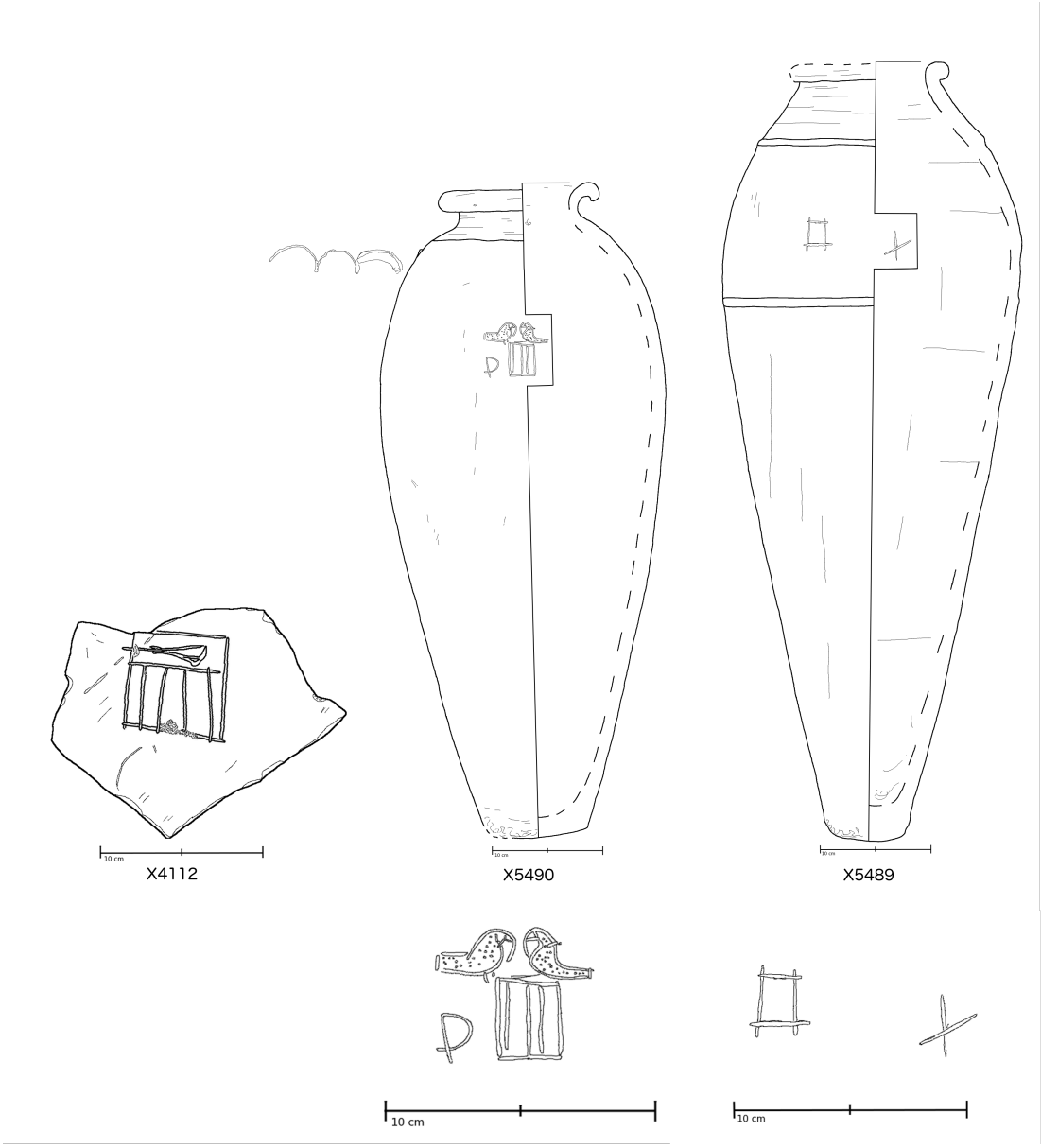

Figure 2. Wine jars used in this study. X4112, the sherd, is from Hierakonpolis; X5489 and X5490 are from Turah. Also shown at the bottom of the figure are enlarged drawings of the pot marks appearing on X5489 and X5490.

tic Egyptian ceramics on this vessel type, noting the gradual change in vessel form from the bulbous vessel with functional wavy handle, to the elongated cylindrical shape with a fine wavy decoration, which no longer served as a functional handle. Indeed, the final known development of this vessel type no longer has a wavy decoration at all, and is a smaller and rougher cylindrical form when compared to its predecessors (Köhler, 2004). The seven wavy-handled/cylindrical vessels selected for OSL analysis here represent an excellent typological assemblage of this particular ware, spanning the Naqada IIIA to Naqada IIIC2 periods.

In addition to the wavy-handled vessels, the three wine jars were also examined with luminescence. Two of these had an inscribed *serekh* (pre-fired engraved marks on the vessel in the form of a rectangle, containing a symbol/name of historical figures). These vessels, owing to their vessel index (Köhler & Smythe, 2004), their typology and their inscribed historical information (i.e. a *serekh*, which can often be directly linked to known figures or time period within the historical chronology) (Van Den Brink, 2001, 1996), make prime candidates for illustrating the applicability of OSL as a relative numerical dating technique.

Unfortunately, with regard to the wavy-handled vessels, although it is known that all these ceramics studied here come from the site of Turah, the exact provenance of each piece was not recorded. No original depositional sediment was attached to the Turah material, and given that the site is now under military occupation, it is at present unlikely that absolute numerical luminescence dates will be obtained for this material in the future.

Table 1. Relative ages of vessels from Turah and Hierakonpolis. Relative ages of the wavy-handled/cylindrical vessels and the wine jars from Turah and Hierakonpolis. The table shows the equivalent dose (D_e) and the total internal dose rate ($\dot{D}_{int}$) for both coarse grain (CG) and fine grain (FG) material as available. Also shown are the relative numerical ages of each pot, relative to a reference vessel (X5486, see text), again for CG and FG. Finally, the table also shows a combined age, which is either the CG or FG age if only one is available, or a combination of both CG and FG results made by using kernel density estimation. It is this combined age which is displayed in Figure 3. Also given is the ratio N of accepted aliquots to total aliquots. Element concentrations used to determine $\dot{D}_{int}$ are available in Hood (2017). The following rejection criteria were applied: test dose error: $\leq$ 20%; recycling ratio: $\leq$20%; recuperation: $\leq$5%; IRSL/OSL ratio: $\leq$15% (Note that these rejection criteria are slightly higher than 'standard' rejection criteria. This is owing to MET sampling producing very few aliquots for some samples and therefore in order to work with these samples a more flexible rejection criteria was implemented. Further details can be found in Hood (2017)). Uncertainties in D_e are calculated, using the central age model, from non-rejected aliquots; uncertainties in $\dot{D}_{int}$, which incorporate the uncertainty in elemental analysis, were determined by DRAC (Durcan et al., 2015); uncertainty in the relative ages is calculated using the uncertainties in D_e, the uncertainties in $\dot{D}_{int}$, and the uncertainty that results from the relative age formula as detailed in Part A (Highcock et al., 2019).

Site	Vessel	N		D_e (Gy)		$\dot{D}_{int}$ (Gy/ka)		Date Relative to X5486 (expressed as a ratio)		Combined Date Relative to X5486 (as a ratio)
		CG	FG	CG	FG	CG	FG	CG	FG	
Turah	X5482	N/A	6/6	N/A	12.05 $\pm$ 0.61	N/A	1.68 $\pm$ 0.07	N/A	1.18 $\pm$ 0.09	1.18 $\pm$ 0.09
Turah	X5484	1/8	N/A	8.09 $\pm$ 1.68	N/A	1.38 $\pm$ 0.07	N/A	0.86 $\pm$ 0.19	N/A	0.86 $\pm$ 0.19
Turah	X5486	3/7	6/6	9.60 $\pm$ 0.78	11.27 $\pm$ 0.40	1.41 $\pm$ 0.08	1.84 $\pm$ 0.07	1.00 $\pm$ 0.11	1.00 $\pm$ 0.07	1.00 $\pm$ 0.06
Turah	X5488	3/6	N/A	10.17 $\pm$ 1.36	N/A	N/A	1.63 $\pm$ 0.06	N/A	1.02 $\pm$ 0.15	1.02 $\pm$ 0.15
Turah	X5489	2/14	5/6	8.73 $\pm$ 0.32	10.05 $\pm$ 0.25	1.50 $\pm$ 0.08	1.81 $\pm$ 0.07	0.85 $\pm$ 0.06	0.91 $\pm$ 0.06	0.88 $\pm$ 0.04
Turah	X5490	N/A	6/6	N/A	9.81 $\pm$ 0.69	N/A	1.63 $\pm$ 0.06	N/A	0.98 $\pm$ 0.09	0.98 $\pm$ 0.09
HK	X4112	11/18	N/A	7.43 $\pm$ 0.48	N/A	1.65 $\pm$ 0.10	N/A	0.66 $\pm$ 0.06	N/A	0.66 $\pm$ 0.06

Far more is known about the provenance of the Hierakonpolis sherd than the vessels recovered from Turah. Owing to the nature of the *serekh* inscription, which possibly exhibits the name of Narmer, arguably Egypt's first Pharaoh, a rather detailed discussion of its find-spot was included in its publication (Garstang, 1907: 135, Pl. III; cf. Adams, 1995: 123–124). Unfortunately, no original depositional material was attached to this sherd either.

3. Methodology

All OSL samples were collected using the minimum extract technique (MET) sampling protocol, specifically designed for use on museum materials (Hood & Schwenninger, 2015). Sample preparation was done in subdued lighting conditions following standard coarse grain and fine grain sample preparation (Hood & Schwenninger, 2015; Hood, 2017). OSL measurements were carried out on a Risø automated DA-15 luminescence reader. The SAR protocol (Murray & Wintle, 2000) was used in combination with a post-IR blue measurement so that any IRSL signal present owing to feldspar contaminants would be removed by IR stimulation carried out before measuring the OSL signal during each SAR cycle (Banerjee et al., 2001; Mauz & Lang, 2004). An IRSL/OSL depletion ratio of $\leq$ 15% was used as a rejection criterion.

Optical excitation was achieved by the use of filtered blue diodes (410–510 nm emission), and infrared stimulation using IR diodes. Luminescence signals were detected in the UV spectrum by an EMI 9635Q bialkali PMT, fitted with a 7.5 mm Hoya U340 glass filter (Riso, 2007). Sample irradiation was done using a sealed ^{90}Sr beta source at a rate of approximately 2.3Gy/min, and calibration was carried out with Risø calibration quartz (Hansen et al., 2015). Equivalent dose (D_e) determination was done using the *Analyst* software package, V4.12 (Duller, 1999), and rejection criteria determined for use with MET sampling were used (see Table 1 caption; Hood 2017). Internal dose rate ($\dot{D}_{int}$) measurements were obtained by ICP-MS analysis.

4. Results

Table 1 presents the final D_e measurement results and the internal dose rate for each vessel obtained using ICP-MS.

Of the 10 vessels examined, all three wine jars produced acceptable OSL signals, but three of the seven wavy-handled vessels did not (X5483, X5485, X5487), which is a relatively high degree of failure. Of these three vessels, two are made of marl clay and one from Nile silt, both materials for which successful OSL measurements were performed here and in other studies. It is unfortunate that X5483, X5485 and X5487 did not yield results, as all three were particularly diagnostic.

5. Discussion

Figure 3 presents the relative ages of the seven vessels for which OSL results were obtained. There are two extreme values, X5482 and X4112, whose relative ages of 1.15 and 0.7 would imply that they are roughly 700 years older and 1500 years younger than the rest of the group respectively, which is not consistent with known historical sequences (further discussion below).

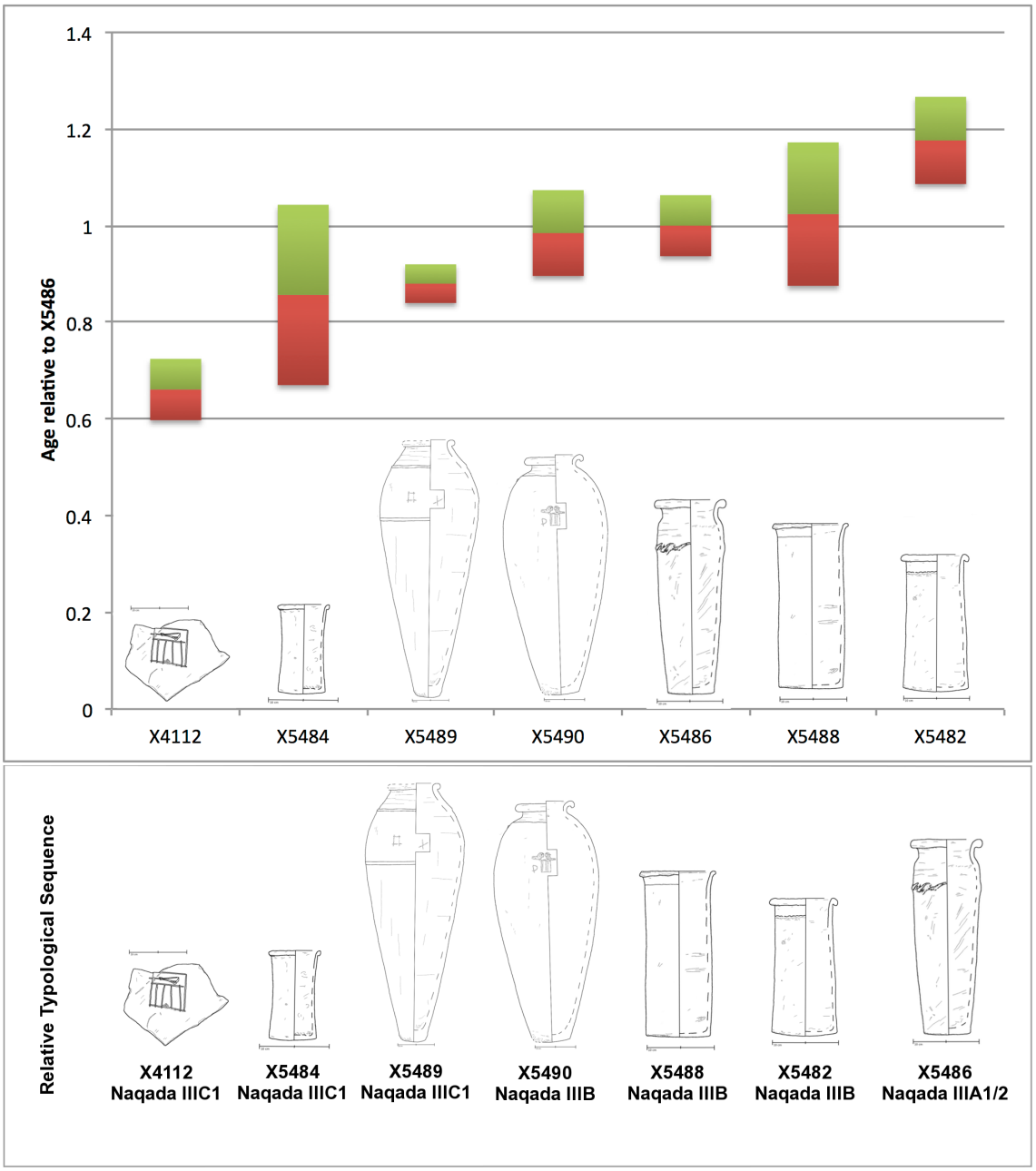

Figure 3. Upper: this graph shows the relative sequence of each vessel that produced a D_e measurement in the Turah/Hierakonpolis assemblage, based upon X5486 which acts as an anchoring reference point for the sequence (see text). The relative numerical age and error are to be found in the final column of Table 1. In turn, this graph therefore indicates the chronological progression of each vessel relative to X5486, with X4112 being the youngest in the assemblage. The red and green bars denote the upper and lower errors with the boundary between them being the central age value. Lower: in contrast with the upper figure, this figure depicts the relative typological sequence for this material based upon archaeological evidence, and thus visually demonstrates the issues encountered with some of the OSL D_e measurements.

The errors associated with the remaining five vessels are broad compared to the difference in relative ages between them. This means that any concrete statement about whether one vessel is older or younger than another must be treated with caution. However, Figure 3 also clearly demonstrates a strong relationship between the relative OSL sequence and the typological ceramic sequence. While it is beyond the scope of this paper to enter a discussion of the full archaeological implications and analysis of the OSL results (interested readers are referred to Hood, 2017), it is appropriate to say that the relative OSL age sequence of vessels is in excellent keeping with established ceramic typology of the Naqada Culture. Indeed, with the exception of X5486, all vessels are in sequence in accordance with latest typological research (Hendrickx, 1996, 2006; Köhler, 2004; Köhler & Smythe, 2004; Van Den Brink, 1996, 2001).

Although X5486 dates to the Naqada IIIA1/IIIA2 period, it is placed in the OSL relative sequence as being younger

than X5488 and X5482, which is not in keeping with the relative archaeological sequence, which places X5488 and X5482 within the later Naqada IIIB period. Within the OSL relative sequence it is almost impossible to distinguish between X5486 and X5488, due to the significant errors associated with X5488. Indeed, this is the situation between all three vessels (X5482, X5486 and X5488): their associated errors make it difficult to distinguish a true chronological sequence here, except for confidently being able to state that all three vessels are chronologically older than X5484. This is a resolution error and could be further refined should a larger data set be available. In the case of X5482, the discrepancy in relative age between it and X5486/X5488 is approximately 15% (see Figure 3), which in terms of numerical age gives an error of $\sim$750 years. This is very unlikely and could be the result of a measurement error: a single aliquot within the OSL data produced a D_e measurement which was significantly higher than the other measurements and is an outlier. However, as this aliquot could not be discounted based upon the standard rejection criteria applied, it was considered best practice to include this measurement even though it is likely to produce an overestimation in the OSL measurement.

We must also discuss sherd X4112. With regard to its relative OSL sequence, it should be noted that although fitting in with the relative sequence of the other two wine jars, the difference between the relative ages of X4112 and X5489/X5490 sits at approximately 20% (see Figure 3). This is far too large a discrepancy to fit with the relative typological sequence as it would place X4112 roughly 1 000 years later, in absolute terms, than the rest of the assemblage.

6. Conclusion

This paper has demonstrated that the application of OSL dating as a relative numerical dating method has benefits for examining the relative typological sequence of ceramics. With the small data set and large uncertainty in the dates presented, it is currently only possible to demonstrate this technique as a proof-of-principle and to make broad statements when comparing the OSL vs. archaeological relative chronologies. However this in no way invalidates the usefulness of OSL dating as a relative numerical dating tool, but rather means that more data (i.e. more vessels) are required than in this pilot study. If several examples of each vessel type were sampled, in combination with good statistical modelling and, even better, a technique such as cladistics (i.e., Hood & Valentine, 2012), OSL as a relative dating technique would be a powerful tool. Even with the limited data available, we can make the following positive observations: that the five non-outlier ages are well clustered and could be considered consistent given errors with a spread in relative numerical ages of around 5% (that is, roughly 250 years), and are consistent with the known historical chronology.

Although the wavy-handled/cylindrical vessels have proved somewhat problematic owing to issues surrounding a small data set, the wine jar assemblage demonstrates that the relative sequence of ceramics achieved through OSL dating of this assemblage has been in full agreement with the pre-existing ceramic sequence described for the Naqada Period.

In the future, this technique could be used on suitable archaeological materials world-wide. It may be of particular value when working with museum contexts, where limited archaeological information is available, or where the internal chronology of an assemblage is little understood. This technique could also be used to identify forgeries in museum collections.

While in itself this paper has not yielded new information (the relative sequences of the wavy-handled vessels and wine jars are well documented and well understood in Egyptian archaeology), this paper has demonstrated that OSL dating can be of benefit to relative chronology as well as absolute, providing a framework for implementing OSL dating as a relative numerical dating method. While the usefulness of this technique will be heavily dependent upon individual assemblages and the quality of available relative dating methods, further potential for this technique is significant in the museum world and further advances in ceramic chronology could be made as a result.

Acknowledgments

This research was completed owing to the generous support of the G.A. Wainwright Fund; the Clarendon Fund; Merton College, Oxford; and Brasenose College, Oxford. ICP-MS analysis was carried out at the Department of Earth Sciences at the University of Oxford. We would like to thank the University of Vienna for allowing access to the Turah teaching collection, which provided the majority of vessels used in this research. We also wish to thank the Garstang Museum, Liverpool (especially Steven Snape) for allowing access to the sherd from Hierakonpolis (X4112; museum identification number: E.5248).

References

Adams, B. *Ancient Nekhen: Garstang in the City of Hierakonpolis*. SIA Publishing, New Malden, 1995.

Banerjee, D., Murray, A., Bøtter-Jensen, L., and Lang, A. *Equivalent Dose Estimation Using a Single Aliquot of Polymineral Fine Grains*. Radiation Measurements, 33(1): 73–94, 2001.

Duller, G. *Luminescence Analyst Computer Programme*. Aberystwyth, v4.12 edition, 1999.

Durcan, J., King, G., and Duller, G. *DRAC: Dose Rate and Age Calculator for trapped charge dating*. Quaternary Geochronology, 28: 54–61, 2015.

Garstang, J. *Excavations at Hierakonpolis, at Esna and in Nubia*. Annales du Service des Antiquitiés de l'Égypte, 8: 132–148, 1907.

Hansen, V., Murray, A., Buylaert, J.-P., Yeo, E.-Y., and Thomsen, K. *A New Irradiated Quartz for Beta Source Calibration*. Radiation Measurements, 81: 123–127, 2015.

Hendrickx, S. *The Relative Chronology of the Naqada Culture. Problems and Possibilities*. In Spencer, J. (ed.), *Aspects of Early Egypt*, pp. 36–69. British Museum Press, London, 1996.

Hendrickx, S. *Predynastic–Early Dynastic Chronology*. In Hornung, E., Krauss, R., and Warburton, D. (eds.), *Ancient Egyptian Chronology*, pp. 55–93. Brill, Leiden, 2006.

Highcock, E., Hood, A., and Schwenninger, J.-L. *Luminescence as a Relative Dating Tool: Part A – Theory*. Ancient TL, 37(2): 9–13, 2019.

Hood, A. *New Insights into Old Problems: The Application of a Multidisciplinary Approach to the Study of Early Egyptian Ceramic Chronology, with a Focus on Luminescence Dating*. PhD thesis, University of Oxford, 2017.

Hood, A. and Schwenninger, J.-L. *The Minimum Extraction Technique: A New Sampling Methodology for Optically Stimulated Luminescence Dating of Museum Ceramics*. Quaternary Geochronology, 30: 381–385, 2015.

Hood, A. and Valentine, J. *The Application of Cladistics to Early Dynastic Egyptian Ceramics: Applying a New Method*. In Knoblauch, C. and Gill, J. (eds.), *Egyptology in Australia and New Zealand 2009: Proceedings of the Conference Held in Melbourne, September 4th-6th*, pp. 47–59, Oxford, 2012. Archaeopress.

Kaiser, W. *Zur Inneren Chronologie der Naqadakultur*. Archaeologia Geographica, 6: 69–77, 1957.

Köhler, E. *On the Origins of Memphis: The New Excavations in the Early Dynastic Necropolis at Helwan*. In Hendrickx, S., Friedman, R., Ciałwicz, K., and Chłodnicki, M. (eds.), *Egypt at its Origins: Studies in Memory of Barbara Adams. Proceedings of the International Conference "Origin of the State. Predynastic and Early Dynastic Egypt", Kraków, 28th August–1st September 2002*, volume 138 of *Orientalia Lovaniensia Analecta*, pp. 295–315, Leuven, 2004. Peeters.

Köhler, E. *Early Dynastic Egyptian Chronologies*. In Shortland, A. and Bronk Ramsey, C. (eds.), *Radiocarbon and the Chronologies of Ancient Egypt*, pp. 224–234. Oxbow Books, Oxford, 2013.

Köhler, E. and Smythe, J. *Early Dynastic Pottery from Helwan – Establishing a Ceramic Corpus of the Naqada III Period*. Cahiers de la Céramique Égyptienne, 7: 123–144, 2004.

Köhler, E. and Thalmann, J.-P. *Synchronising Early Egyptian Chronologies and the Northern Levant*. In Höflmayer, F. and Eichmann, R. (eds.), *Egypt and the Southern Levant in the Early Bronze Age*, volume 31 of *Orient-Archäologie*, pp. 181–206. Rahden/Westf., Leidorf, 2014.

Mauz, B. and Lang, A. *Removal of the Feldspar-derived Luminescence Component from Polymineral Fine Silt Samples for Optical Dating Applications: Evaluation of Chemical Treatment Protocols and Quality Control Procedures*. Ancient TL, 22(1): 1–8, 2004.

Murray, A. and Wintle, A. *Luminescence Dating of Quartz Using an Improved Single-Aliquot Regenerative-Dose Protocol*. Radiation Measurements, 32(1): 57–73, 2000.

Petrie, W. *Sequences in Prehistoric Remains*. Journal of the Royal Anthropological Institute of Great Britain and Ireland, 29: 295–301, 1899.

Petrie, W. *Diospolis Parva*. Egypt Exploration Fund, London, 1901.

Riso, T. *Guide to "The Riso Single grain laser OSL system"*. Technical report, Riso National Laboratory, 2007.

Van Den Brink, E. *The Incised Serekh-Signs of Dynasties 0-1, Part I: Complete Vessels*. In Spencer, J. (ed.), *Aspects of Early Egypt*, pp. 140–58. British Museum Press, London, 1996.

Van Den Brink, E. *The Pottery-Incised Serekh-Signs of Dynasties 0-1 Part 11: Fragments and Additional Complete Vessels*. Archéo-Nil, 11: 23–100, 2001.

Reviewer

Daniel Richter

Ancient TL

LDAC: An Excel-based program for luminescence equivalent dose and burial age calculations

Peng Liang[1,2,3*] and Steven L. Forman[2]

[1] Department of Geography, School of Earth Sciences, Zhejiang University, Hangzhou 310027, China
[2] Geoluminescence Dating Research Lab., Department of Geosciences, Baylor University, Waco, TX 76798, USA
[3] Institute of Geology and Geophysics, Chinese Academy of Sciences, Beijing 100029, China

*Corresponding Author: LiangPeng@mail.iggcas.ac.cn or LiangPeng2012@live.cn

Received: August 14, 2019; in final form: January 14, 2020

Abstract

In the past 20 years optically stimulated luminescence (OSL) dating has advanced as a well-established geochronometer for dating Quaternary sediments. Currently, there are powerful calculation platforms for specific calculations, such as the R package 'Luminescence' and the web-based dose rate calculator DRAC. However, the community lacks a self-contained computational synthesis that can process equivalent dose and dose-rate calculations to avoid unnecessary data exchange among multiple-platforms that may inadvertently propagate errors. Thus, we have developed a unified calculation program that maintains, archives and synthesizes basic OSL data, applies appropriate statistical models, and dose rate parameters in an updatable platform, to render statistically significant OSL ages. In this paper, the Luminescence Dose and Age Calculator (LDAC) written in Microsoft Visual Basic for Application is presented that can compute final equivalent dose values, the environmental dose rate, and render a final burial OSL age. LDAC incorporates statistical parameters, visual presentations of the equivalent dose distribution, applies well-developed statistical age models, and uses up-to-date dose rate parameters into a computational system using fifteen linked functional routines. Most notably, a Markov chain Monte Carlo slice sampling method was employed to estimate the parameters of the minimum and maximum age models. Also, the statistical basis for error propagation of dose rate and final age was improved. The program is designed to be user-friendly with operations and data entry conveniently executed through a graphical user interface. The operations and calculations are presented with transparency and flexibility, allowing for modification of given values, constants, and algorithms. This computational platform is easily loaded on to a PC and can be used in a Windows environment equipped with Microsoft Excel 2010 or later. The latest version of LDAC can be downloaded along with a user manual at https://github.com/Peng-Liang/LDAC.

Keywords: OSL dating; equivalent dose; statistical age models; dose rate; LDAC; Microsoft VBA

1. Introduction

An accurate and precise chronology for sedimentary processes and the enclosure of associated fossils or artifacts is a cornerstone of the geosciences. Optically Stimulated Luminescence (OSL) dating since 1985 has evolved significantly as an accurate dating technique, providing improved chronologic control for the past 200 ka (Huntley et al., 1985; Wintle, 2008; Wintle & Adamiec, 2017). This geochronometer, based on the principles of radiation dosimetry, measures the burial time since mineral grains, such as quartz and K-feldspar, were last exposed to sunlight (Aitken 1998, p. 6–36; Murray & Wintle 2000; Murray & Wintle 2003; Wintle & Murray 2006; Preusser et al. 2009). An important value in OSL dating is the equivalent dose (D_e), which is the estimate of the ionizing radiation dose received during the burial

period (in Grays; Gy) after solar resetting (Aitken 1998, p. 6–36). An OSL age is calculated by division of the D_e by the estimated dose rate (D_r), which is an evaluation of the exposure rate to ionizing radiation (mGy/yr) from the surrounding sediments and cosmic/galactic sources (Aitken 1998, p. 6–11). OSL dating has advanced significantly in the past thirty years with the advent of single aliquot and grain regeneration (SAR) methods (e.g., Wintle & Murray 2006; Wintle & Adamiec 2017). This geochronometer is most robust when dating sediments that have been well and uniformly solar reset, such as mineral grains from aeolian and littoral environments (e.g., Lang et al. 2003; Forman et al. 2014; Yang et al. 2015; Yang et al. 2019; Lancaster et al. 2016; Tamura et al. 2019). The D_e distribution for well solar reset grains often shows a unimodal distribution, with a low overdispersion value (<0.20) (Forman et al., 2014). However, the D_e can vary substantially for separate aliquots or grains from fluvial and lacustrine environments, reflecting partial solar resetting or incorporation of older grains, mostly exposed in turbid water environments (e.g., Aitken 1998, p. 143–175; Arnold et al. 2007; Cunningham & Wallinga 2012; Hesse et al. 2018). Thus, the D_e distribution of variably solar reset grains often exhibits a multi-modal distribution with a high overdispersion (>0.30). Commonly, the youngest D_e population for grains is the closest to the actual age for partially solar-reset sediments (e.g., Cunningham & Wallinga 2012; Hesse et al. 2018).

Fortunately, there are several statistical models such as the central, minimum, maximum, and finite mixture age models that have been developed to deconvolute D_e populations that reflect the time since sediment deposition and shielding from further sunlight exposure (Galbraith & Green, 1990; Galbraith et al., 1999; Galbraith & Roberts, 2012). In turn, the environmental D_r is a required assessment for dating, which is defined by ten separate variables reflecting complex, ionizing-radiation conditions during the burial period (Aitken 1998, p. 37–57; Durcan et al. 2015). Thus, there is a need for a calculation platform that synthesizes D_e data, incorporates appropriate statistical models, and D_r parameters in a self-consistent manner, which can be easily updated with future refinements in constants, statistical analyses, and data visualization. Several well-appointed calculation programs have been developed for specific D_e and D_r computations that serve the luminescence dating community well (e.g., Grün 2009; Kreutzer et al. 2012; Peng et al. 2013; Durcan et al. 2015; Burow et al. 2016). For example, a highly flexible **R** script-based computational package, `'Luminescence'` (Kreutzer et al., 2012, 2018), was designed to further analyze the luminescence data from SAR measurements. This package was integrated into the latest version of the Analyst luminescence software (v4.57), which supports modeling functions and graphing routines (Duller, 2018). However, the **R**`'Luminescence'` package lacks a visual interface with user interactions through the **R** programming environment. As a partial remedy for this platform a graphical user interface (GUI) does exist through `''RLumShiny''` (Burow et al., 2016), but the graphic-presentation functionality is limited. Desktop- or web-based programs, such as the AGE (Grün, 2009) and DRAC (Durcan et al., 2015), have been developed to address the challenges of dose rate calculations. Nevertheless, one must exchange data among multiple programs to obtain the final age, which increases the risk of involuntary errors and inconsistent error analyses. To our knowledge, the luminescence dating community lacks an integrated and interfaced calculation platform to determine OSL ages such as software Calib (Stuiver et al., 2019) or OxCal (Ramsey, 1995, 2017) for radiocarbon dating, ISOPLOT (Ludwig, 1988) or IsoplotR (Vermeesch, 2018) for U-Pb dating, and CRONUS (Balco et al., 2008) or iceTEA (Jones et al., 2019) for cosmogenic nuclide dating.

We present an integrated OSL age calculation program with a well-defined statistical foundation, based on the Microsoft Visual Basic for Application (VBA), referred to as 'Luminescence Dose and Age Calculator (LDAC)', to fulfill a computational need for OSL geochronology. The program is a user-friendly OSL-age-computational system based on previously presented statistical analyses, mathematical relations and other formulations (Galbraith, 1988, 1990, 2003; Bailey & Arnold, 2006; Arnold et al., 2009; Grün, 2009; Duller, 2007, 2015; Durcan et al., 2015). The Microsoft Excel platform was chosen to provide the broadest access and accountability for code, constants, and calculations, though certain Monte Carlo based calculations have lag times of ~ 1 minute. LDAC offers a computational platform to determine OSL age estimates with metrics to assess the statistical robustness of equivalent dose data (Bailey & Arnold, 2006; Arnold & Roberts, 2009), the applicability of statistical age models (Galbraith & Roberts, 2012) and with up-to-date dose rate parameters (Adamiec & Aitken, 1998; Guérin et al., 2011; Liritzis et al., 2013; Durcan et al., 2015). Included in this platform are revised computational pathways for determining overdispersion values on small D_e populations (Galbraith & Roberts, 2012), a new slice sampling method to deconvolute subpopulations using the minimum and maximum models (Neal, 2003), and Monte Carlo based-calculations for the final OSL age estimate. This program can be easily updated to improve dose rate determinations, OSL age calculations, enhanced visualizations, and as a platform to encourage inter-laboratory OSL age comparisons. The current version (LDAC v1.0) of this computational scheme with the code is open access to the community at `https://github.com/Peng-Liang/LDAC`, where a video highlights the capabilities of this computation package. We welcome use by the community and comments to improve this nascent computational platform.

2. Architecture of LDAC

LDAC is an Excel VBA-based package to facilitate the assemblage of luminescence age information and associated calculations. This software is applicable for individual equivalent dose measurements using the SAR protocol (e.g., Wintle & Murray 2006). This computational system has two major components for D_e and D_r calculation (Fig. 1),

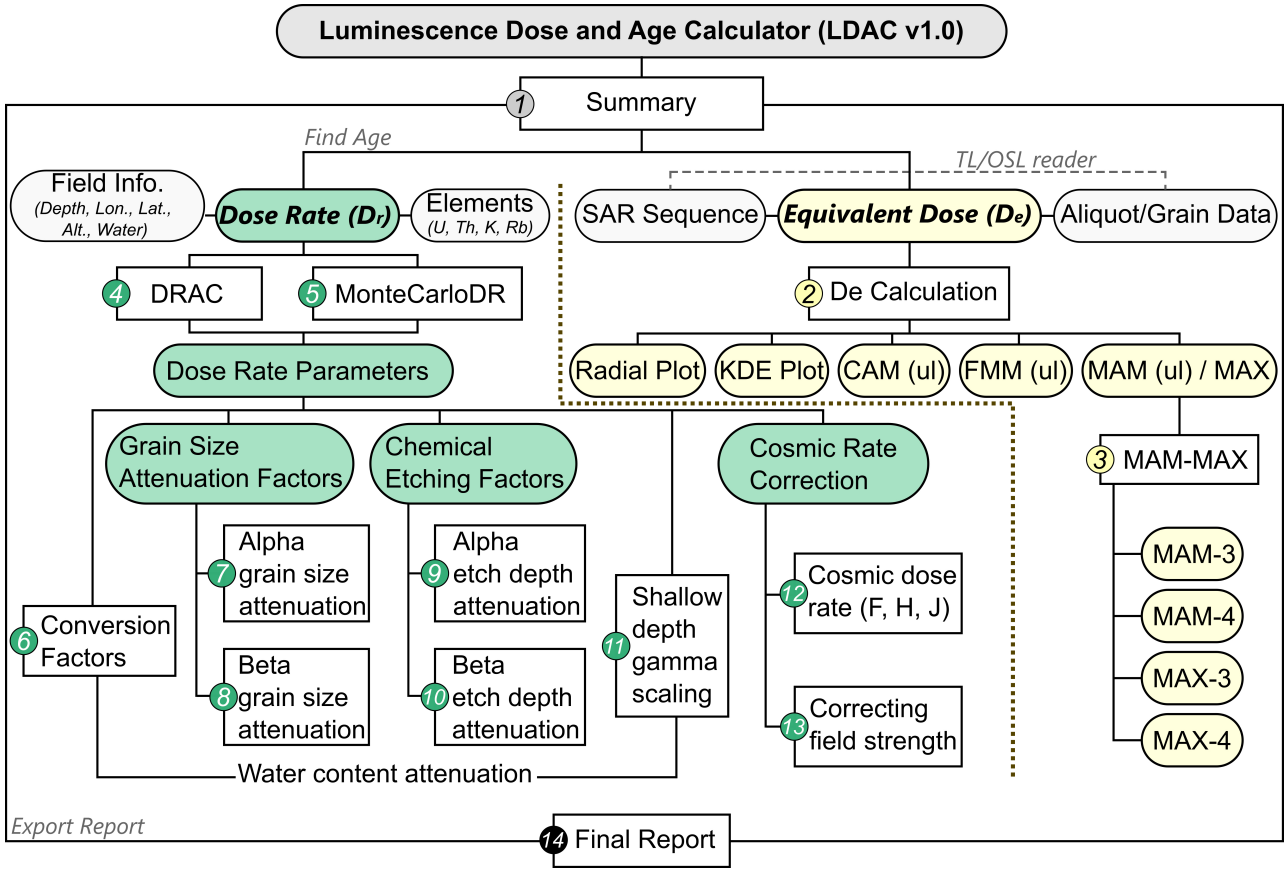

Figure 1. Computational pathways for the Luminescence Dose and Age Calculator (LDAC). The rectangular boxes marked with numbers represent worksheets in LDAC, while the oval frames represent attribute information. The software has two components which are the dose rate calculation system (green) and equivalent dose calculation system (yellow).

based on the following simplified luminescence age equation (Aitken 1998, p. 6–11):

$$Age(yr) = \frac{D_e\,(\mathrm{Gy})}{D_r\left(\frac{\mathrm{Gy}}{\mathrm{yr}}\right)}, \qquad (1)$$

where the D_e is the burial dose accumulated in grains; the D_r is the dose rate that comes from exposure to ionizing radiation from α, β and γ particles in the grain, surrounding sediments, and from cosmic rays (Aitken 1998, p. 37–49). This suite of computations is based on fourteen-linked calculation routines for applying statistical models to determine D_e values and render a corresponding luminescence age (Fig. 1).

The first step to use this computational package is the entry of individual grain or aliquot D_e data, elemental, environmental and contextual information to calculate sample $D_r$which is organized in the "Summary" worksheet (Fig. 1; Supplement A). Subsequent calculations of a final D_e, D_r and an OSL age are presented in succeeding workspaces with these calculations based on data entry on to the "Summary" page (Fig. 1; Supplement A). This "Summary" page allows users to input pertinent information for a sample, such as lab number, field number, sediment type, sample locality and analyst. In turn, there is computation space for D_r information, such as the U, Th, K or K_2O, Rb, water content (mass of water/mass of dry sediment), organic content, grain size, geographical coordinates, elevation, depth, overburden density and a sub-routine to calculate a cosmic dose contribution. Lastly, there are data entry spaces for parameters about the laboratory protocols, including preheat, cut heat, and annealing temperatures, test dose, and irradiation dose cycles (Fig. 1; Supplement A), which are used for keeping a record.

The "Summary" page also has flexible space for the entry of first tier of luminescence data directly imported from the 'Analyst' platform (Duller, 2007, 2018). This data includes calculated individual D_e values for each aliquot or grain (for up to 5000 D_e values) and related parameters such as recycling ratio, percent recuperation (Murray & Wintle, 2000; Wintle & Murray, 2006) with associated errors. Other pertinent diagnostic metrics such as the fast ratio (Durcan & Duller, 2011) and the infrared depletion ratio (Duller, 2003) can also be input. Individual D_e values for single aliquots or grains that fail to meet the data quality assessment metrics (cf. Murray & Wintle 2000; Duller 2003; Durcan & Duller 2011) are marked in a reddish-pink with a toggle choice ('Reject') and are removed from subsequent calculations but stored as part of total aliquots. Designating the 'Transfer'

button transmits the accepted D_e values with standard errors for aliquots/grains into the "De Calculation" page to visualize the D_e data and apply statistical age models.

The "De Calculation" page includes statistical parameters, graphical presentation (see section 3), and parametric statistical models (see section 4) such as common, central, minimum, maximum, and finite mixture age models (Galbraith & Green 1990; Galbraith et al. 1999; Galbraith & Roberts 2012; Fig. 1). Normal and log-normal distributions can be applied to all age models, except the maximum age models, which were only designed for log-transformed data (Olley et al., 2006; Galbraith & Roberts, 2012). LDAC offers two flexible approaches to estimate the uncertainty of overdispersion for the central age model. The first and default option utilizes the formula provided by Galbraith et al. (1999), but this equation is often inappropriate for smaller sample sizes (e.g., <30 aliquots) (Galbraith & Roberts, 2012). An alternative calculation is applied by computing the 95% compatibility interval (CI) of the profile log-likelihood function (Galbraith & Roberts, 2012), when the 'Plot-Lik' checkbox is chosen (see section 4.1). Application of minimum or maximum age models are a separate calculation on a succeeding worksheet entitled "MAM-MAX" (Worksheet 3, Fig. 1). Moreover, two types of diagrams, radial plot (Galbraith, 1988) and kernel density estimate plot (Galbraith & Roberts, 2012), can be created in the "De Calculation" page for data visualization (Fig. 2). The appearance of these graphical displays can be adjusted by users with inputs for decimal places, dot size, dot and curve color, below the plot area in the worksheet "De Calculation", and the dose unit can be chosen either seconds or Grays (worksheet 2 in Fig. 1; Supplement A). Exported figures include sample information such as lab number, the number of aliquots/grains, overdispersion, age model used and final D_e and errors (Fig. 2). Finally, the chosen D_e (tick box) and the designated calculation models will be automatically transferred to the "Summary" page to determine the final OSL age.

Calculation of the cosmic and total environment dose rate, final OSL age, and associated uncertainties (1σ) is actuated by clicking the 'Find Age' button in the "Summary" page (see section 5). The default option for calculating dose rate is modified from the DRAC (v1.2), and the associated uncertainties are propagated in quadrature (Durcan et al., 2015). Propagation of uncertainties through Monte Carlo simulations is also available for the final age calculation in LDAC (see section 5.4). Highlighted dose and age calculation results of the target sample can be compiled as a *.pdf version report via the 'Export Report' button (Fig. 1). This report includes sample identification, dose rate, equivalent dose, sequence information, error analyses, and an associated data-based summary table. Additionally, the relevant graphical presentations will be included in this report if available (worksheet 14 in Fig. 1; Supplement B).

There are additional functionalities in the right-hand corner actuated by the 'Show info', the 'Calibration' and the 'Import' tabs. The 'Show info' allows users to display the underlying basis of the dose-rate calculation and relevant parameters (worksheets 4 to 14, Fig. 1). The 'Calibration' button is used to update the strength of radiation source of the OSL readers in the user's laboratory to compensate for decay changes in source strength. The 'Import' button can transfer data between different versions of LDAC. To familiarize the user with this platform, an example data set is provided after clicking the 'Load Example' button on the "Summary" page.

3. Statistical parameters and graphical presentation of observed D_e values

3.1. Statistical parameters

Statistical parameters may be useful to characterize the D_e distributions for a sample based De values from individual aliquots or grains and may assist in deciphering the depositional environment (Bailey & Arnold, 2006; Arnold & Roberts, 2009). LDAC provides two widely used descriptive statistical parameters, including weighted skewness (Bailey & Arnold, 2006; Arnold & Roberts, 2009) and the chi-square (χ^2) homogeneity test (Galbraith, 2003; Galbraith & Roberts, 2012), to score the original observed data distribution and help to decide which age model is statistically appropriate.

The weighted skewness (c) is calculated as (Bailey & Arnold, 2006):

$$c = \sum_{i=1}^{n} \left\{ w_{\mathrm{ci}} \left(\frac{d_i - \delta}{S_{D_e}} \right)^3 \right\} \frac{1}{\sum_{i=1}^{n} w_{\mathrm{ci}}} \qquad (2)$$

where $w_{\mathrm{ci}} = \left| \frac{1}{\sigma_i / d_i} \right|$, d_i and σ_i are the observed D_e and corresponding standard error for an aliquot or a grain i, respectively; n and s_{D_e} are the total number and standard deviation of all valid observed D_e values. The δ here is the weighted mean of observed D_e values (Arnold & Roberts, 2009) or the central dose value obtained from 'un-logged' central age model (see section 4.1). Note that Eq. 2 is only suitable for original numeric values. When log-transformation is used in data analyses (tick 'Log-Normal'), the following equation is applied (Arnold & Roberts, 2009):

$$c = \sum_{i=1}^{n} \left\{ w_{\mathrm{ci}} \left(\frac{ln(d_i) - \delta}{S_{\ln \mathrm{De}}} \right)^3 \right\} \frac{1}{\sum_{i=1}^{n} w_{\mathrm{ci}}} \qquad (3)$$

where $s_{\ln \mathrm{De}}$ is the standard deviation of the natural logarithm D_e values, δ is the central value obtained from the usual (log-transformed) common or central age model (see section 4.1).

LDAC employs the standard error of skewness σ_c, an approach proposed by Bailey & Arnold (2006), to test the relative statistical significance of the skewness scores calculated by Eq. 2 or Eq. 3. The σ_c is approximated as (Tabachnick & Fidell, 1996):

$$\sigma_c = \sqrt{6/n}. \qquad (4)$$

The modeling investigations of single grains D_e indicate that $\pm\, 2\sigma_c$ can be regarded as the limits for statistically significance of the weighted skewness c (Bailey & Arnold, 2006).

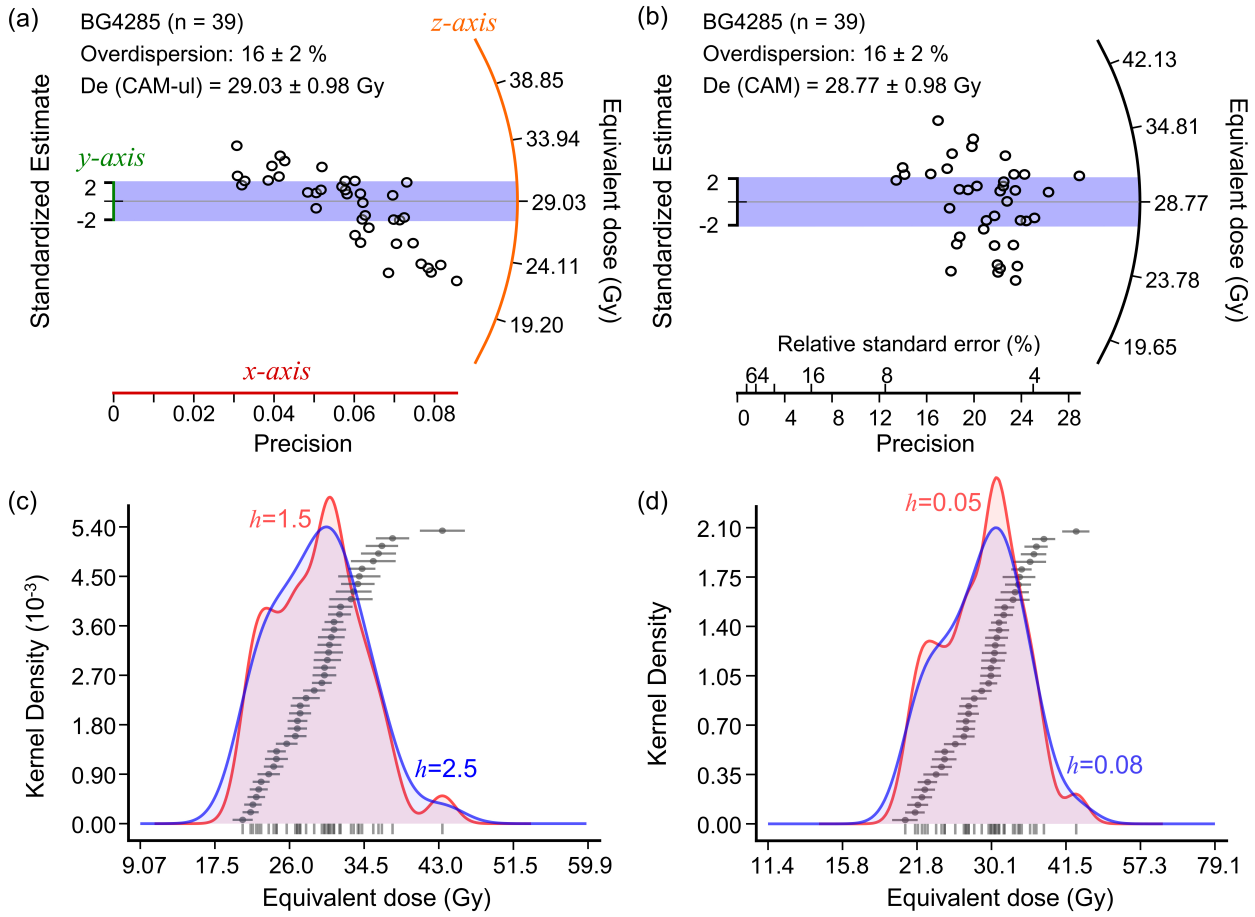

Figure 2. Example figures on "De Calculation" worksheet of radial plots (a, b) and graphs of kernel density estimate (KDE) (c, d) for sample BG4285. Figures (a) and (c) show BG4285 data with normal scale and figures (b) and (d) display the same data with log-transformed scale. The orange and blue colors in (c) and (d) mark the KDE curve with different bandwidth "*h*", revealing potentially different equivalent dose peaks. The grey dots and bars show the empirical cumulative distribution for equivalent dose values and ± 1 standard error.

However, a critical c value of $\pm 1\sigma_c$ is a more meaningful indicator of statistical significance for multi-grain data because of the 'averaging out' effects (Arnold et al., 2007; Arnold & Roberts, 2009). Although LDAC uses $\pm 1\sigma_c$ as a critical skewness value to categorize D_e or log D_e distributions as 'positive' ($c > \sigma_c$), 'negative' ($c < -\sigma_c$) or 'not significant' ($-\sigma_c \leq c \leq \sigma_c$), the original c and σ_c values are also provided in the "De Calculation" page (Supplement A).

LDAC utilizes the 'p-value' of the χ^2 distribution to provide a visual assessment of homogeneity of independent D_e estimates (Galbraith, 2003). This homogeneity test supposes that there are n independent observed values $d_i \pm \sigma_i$, and each d_i is drawn from a normal distribution $N(\mu_i,\ \sigma_i)$. The null hypothesis is that all individual values of μ_i are equal to an unknown common value μ. In this case, the maximum likelihood estimates of $\widehat{\mu}$ under the null hypothesis is:

$$\widehat{\mu} = \frac{\sum_{i=1}^{n} w_i d_i}{\sum_{i=1}^{n} w_i}, \tag{5}$$

where $w_i = \frac{1}{\sigma_i^2}$, and the homogeneity test statistic (G) is defined by:

$$G = \sum_{i=1}^{n} w_i (d_i - \widehat{\mu})^2. \tag{6}$$

Then, a p-value, the probability that a random value drawn from a χ^2 distribution with $n-1$ degrees of freedom is $>G$ (Galbraith, 2003; Galbraith & Roberts, 2012), is calculated according to the G statistic and the degrees of freedom. The smaller the p-value for any given number of observed values, the stronger the evidence to reject the null hypothesis (Galbraith & Roberts, 2012). However, if the p-value is greater than the conventional critical value 0.05 (a small G statistic), then there is insufficient evidence for overdispersion, rather than no overdispersion between observed values (Galbraith, 2003; Galbraith & Roberts, 2012). This homogeneity test can also be applied to evaluate the agreement of paired-age or -dose estimates (Galbraith & Roberts, 2012).

3.2. Graphical presentation

Objective statistical analyses and visual assessments for D_e distributions are critical to evaluate the most appropriate

age model (Galbraith, 1988, 2005, 2010). A useful statistical representation of D_e values is with a radial plot, that displays D_e values against precision (Galbraith, 1988, 2005) and is used widely by the trapped-charge dating community (e.g., Bøtter-Jensen et al. 2003, p. 296–310; Arnold & Roberts 2009; Galbraith & Roberts 2012; Forman 2015; Yang et al. 2015; Guérin et al. 2017). Another useful graphical presentation is the kernel density estimate plot (Sircombe, 2004; Galbraith, 2010; Galbraith & Roberts, 2012; Vermeesch, 2012, 2018; Ramsey, 2017), which is a graphic representation of continuous values that approximates the distribution as a probability density function (Galbraith, 2010).

The radial plot reflects the data distribution, with each value registered independently, where the y-axis is a standardized estimate and the x-axis represents the precision of values (Galbraith, 1988). This plot supposes that there are observed values $d_i \pm \sigma_i$ for aliquot or grain $i = 1, 2, \ldots, n$. The coordinate for each point (x_i, y_i) is calculated by:

$$x_i = \frac{1}{\sigma_i} \text{ and } y_i = \frac{(d_i - d_0)}{\sigma_i}, \tag{7}$$

where d_0 is a convenient reference value (Galbraith & Roberts, 2012). In LDAC, d_0 is the value calculated based on un-logged D_e values by the central age model (CAM-ul) (see section 4.1) and the y scale is truncated at ± 2 standardized estimation (Fig. 2a), which can be used as an aid to evaluate the agreement between any individual value and a reference value (Galbraith & Roberts, 2012). The horizontal line $y = 0$ corresponds to $d_i = d_0$; the ratio y_i/x_i is the slope of the line from the origin point (0, 0) to the target point (x_i, y_i) , which is the difference between an observed value d_i and reference value d_0 (Fig. 2a). The scale of the slope, the z-axis, is displayed as an arc of a circle (Galbraith, 1988, 1990) to yield the radial nature of the plot. When the data is log-transformed, for the observed values d_i with associated standard error σ_i, the Eq (7) is modified to:

$$x_i = \frac{1}{\sigma_i/d_i} \text{ and } y_i = \frac{\ln d_i - \ln d_0}{\sigma_i/d_i}, \tag{8}$$

where d_0 is the value calculated by logarithmic-based central age model (CAM) (see section 4.1). In this case, the precision in x-axis represents the reciprocal of relative standard error and z-axis is in a natural logarithm scale (Fig. 2b).

The kernel density estimate (KDE) for a set of observed values $d_1, d_2, \ldots, d_n$ at x is calculated based on the Gaussian kernel as follows:

$$\text{KDE}(x) = \frac{1}{n}\sum_{i=1}^{n}\left[\frac{1}{h\sqrt{2\pi}}\exp\left(-\frac{1}{2}\left(\frac{x-d_i}{h}\right)^2\right)\right], \tag{9}$$

where h is known as smoothing parameter 'bandwidth' that plays an important role in KDE (Silverman 1998, p. 43–59). As h varies there will be variable resolution of the density curve depicting varying peaks of the data distribution (Silverman 1998, p. 43–59; Galbraith & Roberts 2012; Vermeesch 2012; Fig. 2c, d). The default method for KDE representation is 'adaptive bandwidth' which varies with the density of the data (Botev et al. 2010; Supplement C). This method uses a narrower bandwidth near the dense data distribution and a wider bandwidth near the sparse data distribution (Botev et al., 2010; Vermeesch, 2018). Thus, the resolution of the KDE curve is optimized by the data availability (Vermeesch, 2018). A constant bandwidth for KDE derived from Silverman (1998, p. 45–49) and user-defined values (Supplement C) are also available. Moreover, a probability density function method, where the bandwidth h in Eq. 9 is replaced by the analytical uncertainties σ_i, is provided when the bandwidth method 'PDF plot' is chosen (Supplement C). A continuous KDE curve does not directly reflect the original data distribution, so the individual D_e values with errors are plotted on the KDE graph in rank order as an empirical distribution function (Fig. 2c, d; Galbraith & Roberts 2012). Additionally, the KDE can be calculated with log-transformed data, when d_i in Eq. 9 is altered to $\ln d_i$ (Fig. 2d).

4. Age models for D_e determination

The complexity of depositional processes, environmental microdosimetry, and individual mineral grains response to optical stimulation may result in D_e values measured from separate aliquots or grains exhibiting significant scatter (Jacobs & Roberts, 2007; Arnold & Roberts, 2009; Galbraith & Roberts, 2012; Cunningham & Wallinga, 2012; Guérin et al., 2017). Thus, it is usually inappropriate to analyze such D_e data by assuming a simple Gaussian distribution, by using the weighted average method (Taylor 1997, p. 173–179), known as the common age model (Supplement C; Galbraith 2005, p. 47–50; Galbraith & Roberts 2012). Fortunately, there exists other statistical models that are more appropriate metrics for non-Gaussian data distributions. This section focuses on presenting the logic and mathematical bases for the application of the much used central, minimum and maximum age models to D_e data; the statistical principles of the common and finite mixture age models are discussed in the supplementary information (Supplement C).

4.1. Central age model

The central age model (CAM) is commonly adopted to determine a final D_e value for well solar reset sediments, such as aeolian sand (e.g., Forman et al. 2014; Yang et al. 2015; Hesse et al. 2018; Tamura et al. 2019). The CAM assumes that D_e values are not consistent even if the measurement errors σ_{w_i} are considered, and the natural logarithm of true D_e ($\ln D_e$) values are drawn from a normal distribution with central dose δ and standard deviation σ (Galbraith et al., 1999; Galbraith & Roberts, 2012). The standard deviation σ, also known as overdispersion, denotes an additional dispersion after accounting for within-aliquot/grain measurement errors (Galbraith & Roberts, 2012). The central dose δ and overdispersion σ are estimated with simultaneous evaluation of the following three equations (Galbraith et al., 1999):

$$w_i = \frac{1}{\sigma^2 + {\sigma_{w_i}}^2} \tag{10}$$

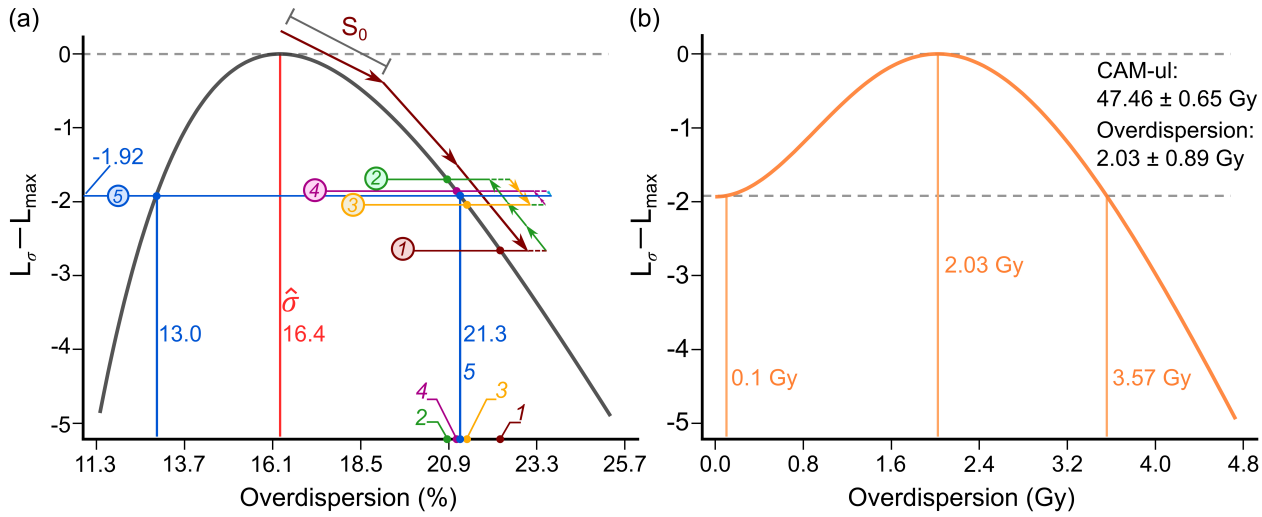

Figure 3. Examples of profile log-likelihood function for the overdispersion in the central age model. (a) Illustration of the algorithm for calculating the standard error of overdispersion based on profile log-likelihood function (BG4285). The limits of 95% comparability interval were calculated by searching the values of σ to fulfill $L_\sigma - L_{\max} = 1.92$ on this profile log-likelihood function. Sequential the calculation entails, first, give an initial step (brown arrow) to cross over the line $L_\sigma - L_{\max} = 1.92$ and find the brown point ①. Then, give a finer step (green arrow) to go back and cross over the line 1.92 again to find the green point ②. Repeat this calculation until a fine limit ⑤, under the tolerance (0.01%), was reached. The calculation of lower limit is same. (b) An example of output shows the profile log-likelihood function for overdispersion parameter σ in the un-logged central age model (CAM-ul); in this case, the overdispersion and associated error are expressed in grays (Gy).

$$\delta = \frac{\sum_{i=1}^{n} w_i d_i}{\sum_{i=1}^{n} w_i} \tag{11}$$

$$\sum_{i=1}^{n} {w_i}^2 (d_i - \delta)^2 = \sum_{i=1}^{n} w_i \tag{12}$$

where d_i and σ_{w_i} are the natural logarithm of observed D_e value and relative standard error for aliquot or grain i, respectively. When overdispersion σ is zero, the CAM is mathematically equivalent to the common age model (Galbraith & Roberts, 2012). These equations are solved by starting with an initial $\sigma = 0.5$ (overdispersion is 50%), and calculate w_i for each i based on Eq. 10, and then calculate δ based on Eq. 11; this calculation iterates and updates sequentially with an $\sigma = \sigma(\frac{\sum_{i=1}^{n} {w_i}^2 (d_i-\delta)^2}{\sum_{i=1}^{n} w_i})$. Once the parameters σ and δ satisfy Eq. 12 with $\frac{\sum_{i=1}^{n} {w_i}^2 (d_i-\delta)^2}{\sum_{i=1}^{n} w_i} = 1$ (assuming $w_i \neq 0$), appropriate estimates, $\widehat{\sigma}$ and $\widehat{\delta}$, are derived.

LDAC provides two methods to estimate the standard error of the overdispersion. For large sample populations, the standard error (se) could be approximately (Galbraith et al., 1999):

$$\text{se}\ (\delta) = \sqrt{\frac{1}{\sum_{i=1}^{n} w_i}} \tag{13}$$

$$\text{se}\,(\sigma) = \sqrt{\frac{1}{2\sigma^2 \sum_{i=1}^{n} {w_i}^2}} \tag{14}$$

The above $se(\sigma)$ can be unreliable for smaller sample populations (e.g., < 30) (Galbraith & Roberts, 2012). In this case, an alternative calculation is executed using the 'profile log-likelihood function' to provide an assessment of the standard error of the overdispersion. This method constructs a profile log-likelihood function of L_σ against σ (Galbraith & Roberts, 2012), where

$$L_\sigma = \frac{1}{2} \sum_{i=1}^{n} \left\{ \ln w_i - w_i (d_i - \delta)^2 \right\}. \tag{15}$$

When σ equals the maximum likelihood estimated overdispersion $\widehat{\sigma}$, the L_σ has its maximum value $L_{\max}$ and it decreases as σ departs from $\widehat{\sigma}$. Based on the large-sample maximum likelihood theory and the likelihood-ratio test, approximate boundaries of 95% CI are values of σ for which L_σ is within 1.92 of $L_{\max}$ (Cox 2006, p. 96–106; Galbraith & Roberts 2012). These coarse boundaries are evaluated by searching for threshold values of σ for which $(L_\sigma - L_{\max}) \leq$ -1.92 from $\widehat{\sigma}$ to either direction with an initial step S_0 (e.g., $S_0 = 5\%$ of $\widehat{\sigma}$) in the profile log-likelihood function (Fig. 3a). This calculation is iterated sequentially with 10% of the previous step as a new value (e.g., 10% of S_0) to resolve finer compatibility intervals (Fig. 3a). A symmetric standard error of $\widehat{\sigma}$ is calculated by dividing the length of this 95% CI by 3.92 when the distribution of σ is assumed to be Gaussian (Cox 2006, p. 64–93; Galbraith & Roberts 2012).

A challenge for luminescence dating is that the usual (natural logarithm transformed) CAM may be unsuitable for young sediments (e.g., < 350 a) because of low signal to noise ratio and the preponderance of negative D_e values (Arnold et al., 2009; Galbraith & Roberts, 2012). Consequently, an un-logged central age model (CAM-ul) was de-

signed for samples which contains grains with near-zero or negative D_e values (Arnold et al., 2009). In this case, the d_i is the original D_e values for each aliquot or grain i, and the σ_{w_i} is the absolute rather than relative standard error. The absolute overdispersion and 95% CI is calculated and shown graphically as a profile log-likelihood function (Fig. 3b). If the overdispersion $\widehat{\sigma}$ for CAM-ul equals 0, the estimate δ given by Eq. 11 is mathematically equivalent to 'inverse variance weighted mean' of the observed D_e values (Taylor 1997, p. 173–179; Galbraith & Roberts 2012).

4.2. Minimum age models

4.2.1 Statistical principle of minimum ages models

The minimum age model (MAM) is designed for sediments that contain a mixture of grains with different solar-resetting histories, with inherent varying luminescence emissions (Galbraith et al., 1999; Galbraith & Roberts, 2012). Though mineral grains in a sedimentary unit may have an equivalent burial time, the component grains yield varying equivalent doses, indicating grain populations were not fully solar reset prior to burial (Galbraith et al., 1999; Preusser et al., 2009). These partially bleached sediments are typically characterized by high overdispersion (>0.25) of D_e distributions (Rodnight, 2008; Galbraith & Roberts, 2012). In such cases, the MAM may be most suitable to determine the D_e for the burial period. The MAM assumes that the burial $\ln D_e$ values are drawn from a truncated normal distribution, where γ denotes the lower truncation point and corresponds to the average burial $\ln D_e$ of the well solar-reset grains. The proportion of well-bleached grains is denoted by p; the partially bleached grains have larger doses which are drawn from a truncated normal distribution with parameters μ and σ (Galbraith et al., 1999; Galbraith & Roberts, 2012). Note that if the ln D_e distribution were not truncated, it would have a mean μ and a standard deviation σ as δ and σ for the central age model (Galbraith et al., 1999).

For the MAM, LDAC calculates the probability density function f_i for a ln D_e value d_i based on (Galbraith et al., 1999; Galbraith & Roberts, 2012):

$$s_i^2 = {\sigma_{w_i}}^2 + {\sigma_b}^2 \tag{16}$$

$$\mu_* = \frac{\frac{\mu}{\sigma^2} + \frac{d_i}{s_i^2}}{\frac{1}{\sigma^2} + \frac{1}{s_i^2}} \tag{17}$$

$$\sigma_* = \frac{1}{\sqrt{\frac{1}{\sigma^2} + \frac{1}{s_i^2}}} \tag{18}$$

$$f_{1i} = \frac{1}{\sqrt{2\pi {s_i}^2}} \exp\left(-\frac{(d_i-\gamma)^2}{2{s_i}^2}\right) \tag{19}$$

$$f_{2i} = \frac{1}{\sqrt{2\pi\left(\sigma^2+s_i^2\right)}} \frac{1-\Phi\left(\frac{\gamma-\mu_*}{\sigma_*}\right)}{1-\Phi\left(\frac{\gamma-\mu}{\sigma}\right)} \exp\left(-\frac{(d_i-\mu)^2}{2\left(\sigma^2+s_i^2\right)}\right) \tag{20}$$

$$f_i = p f_{1i} + (1-p) f_{2i} \tag{21}$$

where d_i and σ_{w_i} are the same as the parameters in Eqs. 11 and 12; $\Phi(\bullet)$ is the cumulative distribution function of $N(0,\ 1)$; f_{1i} and f_{2i} are the contribution from the well-bleached component and partially bleached component, respectively. Another important parameter in this age model is σ_b in Eq. 16, which is a likely overdispersion for the expected population of well-bleached grains, such as between-grain variation in a heterogenous dose environment ('hot grains') (Jacobs & Roberts, 2007; Guérin et al., 2015). This σ_b is independent of within-grain or aliquot measurement error and inhomogeneous solar resetting (Galbraith et al., 2005; Cunningham & Wallinga, 2012). An appropriate σ_b is difficult to measure for mixed grain populations with variable D_e but can be assessed from well solar reset mineral grains from the same source (Galbraith & Roberts, 2012). Overestimating or underestimating the σ_b will lead to corresponding older and younger age estimates. In LDAC, we use a default σ_b of 0.11 ± 0.04 (11 ± 4%) for multi-grain data consistent with the value recommended by Cunningham & Wallinga (2012). However, it is advised to evaluate σ_b for each sample dated (Galbraith et al., 2005; Cunningham & Wallinga, 2012). Thus, users can input other σ_b values in the "MAM-MAX" worksheet (Supplement A). Hence, the four unknown parameters p, γ, μ and σ in Eqs. 16–21 can be estimated when the log-likelihood L is a maximum, where

$$L(d_i,\ \sigma_{w_i}|p,\ \gamma,\ \mu,\ \sigma) = \sum_{i=1}^{n} \ln f_i. \tag{22}$$

Some data sets with a small number of valid values or less dispersed distributions, may be uncalculatable with the above four-parameters model (MAM-4). Thus, it may be suitable to apply a simpler three parameters model in which $\mu = \gamma$ (MAM-3) (Galbraith et al., 1999). As with the CAM, this natural logarithm-transformed MAM may be unsuitable for sediments that have a D_e <0.50 Gy, with significant zero and negative values which are consistent with zero dose within 2 standard errors (Arnold et al., 2009; Galbraith & Roberts, 2012). In this case, the un-logged minimum age model (MAM-ul) is used, which supposes that the actual D_e instead of $\ln D_e$ values are drawn from a truncated normal distribution, where γ denotes the lower truncation point and corresponds to the average burial D_e of well-bleached grains (Arnold et al., 2009). Thus, the parameters d_i and σ_{w_i} in Eqs. 16–22 are referred to the actual dose and absolute standard error, rather than log-transformed and relative standard error scale. Likewise, the σ_b of MAM-ul in Eq. 16 is the absolute overdispersion (Gy) instead of the relative overdispersion (%) of well-bleached grains.

4.2.2 Markov chain Monte Carlo slice sampling for parameters estimation

There is need for computational tools to estimate the four parameters p, γ, μ and σ for the MAM (Eqs. 16–22). Often these values and associated standard errors are computed numerically through an optimization program such as Fortran program 'minim' (Galbraith et al., 1999) or maximum

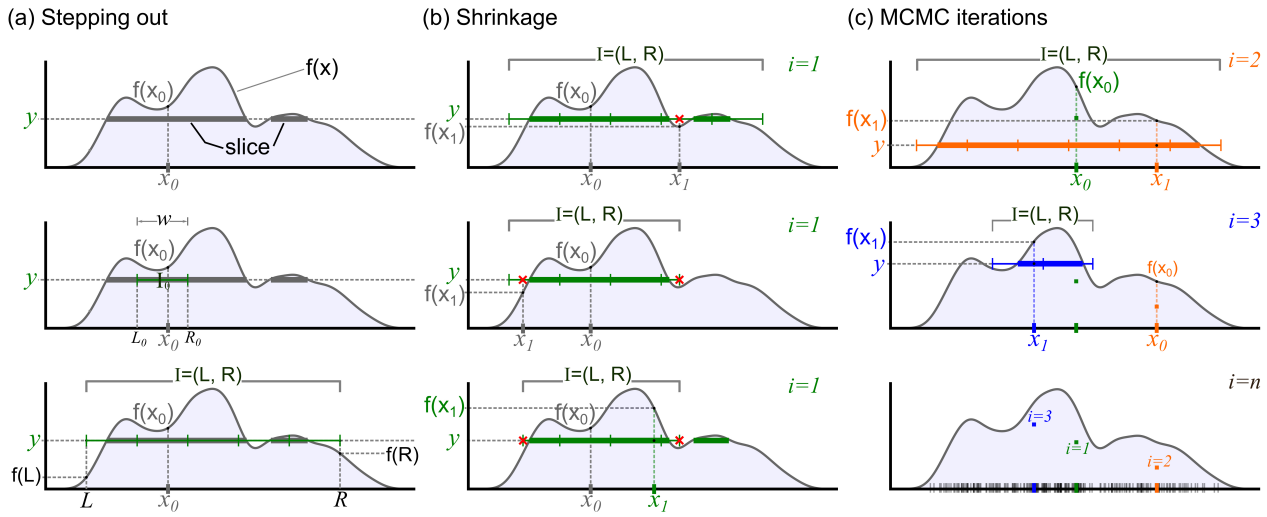

Figure 4. Procedures for estimating the parameters for the minimum age model (Galbraith & Roberts, 2012) using Markov chain Monte Carlo (MCMC) slice sampling method (Neal, 2003). (a) Processes for defining the "slice" (bold line), positioning an initial interval I_0, and expanding the I_0 to $I = (L, R)$ in incremental steps w to include the slices as more as possible. (b) Initiate a calculation at point x_1 uniformly from the interval I until a value is found inside the slice. Values outside the slice (e.g., the red dots "×") are used to shrink the interval. (c) MCMC iterations using the procedures of (a) and (b) to obtain the distribution of f(x).

likelihood estimation package `'bbmle'` in **R** (Bolker & R Development Core Team, 2017). However, these packages are incompatible with an Excel VBA-based computational system. A well-adapted replacement is through 'slice sampling' based on the Markov chain Monte Carlo (MCMC) method (Gilks et al. 1996; Neal 2003; Brooks et al. 2011, p. 215–219; Peng et al. 2013), which was initially used by an **R** package `'numOSL'` to solve the MAM parameters (Peng et al., 2013). The basis of this algorithm is that any unknown distribution can be obtained by sampling uniformly from a region under a probability distribution curve, applying an MCMC algorithm (Neal 2003; Vermeesch 2007; Fig. 4). The procedures of single-variable slice sampling are outlined in Table 1 and shown in Fig. 4 (Neal, 2003).

The advantage of the slice sampling is that it is appropriate for a single-variable distribution (Neal, 2003). This computation is adept at sampling a multivariate distribution such as $L(x)$ in Eq. 21 for $x = (p, \gamma, \mu, \sigma)$, by repeatedly updating each variable in turn (Neal, 2003). This slice sampling method is more efficient through 'stepping out' and 'shrinkage' procedures (Neal, 2003) than the other Markov chain methods such as Gibbs sampling (Gelfand & Smith, 1990) and adaptive-rejection Metropolis sampling methods (Gilks et al., 1995; Vermeesch, 2007). In LDAC, the MCMC slice sampling (Table 1) is used to estimate the maximum likelihood parameters for the MAM, based on Eq. 21 and rotationally update parameters (Table 2).

The fundamental prerequisite for applying the MCMC algorithm to estimate parameters and associated uncertainties for a distribution is that the Markov chain attains convergence states (Gilks et al. 1996; Cowles & Carlin 1996; Neal 2003; Brooks et al. 2011, p. 163–174). Several diagnostic tools can be applied to assess the steps for value convergence (Cowles & Carlin, 1996). In LDAC, trace plot, marginal density, and autocorrelation function (ACF) are employed to evaluate the convergence states of a Markov chain analysis (Fig. 5). A trace plot shows the trajectories at each MCMC iteration and is a straightforward graphic to assess the convergence of a Markov chain (Gilks et al., 1996; Plummer et al., 2006; Philippe et al., 2019). The Markov chain reached a stable state if the trace plot displays a random distribution with a relatively constant mean and variance (Brooks et al. 2011, p. 163–174; Philippe et al. 2019). In LDAC, the default number of iterations is $n = 1800$, which balances the convergence, precision, and efficiency of the MAM calculations. An unsuitable initial value affects the initial behavior of a Markov chain within finite iterations (see Fig. 5). Thus, we use a 'burn-in' strategy (Gilks et al. 1996; Brooks et al. 2011, p. 19–23), which discards the first t iterations of a Markov chain analysis, to reduce the influence of initial values and use exclusively the stationary values for estimation of parameters. Another graphical assessment method is the autocorrelation function, which monitors the correlation between states of the Markov chain (Brooks et al. 2011, p. 163–174). High sampling autocorrelation may result in a biased standard error for Monte Carlo iterations (Gilks et al., 1996). LDAC computations use a conventional 'thinning' method (Gilks et al. 1996; Brooks et al. 2011, p. 163–174), with every kth iteration stored, to reduce autocorrelation between consecutive iterations. The default values for burn-in and thinning in LDAC are 200 and 4, respectively. Consequently, the number of MCMC iterations used for final parameter estimation is $[(n-t)/k]$ (in LDAC, 400). Users can adjust (increase) the default values for Monte Carlo iterations, burn-in inter-

Table 1. The 'stepping out' and 'shrinkage' procedures for Markov chain Monte Carlo (MCMC) slice sampling method for Minimum Age Model calculations.

Step	Calculation	Notes
1	Give an initial value, x_0, and calculate $f(x_0)$;	x_0 and $f(x_0)$ in Fig. 4a
2	Draw an auxiliary value at vertical level, y ,uniformly from $(0,\ f(x_0))$, thereby defining a horizontal 'slice': $S = \{x : y < f(x)\}$;	The bold gray lines in Fig. 4
3	Give a rough estimate, w, for the scale of S (w is estimated prior to slice sampling and keep constant);	Fig. 4
4	Pick randomly an initial interval $I_0 = (L_0,\ R_0)$, which size equals w, containing x_0;	I_0 is the green line in Fig. 4a and the length of $I_0 = w$
5	Expand the initial interval I_0 by 'stepping out' procedure (Neal, 2003) until $f(L)\ \leq y$ and $f(R) \leq y$; we get an interval as $I = (L,\ R)$;	The thin solid green line in Fig. 4a;
6	Draw a new point x_1 uniformly from the interval I using 'shrinkage' method (Neal, 2003). If the $f(x_1) < y$, reject the value, shrink the interval I and repeat the uniform sampling within the new interval again, until $f(x_1) \geq y$.	The rejection points and shrinkage procedures are illustrated in Fig. 4b.
7	Set the new point x_1 as current point x_0 and return to 1.	The MCMC iteration is illustrated in Fig. 4b,c

Table 2. Protocol for applying the single-variable slice sampling method outlined in Table 1 to estimate parameters from a multivariable distribution.

Step	Procedure	Calculation
1	Calculate the lower and upper limits of p, γ, μ, σ;	$p \in [0,\ 1]$; $\gamma \in [\min(d_i),\ max(d_i)]$; $\mu \in [\min(d_i),\ max(d_i)]$; $\sigma \in [0,\ 10]$;
2	Give initial values of p, γ, μ, σ within their range;	$p_0, \gamma_0, \mu_0, \sigma_0$; both default and user-defined values are available;
3	Calculate new points $p_1, \gamma_1, \mu_1, \sigma_1$ using the single-variable slice sampling method and save these values in a matrix $[j,k]$ (j represents the time of iterations; k represents the number of parameters);	$p_1 = \text{slice sampling}\,(L(p_0 \mid \gamma_0, \mu_0, \sigma_0, d_i, \sigma_{w_i}))$; $\gamma_1 = \text{slice sampling}\,(L(\gamma_0 \mid p_1, \mu_0, \sigma_0, d_i, \sigma_{w_i}))$; $\mu_1 = \text{slice sampling}\,(L(\mu_0 \mid p_1, \gamma_1, \sigma_0, d_i, \sigma_{w_i}))$; $\sigma_1 = \text{slice sampling}\,(L(\sigma_0 \mid p_1, \gamma_1, \mu_1, d_i, \sigma_{w_i}))$;
4	Set $p_1, \gamma_1, \mu_1, \sigma_1$ as new $p_0, \gamma_0, \mu_0, \sigma_0$ and return to 2;	Start Markov chains iteration $j+1$ until hit the limit on iterations.

Note: slice sampling (•) is a single-variable slice sampling calculation function based on Table 1.

actions and thinning to ensure the convergence states are reliably reached. Finally, the central value and 95% CI of the estimated parameters are calculated based on the arithmetic mean, 2.5% and 97.5% quantiles from the stationary MCMC results (Brooks et al. 2011, p. 175–197). The standard errors of parameters are estimated by dividing the length of 95% CI by 3.92 (Cox 2006, p. 64–93; Galbraith & Roberts 2012).

4.2.3 Validation of slice sampling MAM

A simulated data set was fabricated by mixing D_e data of two disparate samples to test the veracity of the slice sampling for resolving the youngest D_e population by the MAM. The first sample is well-bleached quartz grains with an overdispersion of 4 ± 2 % and a D_e (CAM) of 47.7 ± 0.7 Gy (n = 30) (Table 3; Fig. 6a). The second sediment is poorly-bleached and contains three significant D_e components, displaying a high overdispersion (37 ± 3%) with an apparent D_e (CAM) of 158.5 ± 7.1 Gy (n = 70) (Table 3; Fig. 6b). The two simulated sediments have an average relative standard error of 6 ± 1.5% (Fig. 6). The two data sets are combined (n = 100), and the aliquots from each sample are traced by two different colors: red for well solar reset data set and green for the high dispersed data (see Fig. 6c). The overdispersion of this mixed, synthetic sample is 63 ± 5 % and the apparent D_e calculated by CAM is 110.4 ± 7.0 Gy (Fig. 6c).

The slice-sampled MAM approach was tested using the MAM-4 computations in LDAC. A total of 1800 iterations of MCMC slice sampling were implemented. The first 200 iterations of the MCMC were discarded ('burn-in') and ap-

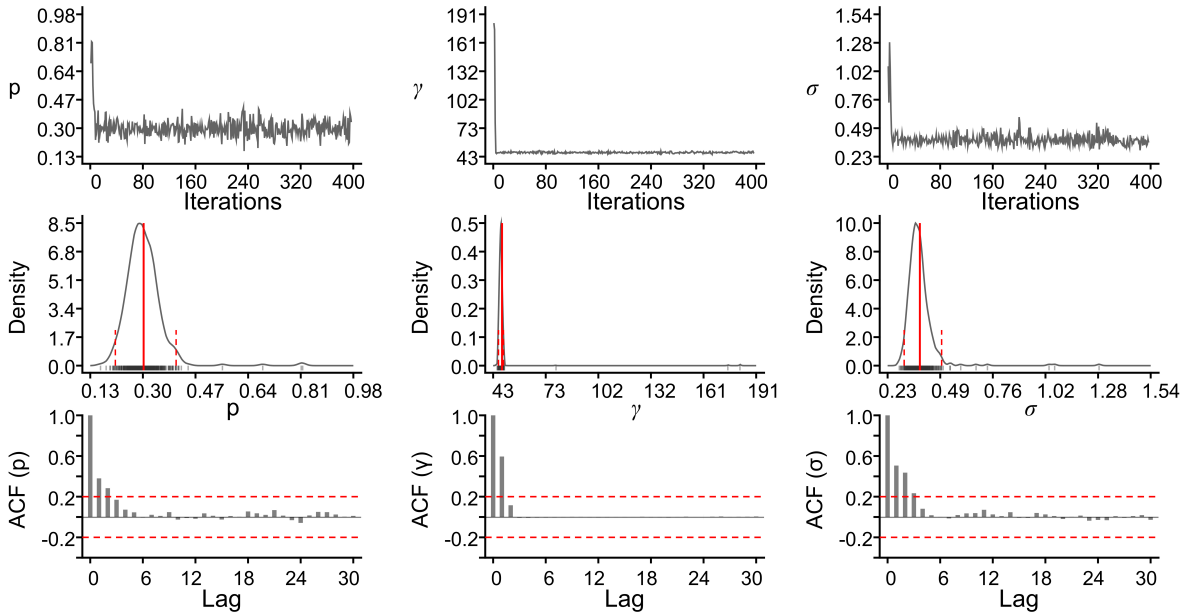

Figure 5. An example of Markov chain Monte Carlo sampling without 'burn-in' and 'thinning' showing graphical diagnostics such as trace plots (upper), marginal densities (middle) and evaluation of autocorrelation (ACF) (lower). There is high autocorrelation until after lag-3 analysis.

plied a data thinning routine of registering every 4th value to avoid autocorrelation. The trace, KDE and autocorrelation plots demonstrate stationarity of the Markov chain analysis (Fig. 7). Finally, 400 iterations (after burn-in and thinning) were used to estimate p, γ, μ and σ and their 95% CI (Table 3; Fig. 7). The default initial values given by MAM-4 in this experiment are $p_0 = 0.5$, $\gamma_0 = 3.93$ (normal scale: 50.91 Gy), $\mu_0 = 4.7$ (normal scale: 109.95 Gy) and $\sigma = 4.87$. The σ_b is 0.0438 $\pm$ 0.0173 which is the overdispersion of the well-bleached component of this synthetic sample (Fig. 6a). The results of this experiment indicate that the slice sampling MAM can reliably separate the lowest synthetic D_e associated with the well solar-reset subpopulation (Table 3).

4.3. Maximum age models

The maximum age model (MAX) was proposed for sediments that are suspected to be disturbed or mixed by processes that lead to partial or full solar resetting of grains post deposition, such as pedogenesis or other biogenic activities (Olley et al., 2006; Galbraith & Roberts, 2012; Ahr et al., 2013). The MAX computation model shares the same assumption and statistical principle with the MAM (section 4.2.1), but the γ is defined as the upper truncation point of the truncated log-normal distribution of true D_e values (Olley et al., 2006; Galbraith & Roberts, 2012). As with the MAM, LDAC provides three and four parameters maximum age models (MAX-3 and MAX-4, respectively) following the method developed by Olley et al. (2006). The same equations and parameters estimation methods as the MAM are used, but the d_i in Eqs. (16-22) is changed to

$$d_i = -\ln \mathrm{De}_i + \ln\left[\mathrm{Max}\left(\mathrm{De}\right)\right], \qquad (23)$$

where De_i is the observed value from single aliquot or grain i, $Max(De)$ is the maximum value of all observed D_es. The purpose of this conversion process is to create a 'mirror image' of the original data distribution (Olley et al., 2006).

Table 3. The results of slice sampling for Minimum Age Model-4 (MAM-4) for the simulated sample.

Parameters	Known values ($\pm$ 1 σ)	MAM-4 estimates (LDAC)	
		Asymmetric CI (95%)	Standard error ($\pm$ 1 σ)
p	0.30	$0.300^{+0.10}_{-0.08}$	0.300 $\pm$ 0.045
γ	47.66 $\pm$ 0.65 Gy	$47.59^{+1.46}_{-1.30}$ Gy	47.59 $\pm$ 0.71 Gy
μ	158.49 $\pm$ 7.10 Gy	$157.17^{+14.08}_{-16.37}$ Gy	157.17 $\pm$ 7.77 Gy
σ	0.37 $\pm$ 0.03	$0.386^{+0.07}_{-0.06}$	0.386 $\pm$ 0.033

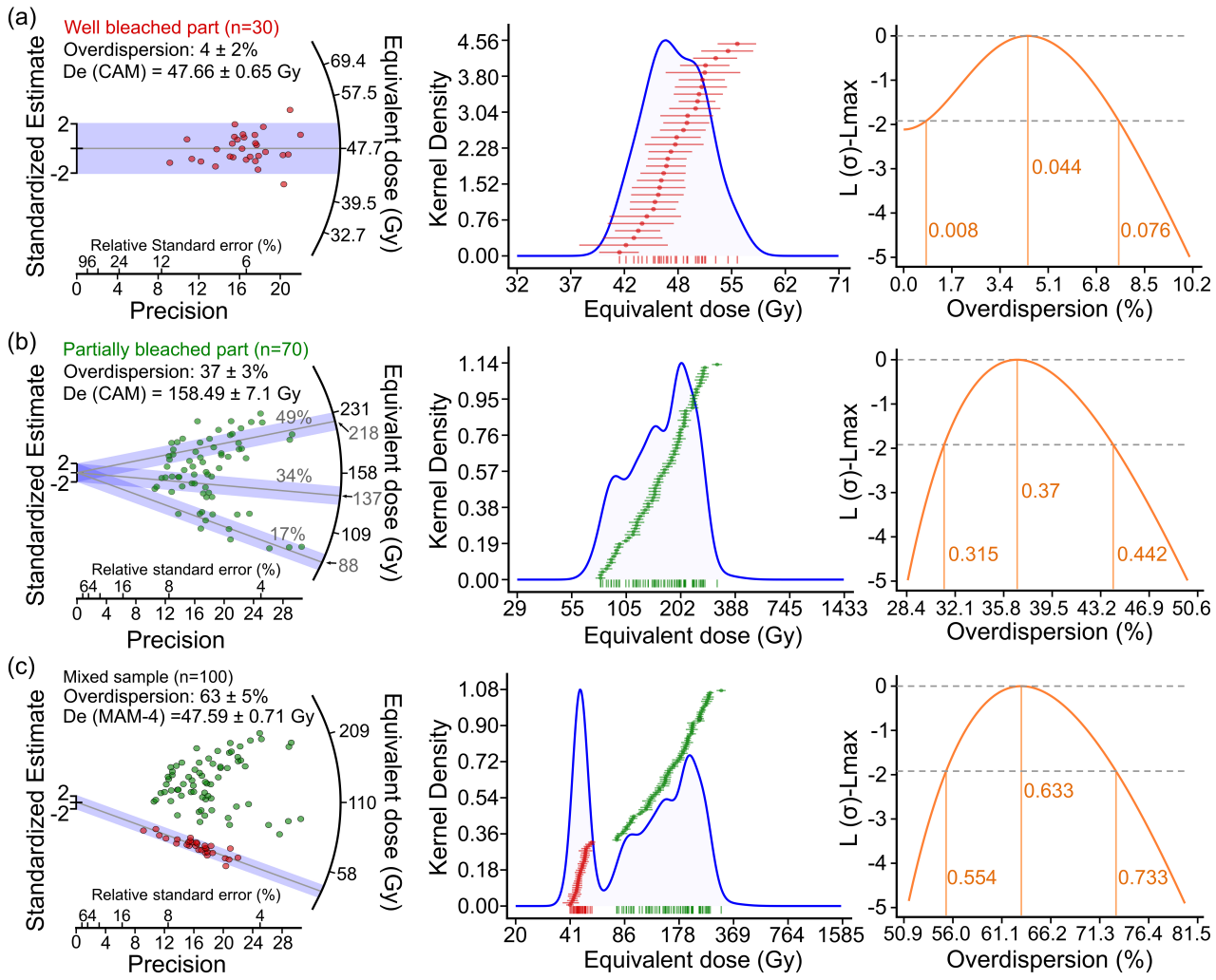

Figure 6. The unmixed (a and b) and mixed (c) simulant samples used in validation for Minimum Age Model (MAM). (a) shows equivalent dose distribution of a well solar reset component with 4 ± 2% overdispersion; (b) illustrates partially solar reset component which includes three sub-populations and with 37 ± 3% overdispersion. (c) Distribution of the mixed sample and the MAM-4 result.

As with the MAM, the MCMC slice sampling method (section 4.2.2) is used to estimate the upper truncation point, γ. The σ_b value is vital for the accuracy of MAX, and this value can be estimated from the associated parameters for well-bleached equivalent grains (Olley et al., 2006).

5. Environmental dose rate (D_r) and final age calculation

The environmental D_r of sediments that induces luminescence is from α, β and γ radiations from the radiative decay of the U and Th series, ^{40}K, ^{87}Rb and from cosmic-galactic components (Aitken 1985, chapter 4). The D_r is often calculated from the concentrations of radionuclides in the surrounding sediments within 30 cm radius of the sampling site based on the assumptions of an infinite matrix and secular equilibrium in the U and Th series (Aiken, 1998, p. 37–41; Guérin et al. 2012). The total environmental D_r for a particular grain size includes attenuation of external and internal dose contributions for grain-size, chemical etching of the alpha-affected outer 5 to 10 µm of grains and inferred sediment water content during the burial period, and cosmic dose components. The calculations for D_r in LDAC are similar to DRAC (Durcan et al., 2015), but with modifications discussed below.

5.1. Conversion and attenuation factors

LDAC offers three conversion factor options for dose contributions from α, β and γ components, as an infinite matrix dose, including 'Adamiec1998' (Adamiec & Aitken, 1998), 'Guérin2011' (Guérin et al., 2011) and 'Liritzis2013' (Liritzis et al., 2013) (worksheet 6 in Fig. 1). The given conversion factors assume secular equilibrium of U and Th decay series with no Radon loss (Aitken 1985, chapter 4). The uncertainties of the conversion factors derived from Liritzis et al. (2013) are applied proportional to the three data sets

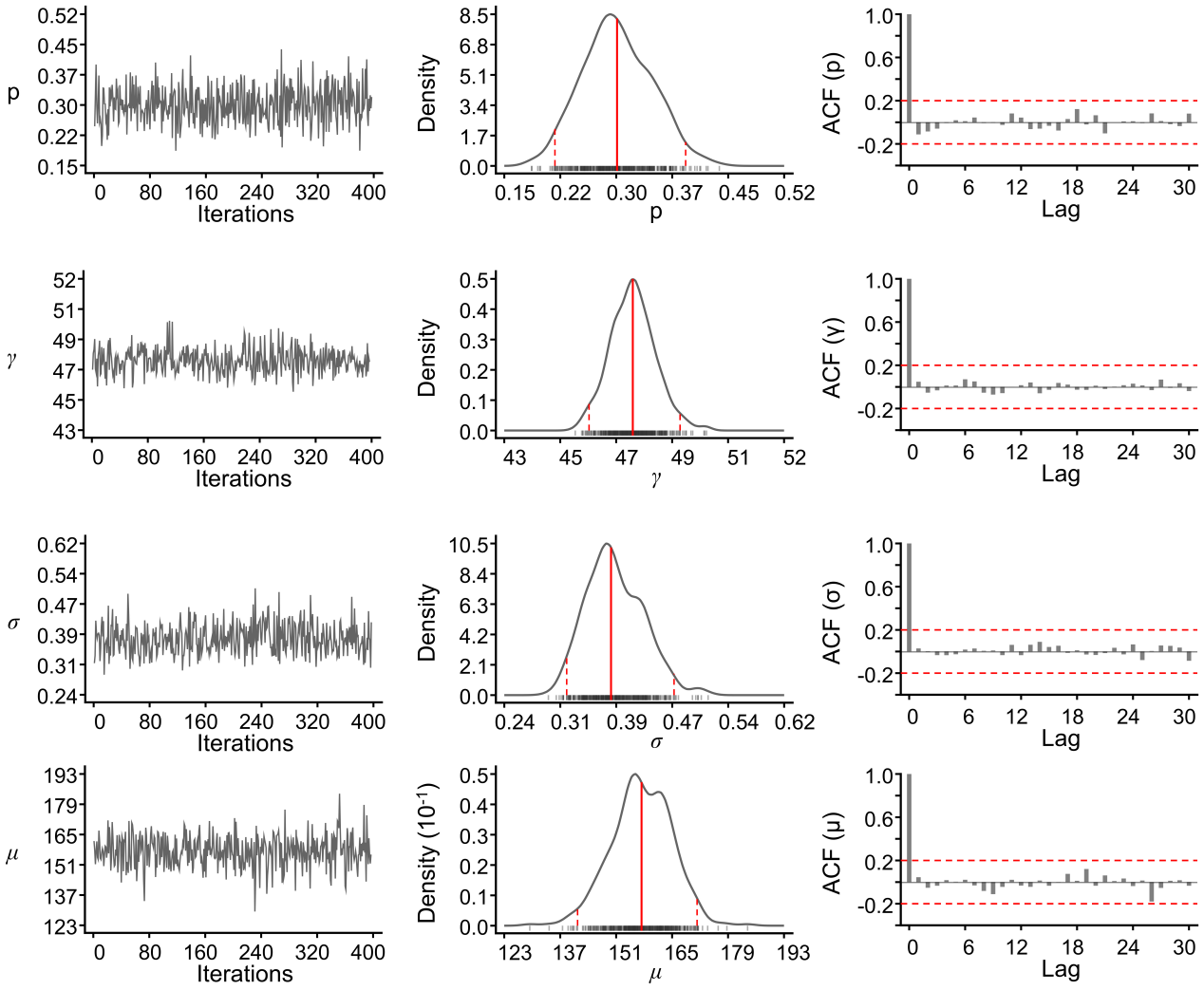

Figure 7. Estimation of the parameters p, γ, σ, and μ in minimum age model-4 for the simulant sample of Fig. 6c using the Markov chain Monte Carlo slice sampling method. The iteration times, burn-in, and thinning are 1800, 200 and 4, respectively.

following (Durcan et al., 2015). Users are required to input concentrations of U, Th, Rb in ppm and K or K_2O in % in the "Summary" page. The internal radionuclide concentration or dose rates and user-specified dose rates estimated through other methods, such as beta counting (Cunningham et al., 2018), can be input in the bottom panel of the "Summary" page and incorporated into subsequent attenuation as an option (Supplement A).

Several attenuation factors are considered in dose rate calculations including by grain size, from chemical etching (e.g., HF) of grain surface, by water content and a-value for alpha radiation (Aitken 1985, p. 252–263). Previously vetted attenuation factors are used in LDAC (e.g. Durcan et al. 2015) (worksheets 7-10 in Fig. 1). The default parameters for α and β attenuation by grain size and after chemical etching are from Brennan et al. (1991), Guérin et al. (2012), Bell (1980) and Brennan (2003), respectively. Alternative earlier parameters can be chosen on the "Summary" page (Supplement A) for β attenuation by grain size (Mejdahl, 1979; Brennan, 2003) to facilitate D_r comparison with previously published calculations. Grain size attenuation effects for α and β radiation is corrected with a resolution of 1 μm and a grain size range of 1 to 1000 μm (worksheet 7-8; Durcan et al. 2015). The factors and associated uncertainties are determined for the mean value and associated standard deviations corresponding to a grain size range (e.g., 150–250 μm). Similarly, the chemical etching attenuation factors are calculated with 1 μm resolution to a removal depth of 1 to 30 μm (worksheet 9-10; Durcan et al. 2015). A γ scaling factor is used to correct the contribution from inert air, for sediments collected at depths from < 30 cm of the ground surface (Aitken 1985, p. 289–296; Durcan et al. 2015; worksheet 11 in Fig. 1). These attenuated dry dose rates are adjusted for the water content with the attenuation factors for α, β and γ of 1.49, 1.25 and 1.14, respectively (Aitken 1985, p. 74–76; Grün 1994; Durcan et al. 2015).

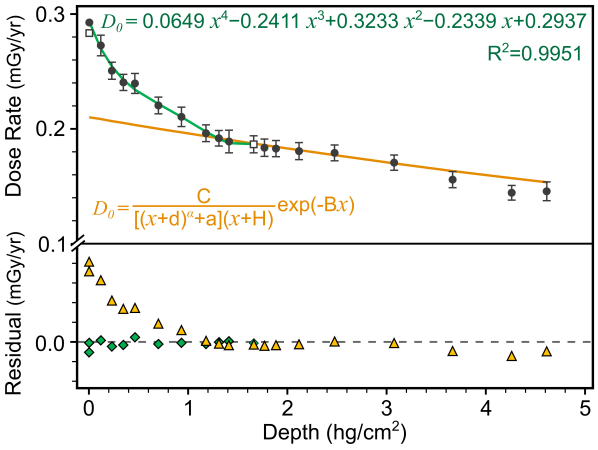

Figure 8. Standard cosmic dose rate (D_0) at different depths below surface. The black dots are the original measured data from bryozoan limestone in the southeast of South Australia (Prescott & Hutton, 1988). The white square data point at 1.67 hg/cm^2 is from Barbouti & Rastin (1983), and the white square at zero depth is from Kyker & Liboff (1978). The green and orange line show fitted curved defined by Eq. 24 and Eq. 25, respectively. The lower panel shows the D_0 residual between measured and fitted data. The constants of the equation are C = 6072, B = 5.50×10^{-4}, d = 11.6, α = 1.68, a = 75 and H = 212 (Prescott & Hutton, 1994).

5.2. Cosmic Dose Rate

The cosmic dose rate (D_c) is an integral part of the evaluation of the D_r, particularly for low dose sediments. The D_c calculation in LDAC follows the protocol outlined by Prescott & Hutton (1994). The standard cosmic dose rate (D_0) is calculated at sea level at a geomagnetic latitude of 55° for a given depth and overburden density using the following equations:

$$D_0 = 0.0649x^4 - 0.2411x^3 + 0.3233x^2 - 0.2339x + 0.2937, \quad x < 1.67 \text{ hg/cm}^2, \tag{24}$$

or

$$D_0 = \frac{6072}{[(x+11.6)^{1.68}+75](x+212)} e^{-0.00055x}, \quad x \geq 1.67 \text{ hg/cm}^2, \tag{25}$$

where x (hg/cm^2, equals to 100 g/cm^2) is the product of sampling depth below ground surface (m) and average overburden bulk density of the sediments (g/cm^3).

Eq. 25 from Prescott & Hutton (1994) is used to calculate D_0, but as pointed out by the authors, it is not valid for depths shallower than 1.67 hg/cm^2 (Aitken 1985, p. 297–298; Fig. 8). The principal components of the cosmic dose in the atmosphere are ionized electrons and muons, with a negligible contribution from heavier particles (Prescott & Hutton, 1988). The 'soft' component (electrons) of cosmic rays is attenuated with increasing depth into sediments, with penetrating limited at density depth of 1.5 ~ 1.67 hg/cm^2 (Barbouti & Rastin, 1983; Prescott & Hutton, 1988). The remaining 'hard' component (muons) is less readily attenuated, and it can penetrate to considerable depths, with decreasing intensity (Prescott & Hutton, 1988). The prototype of Eq. 25 is an empirical relationship between the vertical muon intensity and depth (Barbouti & Rastin, 1983), and only considers the 'hard' component of the cosmic rays. This equation (Eq. 25) excludes the 'soft' component (electron) of cosmic rays at depth shallower than 1.67 hg/cm^2 (Durcan et al., 2015; Burow, 2018). The residual between the 'hard' and 'soft' data sets for dose attenuation with depth is derived from measured cosmic dose from a bryozoan limestone in southeastern South Australia (orange triangles in Fig. 8). We translated the original measurement values from Figure 1 of Prescott and Hutton (1988) using MATLAB; the data points < 1.67 hg/cm^2 were fitted with a 4-degree polynomial function (Eq. 24; Fig. 8). LDAC adopts Eq. 24 to calculate the D_0 for depth between 0 and 1.67 hg/cm^2, because it includes both the 'soft' and 'hard' components in evaluating the cosmic dose rate, which is an accurate assessment.

The D_0 is then corrected by F, J and H values based on the geomagnetic latitude and altitude for the dated sediment (Prescott & Stephan, 1982; Durcan et al., 2015). The effect of known variations of the geomagnetic field is corrected for dose rate estimates for the late Pleistocene (Prescott & Hutton, 1994). Users can choose an estimated age range (0 – 5, 5 – 10, 10 – 15, 20 – 35, 35 – 50, 50 – 80 and > 80 ka) from the 'Age Estimate' tab (Fig. 9a) in the "Summary" worksheet. This value, together with altitude and the geomagnetic latitude converted from geographical coordinate, are applied to determine the geomagnetic field fluctuation factor (f_g) and altitude factor (f_h) (Prescott & Hutton 1994; Fig. 9). Consequently, the final equation for cosmic dose rate is:

$$D_c = D_0 \cdot (F + J \cdot e^{(h/1000)/H}) \cdot f_h \cdot (f_g - 1) \tag{26}$$

where F, J and H are the correction parameters of altitude and geomagnetic latitude (Prescott & Hutton, 1994; Durcan et al., 2015); h is the altitude of the sampling site (in m a.s.l.); f_g is the correction factors for cosmic ray flux change resulting from geomagnetic fields variations (Fig. 9a); and f_h is the factor for adjusting f_g for altitude (Fig. 9b). LDAC assigns an uncertainty of ± 10% for the calculated D_c (Prescott & Hutton, 1994). User-defined cosmic dose rate can also be input in the "Summary" page, if necessary.

The overburden density influences the accuracy of D_c calculation. LDAC allows users to input an estimated average bulk density different from the default value of 1.6 ± 0.1 g/cm^3, which is based on the investigation of soil dry bulk density, such as loess (1.1 – 1.8 g/cm^3) and aeolian sand (1.3 – 1.8 g/cm^3) with adjustments for field moisture content (Logsdon & Karlen, 2004; Wang et al., 2014).

5.3. Final Age calculation

The D_r is computed by the sum of all attenuated radionuclide components which include D_α^U, D_β^U, D_γ^U, D_α^{Th}, D_β^{Th},

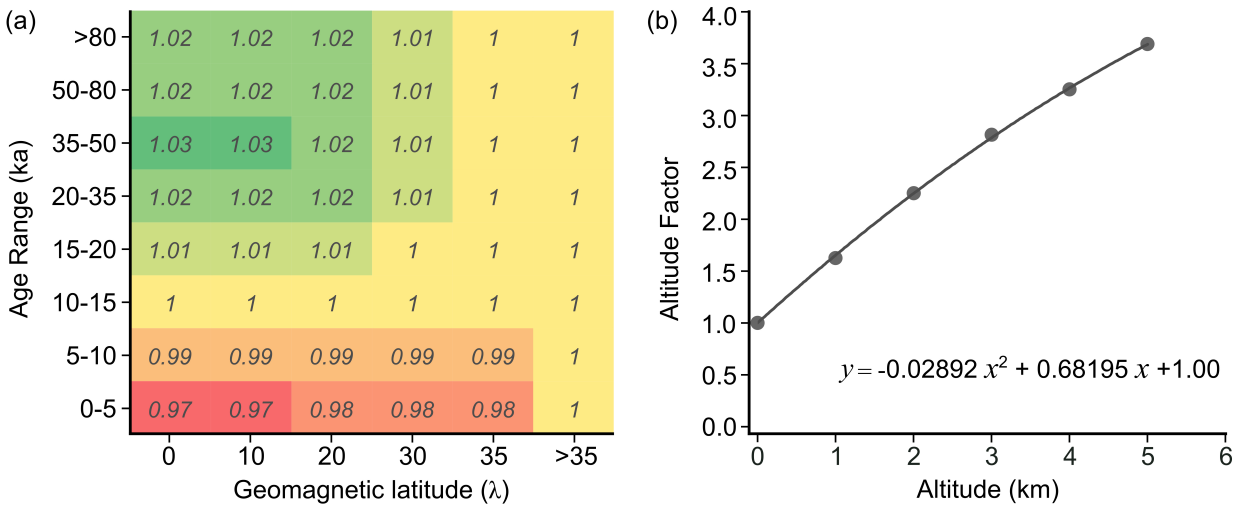

Figure 9. Correction factors for adjusting geomagnetic field variations for time (a) and altitude (b) (Prescott & Hutton, 1994).

D_γ^{Th}, D_β^K, D_γ^K, D_β^{Rb}, and the cosmic dose rate D_c. LDAC calculates the final age based on Eq. 1; the mean dose rate and age is calculated from mean values before rounding to two significant figures. The dose rate and associated uncertainty are reported in the "Summary" page at two significant figures (e.g., 2.75 mGy/yr). The final age is reported to the nearest 5-year increment if < 50 ka and rounded to the nearest 10-year increment for ages > 50 ka, reflecting inherent resolution.

5.4. Error propagation

LDAC provides two approaches to evaluate the uncertainties of the environmental dose rate and hence the final age. The first one is based on quadrature (Aitken 1985, p. 241–251; Taylor 1997, p. 45–92). However, all uncertainties propagated in quadrature will underestimate the total error because parts of dose rate from γ, β and α are correlated, which share the same source of errors from nuclide measurements (Grün 1994; Grün 2009; Taylor 1997, p. 45–92). To overcome this drawback, LDAC computes and attenuates the α, β and γ radiations from each nuclide independently in all steps and propagates the errors in quadrature separately in each step. Until the last step, all errors are combined based on:

$$\sigma_{D_r} = \sqrt{\begin{array}{l}\left(\sigma_{D_\alpha^U}+\sigma_{D_\beta^U}+\sigma_{D_\gamma^U}\right)^2+\left(\sigma_{D_\alpha^{\mathrm{Th}}}+\sigma_{D_\beta^{\mathrm{Th}}}+\sigma_{D_\gamma^{\mathrm{Th}}}\right)^2 \\ +\left(\sigma_{D_\beta^K}+\sigma_{D_\gamma^K}\right)^2+\left(\sigma_{D_\beta^{\mathrm{Rb}}}\right)^2+(\sigma_{D_c})^2\end{array}} \quad (27)$$

$$\sigma_{\mathrm{age}} = Age\sqrt{\left(\frac{\sigma_{D_e}}{D_e}\right)^2+\left(\frac{\sigma_{D_r}}{D_r}\right)^2}, \quad (28)$$

where $\sigma_{D_\beta^U}$ is the uncertainty of attenuated β dose rate (internal and external) emitted by U; it combines the random and systematic errors from nuclide measurement, conversion factors, attenuation factors and water content in quadrature. All other subscript of each σ has a corresponding meaning.

The second method for propagating the uncertainties in the final age estimate from all data sources is through Monte Carlo simulations. This approach is commonly used in numeric analysis to more faithfully propagate the uncertainties that are statistically robust (e.g., Anderson 1976; Duller 2007; Vermeesch 2007; Shao et al. 2014). This analysis assumes that each numeric value of input variables (e.g., U, Th, K, Rb, water contents), conversion and attenuation factors and their associated errors are represented by a Gaussian distribution of possible values. A large amount of repeated D_r and age calculations (e.g., 1000) are undertaken with stochastic values drawn from the independent Gaussian distributions (Shao et al., 2014). The 68.3% CI is evaluated by the 15.85 % and 84.15 % quantiles of outputs of the Monte Carlo simulations, and this asymmetric age interval is available in the final report (Supplement B). The 1σ uncertainties for the D_r and the final age are determined by the standard deviations of the Monte Carlo results (Cox, 2006). The default Monte Carlo iteration times in LDAC is 1000 which can be modified. This Monte Carlo simulation is a stochastic numeric analysis to propagate estimates of the total uncertainties, and thus these uncertainties will vary slightly with each calculation (Duller, 2007). The central values of D_r and OSL age are still calculated based on the input values rather than the mean of the Monte Carlo outputs.

5.5. Comparisons with other calculation packages

All algorithms for equivalent dose and dose rate calculations in LDAC are well developed by the community in the past thirty years. The key merit of the LDAC is assembling the most used functions for calculating the luminescence age to one package. To test the consistency between LDAC (v1.0) and other existing calculation tools, we compared both the D_e and D_r calculated by different published

Table 4. Comparison between equivalent doses (D_e) calculated by LDAC and **R** `'Luminescence'` package. BG4285 is the example data set of LDAC (v1.0) and the 'simulated sample' is the data set used in Section 4.2.3

Sample	Software	CAM		MAM	MAX
		D_e	Overdispersion		
BG4285	LDAC	366.05 ± 10.06	16.43 ± 2.03	325.68 ± 21.90	407.20 ± 27.92
	`'Luminescence'`	366.05 ± 10.06	16.43 ± 2.03	314.27 ± 17.48	NA
Simulated sample	LDAC	110.42 ± 7.02	63.30 ± 4.52	47.59 ± 0.71	237.22 ± 17.28
	`'Luminescence'`	110.42 ± 7.02	63.30 ± 4.52	47.54 ± 1.11	226.52 ± 9.81

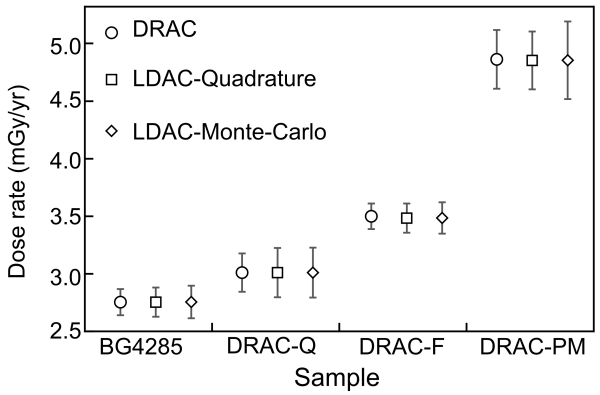

Figure 10. Comparison of dose rates (D_r) calculated by LDAC and DRAC. BG4285 is the example data set in LDAC (v1.0). DRAC-Q, DRAC-F and DRAC-PM are quartz, feldspar and poly-mineral example data sets provided by DRAC (Durcan et al., 2015), respectively. The raw data and used parameters are provided in Supplement D.

software. The comparisons show that our D_e and D_r are consistent with the results calculated by the **R** `'Luminescence'` package and the DRAC within the error range, respectively (Table 4; Fig. 10). However, the standard error of dose rate calculated by LDAC is systematically greater than that of DRAC (Fig. 10), which is caused by the different error propagation strategies stated in Section 5.4.

6. Discussion and Future direction

LDAC is a user-friendly, statistically robust, and self-contained luminescence age calculator which provides equivalent dose, environment dose rate, and final age calculations. This platform is accessible in a Windows environment equipped with Microsoft Excel 2010 or later. The framework of this software openly defines the calculation processes and input and output parameters. This Excel-based program, beyond a calculation tool, can be an effective manager of OSL data. Users can store the parameters of SAR sequences, individual aliquot or grain D_e values, dose rate information, pertinent diagnostic metrics on data quality and other analytical results as a separate LDAC file for each dated sediment. LDAC requires users to input or import their measured data just one time, which can reduce potential mistakes in exchanging data among multiple calculation programs.

This is the first generation of LDAC as an open-source and free access luminescence age calculation software. We plan to further develop and refine this software with advances in luminescence dating and community input. This calculation platform will also evolve for dating and research applications with improvements to the Microsoft Excel. The conversion and attenuation factors for dose rate calculation will be updated to reflect periodic refinements. Moreover, future additions of LDAC may include new statistical models (e.g., Guérin et al. 2017) for assessing disequilibrium of U and Th decay series and improved formulations for variations in cosmic and galactic radiation with fluctuations of Earth's magnetic field. Improving the calculation efficiency of Monte Carlo simulation is also a direction of future optimization.

Acknowledgments

This work was supported by the China Scholarship Council (awarded to P.L.), the National Natural Science Foundation of China (#41430532), the State Scientific Survey Project of China (#2017FY101001), USA National Science Foundation Award #GSS-1660230 (SLF), National Geographic Society Award #9990-16 (SLF), and the Geoluminescence Dating Research Laboratory at Baylor University, USA. Sincere thanks are extended to Liliana Marin for discussion and proofreading the manuscript and to Professor Geoff A.T. Duller for his very valuable comments and suggestions.

References

Adamiec, G. and Aitken, M. J. *Dose-rate conversion factors: update*. Ancient TL, 16: 37–50, 1998.

Ahr, S. W., Nordt, L. C., and Forman, S. L. *Soil genesis, optical dating, and geoarchaeological evaluation of two upland Alfisol pedons within the Tertiary Gulf Coastal Plain*. Geoderma, 192: 211–226, 2013.

Aitken, M. J. *Thermoluminescence dating*. Academic Press, Orlando, Florida, 1985.

Aitken, M. J. *Introduction to optical dating: the dating of Quaternary sediments by the use of photon-stimulated luminescence*. Oxford University Press, New York, 1998.

Anderson, G. *Error propagation by the Monte Carlo method in geochemical calculations.* Geochimica Cosmochimica Acta, 40: 1533–1538, 1976.

Arnold, L. J. and Roberts, R. G. *Stochastic modelling of multi-grain equivalent dose (De) distributions: Implications for OSL dating of sediment mixtures*. Quaternary Geochronology, 4: 204–230, 2009.

Arnold, L. J., Bailey, R. M., and Tucker, G. E. *Statistical treatment of fluvial dose distributions from southern Colorado arroyo deposits*. Quaternary Geochronology, 2: 162–167, 2007.

Arnold, L. J., Roberts, R. G., Galbraith, R. F., and DeLong, S. B. *A revised burial dose estimation procedure for optical dating of young and modern-age sediments*. Quaternary Geochronology, 4: 306–325, 2009.

Bailey, R. M. and Arnold, L. J. *Statistical modelling of single grain quartz De distributions and an assessment of procedures for estimating burial dose*. Quaternary Science Reviews, 25: 2475–2502, 2006.

Balco, G., Stone, J. O., Lifton, N. A., and Dunai, T. J. *A complete and easily accessible means of calculating surface exposure ages or erosion rates from ^{10}Be and ^{26}Al measurements*. Quaternary Geochronology, 3: 174–195, 2008.

Barbouti, A. and Rastin, B. *A study of the absolute intensity of muons at sea level and under various thicknesses of absorber*. Journal of Physics G: Nuclear Physics, 9: 1577, 1983.

Bell, W. *Alpha dose attenuation in quartz grains for thermoluminescence dating*. Ancient TL, 12: 4–8, 1980.

Bolker, B. and R Development Core Team. *bbmle: Tools for General Maximum Likelihood*. R package version, 1.0.20, 2017. URL https://CRAN.R-project.org/package=bbmle.

Botev, Z. I., Grotowski, J. F., and Kroese, D. P. *Kernel density estimation via diffusion*. Annals of Statistics, 38: 2916–2957, 2010.

Bøtter-Jensen, L., McKeever, S. W. S., and Wintle, A. G. *Optically stimulated luminescence dosimetry*. Elsevier, 2003.

Brennan, B. *Beta doses to spherical grains*. Radiation Measurements, 37: 299–303, 2003.

Brennan, B., Lyons, R., and Phillips, S. *Attenuation of alpha particle track dose for spherical grains*. International Journal of Radiation Applications and Instrumentation. Part D. Nuclear Tracks and Radiation Measurements, 18: 249–253, 1991.

Brooks, S., Gelman, A., Jones, G., and Meng, X.-L. *Handbook of Markov chain Monte Carlo*. CRC Press, 2011.

Burow, C. *calc_ CosmicDoseRate(): Calculate the cosmic dose rate. Function version 0.5.2*. In Kreutzer, S., Burow, C., Dietze, M., Fuchs, M., Schmidt, C., Fischer, M., and Friedrich, J. (eds.), *Luminescence: Comprehensive Luminescence Dating Data Analysis. R package version 0.8.6*. 2018. URL https://CRAN.R-project.org/package=Luminescence.

Burow, C., Kreutzer, S., Dietze, M., Fuchs, M. C., Fischer, M., Schmidt, C., and Brückner, H. *RLumShiny-A graphical user interface for the R Package 'Luminescence'*. Ancient TL, 34: 22–32, 2016.

Cowles, M. K. and Carlin, B. P. *Markov chain Monte Carlo convergence diagnostics: a comparative review.* Journal of the American Statistical Association, pp. 883–904, 1996.

Cox, D. *Principles of statistical inference*. Cambridge University Press, New York, 2006.

Cunningham, A. C. and Wallinga, J. *Realizing the potential of fluvial archives using robust OSL chronologies*. Quaternary Geochronology, 12: 98–106, 2012.

Cunningham, A. C., Murray, A. S., Armitage, S. J., and Autzen, M. *High-precision natural dose rate estimates through beta counting*. Radiation Measurements, 120: 209–214, 2018.

Duller, G. A. T. *Distinguishing quartz and feldspar in single grain luminescence measurements*. Radiation Measurements, 37: 161–165, 2003.

Duller, G. A. T. *Assessing the error on equivalent dose estimates derived from single aliquot regenerative dose measurements*. Ancient TL, 10: 15–24, 2007.

Duller, G. A. T. *The Analyst software package for luminescence data: overview and recent improvements*. Ancient TL, 33: 35–42, 2015.

Duller, G. A. T. *Enhancing Analyst by integrating the R package 'Luminescence'*. Ancient TL, 36: 1–6, 2018.

Durcan, J. A. and Duller, G. A. T. *The fast ratio: A rapid measure for testing the dominance of the fast component in the initial OSL signal from quartz*. Radiation Measurements, 46: 1065–1072, 2011.

Durcan, J. A., King, G. E., and Duller, G. A. T. *DRAC: Dose Rate and Age Calculator for trapped charge dating*. Quaternary Geochronology, 28: 54–61, 2015.

Forman, S. L. *Episodic eolian sand deposition in the past 4000 years in Cape Cod National Seashore, Massachusetts, USA in response to possible hurricane/storm and anthropogenic disturbances*. Frontiers in Earth Sciences, 3: 3, 2015.

Forman, S. L., Tripaldi, A., and Ciccioli, P. L. *Eolian sand sheet deposition in the San Luis paleodune field, western Argentina as an indicator of a semi-arid environment through the Holocene.* Palaeogeography, Palaeoclimatology, Palaeoecology, 411: 122–135, 2014.

Galbraith, R., Roberts, R., and Yoshida, H. *Error variation in OSL palaeodose estimates from single aliquots of quartz: a factorial experiment*. Radiation Measurements, 39: 289–307, 2005.

Galbraith, R. F. *Graphical display of estimates having differing standard errors*. Technometrics, 30: 271–281, 1988.

Galbraith, R. F. *The radial plot: graphical assessment of spread in ages*. International Journal of Radiation Applications and Instrumentation. Part D. Nuclear Tracks and Radiation Measurements, 17: 207–214, 1990.

Galbraith, R. F. *A simple homogeneity test for estimates of dose obtained using OSL*. Ancient TL, 21: 75–77, 2003.

Galbraith, R. F. *Statistics for fission track analysis*. Chapman and Hall/CRC, 2005.

Galbraith, R. F. *On plotting OSL equivalent doses*. Ancient TL, 28: 1–10, 2010.

Galbraith, R. F. and Green, P. *Estimating the component ages in a finite mixture*. International Journal of Radiation Applications and Instrumentation. Part D. Nuclear Tracks and Radiation Measurements, 17: 197–206, 1990.

Galbraith, R. F. and Roberts, R. G. *Statistical aspects of equivalent dose and error calculation and display in OSL dating: an overview and some recommendations*. Quaternary Geochronology, 11: 1–27, 2012.

Galbraith, R. F., Roberts, R. G., Laslett, G. M., Yoshida, H., and Olley, J. M. *Optical dating of single and multiple grains of quartz from Jinmium rock shelter, northern Australia: Part I, experimental design and statistical models*. Archaeometry, 41: 339–364, 1999.

Gelfand, A. E. and Smith, A. F. *Sampling-based approaches to calculating marginal densities*. Journal of the American Statistical Association, 85: 398–409, 1990.

Gilks, W. R., Best, N., and Tan, K. *Adaptive rejection Metropolis sampling within Gibbs sampling*. Journal of the Royal Statistical Society. Series C (Applied Statistics), 44: 455–472, 1995.

Gilks, W. R., Richardson, S., and Spiegelhalter, D. *Markov chain Monte Carlo in practice*. Springer-Science+Business Media, Dordrecht, 1996.

Grün, R. *A cautionary note: use of 'water content' and 'depth for cosmic ray dose rate' in AGE and DATA programs*. Ancient TL, 12: 50–51, 1994.

Grün, R. *The "AGE" program for the calculation of luminescence age estimates*. Ancient TL, 27: 45–46, 2009.

Guérin, G., Mercier, N., and Adamiec, G. *Dose-rate conversion factors: update*. Ancient TL, 29: 5–8, 2011.

Guérin, G., Mercier, N., Nathan, R., Adamiec, G., and Lefrais, Y. *On the use of the infinite matrix assumption and associated concepts: A critical review*. Radiation Measurements, 47: 778–785, 2012.

Guérin, G., Jain, M., Thomsen, K. J., Murray, A. S., and Mercier, N. *Modelling dose rate to single grains of quartz in well-sorted sand samples: The dispersion arising from the presence of potassium feldspars and implications for single grain OSL dating*. Quaternary Geochronology, 27: 52–65, 2015.

Guérin, G., Christophe, C., Philippe, A., Murray, A. S., Thomsen, K. J., Tribolo, C., Urbanova, P., Jain, M., Guibert, P., Mercier, N., Kreutzer, S., and Lahaye, C. *Absorbed dose, equivalent dose, measured dose rates, and implications for OSL age estimates: Introducing the Average Dose Model*. Quaternary Geochronology, 41: 163–173, 2017.

Hesse, P. P., Williams, R., Ralph, T. J., Fryirs, K. A., Larkin, Z. T., Westaway, K. E., and Farebrother, W. *Palaeohydrology of lowland rivers in the Murray-Darling Basin, Australia*. Quaternary Science Reviews, 200: 85–105, 2018.

Huntley, D. J., Godfrey-Smith, D. I., and Thewalt, M. L. W. *Optical dating of sediments*. Nature, 313: 105–107, 1985.

Jacobs, Z. and Roberts, R. G. *Advances in optically stimulated luminescence dating of individual grains of quartz from archeological deposits*. Evolutionary Anthropology, 16: 210–223, 2007.

Jones, R. S., Small, D., Cahill, N., Bentley, M. J., and Whitehouse, P. L. *iceTEA: Tools for plotting and analysing cosmogenic-nuclide surface-exposure data from former ice margins*. Quaternary Geochronology, 51: 72–86, 2019.

Kreutzer, S., Schmidt, C., Fuchs, M. C., Dietze, M., Fischer, M., and Fuchs, M. *Introducing an R package for luminescence dating analysis*. Ancient TL, 30: 1–8, 2012.

Kreutzer, S., Burow, C., Dietze, M., Fuchs, M. C., Schmidt, C., Fischer, M., and Friedrich, J. *Luminescence: Comprehensive Luminescence Dating Data Analysis. R package version 0.8.6*, 2018. URL https://CRAN.R-project.org/package=Luminescence.

Kyker, G. C. and Liboff, A. R. *Absolute cosmic ray ionization measurements in a 900-liter chamber*. Journal of Geophysical Research: Space Physics, 83: 5539–5549, 1978.

Lancaster, N., Wolfe, S., Thomas, D., Bristow, C., Bubenzer, O., Burrough, S., Duller, G. A. T., Halfen, A., Hesse, P., Roskin, J., Singhvi, A., Tsoar, H., Tripaldi, A., Yang, X., and Zárate, M. *The INQUA Dunes Atlas chronologic database*. Quaternary International, 410: 3–10, 2016.

Lang, A., Hatté, C., Rousseau, D. D., Antoine, P., Fontugne, M., Zöller, L., and Hambach, U. *High-resolution chronologies for loess: comparing AMS 14C and optical dating results*. Quaternary Science Reviews, 22: 953–959, 2003.

Liritzis, I., Stamoulis, K., Papachristodoulou, C., and Ioannides, K. *A re-evaluation of radiation dose-rate conversion factors*. Mediterranean Archaeology and Archaeometry, 13: 1–15, 2013.

Logsdon, S. D. and Karlen, D. L. *Bulk density as a soil quality indicator during conversion to no-tillage*. Soil Tillage Research, 78: 143–149, 2004.

Ludwig, K. R. *ISOPLOT for MS-DOS, a Plotting and Regression Program for Radiogenic Isotope Data for IBM-PC Compatible Computers, Version 1.00. USGS Open-File Report OF-88-0557*, 1988.

Mejdahl, V. *Thermoluminescence dating: beta-dose attenuation in quartz grains*. Archaeometry, 21: 61–72, 1979.

Murray, A. S. and Wintle, A. G. *Luminescence dating of quartz using an improved single-aliquot regenerative-dose protocol*. Radiation Measurements, 32: 57–73, 2000.

Murray, A. S. and Wintle, A. G. *The single aliquot regenerative dose protocol: potential for improvements in reliability*. Radiation Measurements, 37: 377–381, 2003.

Neal, R. M. *Slice sampling*. Annals of Statistics, 31: 705–767, 2003.

Olley, J. M., Roberts, R. G., Yoshida, H., and Bowler, J. M. *Single-grain optical dating of grave-infill associated with human burials at Lake Mungo, Australia*. Quaternary Science Reviews, 25: 2469–2474, 2006.

Peng, J., Dong, Z., Han, F., Long, H., and Liu, X. *R package numOSL: numeric routines for optically stimulated luminescence dating*. Ancient TL, 31: 41–48, 2013.

Philippe, A., Guérin, G., and Kreutzer, S. *BayLum-An R package for Bayesian analysis of OSL ages: An introduction*. Quaternary Geochronology, 49: 16–24, 2019.

Plummer, M., Best, N., Cowles, K., and Vines, K. *CODA: convergence diagnosis and output analysis for MCMC*. R news, 6: 7–11, 2006.

Prescott, J. and Stephan, L. *The contribution of cosmic radiation to the environmental dose for thermoluminescence dating: latitude, altitude and depth dependences*. PACT, 6: 17–25, 1982.

Prescott, J. R. and Hutton, J. T. *Cosmic ray and gamma ray dosimetry for TL and ESR*. International Journal of Radiation Applications and Instrumentation. Part D. Nuclear Tracks and Radiation Measurements, 14: 223–227, 1988.

Prescott, J. R. and Hutton, J. T. *Cosmic ray contributions to dose rates for luminescence and ESR dating: Large depths and long-term time variations*. Radiation Measurements, 23: 497–500, 1994.

Preusser, F., Chithambo, M. L., Götte, T., Martini, M., Ramseyer, K., Sendezera, E. J., Susino, G. J., and Wintle, A. G. *Quartz as a natural luminescence dosimeter*. Earth-Science Reviews, 97: 184–214, 2009.

Ramsey, C. B. *Radiocarbon calibration and analysis of stratigraphy: the OxCal program*. Radiocarbon, 37: 425–430, 1995.

Ramsey, C. B. *Methods for Summarizing Radiocarbon Datasets*. Radiocarbon, 59: 1809–1833, 2017.

Rodnight, H. *How many equivalent dose values are needed to obtain a reproducible distribution*. Ancient TL, 26: 3–9, 2008.

Shao, Q., Bahain, J.-J., Dolo, J.-M., and Falguères, C. *Monte Carlo approach to calculate US-ESR age and age uncertainty for tooth enamel*. Quaternary Geochronology, 22: 99–106, 2014.

Silverman, B. W. *Density estimation for statistics and data analysis*. Routledge, 1998.

Sircombe, K. N. *AgeDisplay: an EXCEL workbook to evaluate and display univariate geochronological data using binned frequency histograms and probability density distributions*. Computers & Geosciences, 30: 21–31, 2004.

Stuiver, M., Reimer, P. J., and Reimer, R. W. *CALIB 7.1 [WWW program] at*, 2019. URL http://calib.org. accessed 2019-6-16.

Tabachnick, B. G. and Fidell, L. S. *Using Multivariate Statistics (3rd ed.)*. Harper and Row, New York, NY, USA, 1996.

Tamura, T., Cunningham, A. C., and Oliver, T. S. N. *Two-dimensional chronostratigraphic modelling of OSL ages from recent beach-ridge deposits, SE Australia*. Quaternary Geochronology, 49: 39–44, 2019.

Taylor, J. *An Introduction to error analysis: the study of uncertainties in physical measurements*. University Science Books, Sausalito, California, 1997.

Vermeesch, P. *CosmoCalc: An Excel add-in for cosmogenic nuclide calculations*. Geochemistry, Geophysics, Geosystems, 8: Q08003, 2007. doi: 10.1029/2006GC001530.

Vermeesch, P. *On the visualisation of detrital age distributions*. Chemical Geology, 312: 190–194, 2012.

Vermeesch, P. *Dissimilarity measures in detrital geochronology*. Earth-Science Reviews, 178: 310–321, 2018.

Wang, Y., Shao, M., Liu, Z., and Zhang, C. *Prediction of bulk density of soils in the Loess Plateau region of China*. Surveys in Geophysics, 35: 395–413, 2014.

Wintle, A. G. *Luminescence dating: where it has been and where it is going*. Boreas, 37: 471–482, 2008.

Wintle, A. G. and Adamiec, G. *Optically stimulated luminescence signals from quartz: A review*. Radiation Measurements, 98: 10–33, 2017.

Wintle, A. G. and Murray, A. S. *A review of quartz optically stimulated luminescence characteristics and their relevance in single-aliquot regeneration dating protocols*. Radiation Measurements, 41: 369–391, 2006.

Yang, X., Scuderi, L. A., Wang, X., Scuderi, L. J., Zhang, D., Li, H., Forman, S., Xu, Q., Wang, R., Huang, W., and Yang, S. *Groundwater sapping as the cause of irreversible desertification of Hunshandake Sandy Lands, Inner Mongolia, northern China.* Proceedings of the National Academy of Sciences of the United States of America, 112: 702–706, 2015.

Yang, X., Liang, P., Zhang, D., Li, H., Rioual, P., Wang, X., Xu, B., Ma, Z., Liu, Q., Ren, X., Hu, F., He, Y., Rao, G., and Chen, N. *Holocene aeolian stratigraphic sequences in the eastern portion of the desert belt (sand seas and sandy lands) in northern China and their palaeoenvironmental implications*. Science China Earth Sciences, 62: 1302–1315, 2019.

Reviewer

Geoff Duller

Reviewer comment:

This excellent paper is a welcome addition to the suite of software available for luminescence dating, and draws together a range of calculations that would otherwise be scattered across different programmes. The authors' parameterisation of the soft component of the cosmic dose rate (Eq. 24) is similar to that originally developed by Robert Clark in 1997 for his unpublished software "Cosmic". In that software he parameterised the data from Prescott & Hutton (1988) with the following function which was adopted for DRAC by Durcan et al. (2015).

$$D_c = 3.21 \times 10^{-2} x^4 - 1.35 \times 10^{-1} x^3 + 2.21 \times 10^{-1} x^2 - 2.07 \times 10^{-1} x + 0.295$$

Thesis Abstracts

Index

Victoria Fitzgerald

Chronology of gypsum dunes at Knolls, Utah: refining OSL techniques and timing of Holocene eolian processes

December 2019
Kansas State University, Manhattan, USA

Degree: M.Sc.
Supervisor: Dr. Joel Q. Spencer

This study examines eolian samples from post-Lake Bonneville gypsum dunes in Knolls, UT, primarily to determine suitability of optically stimulated luminescence (OSL) dating protocols for gypsum geochronology. Sedimentologists often rely on proxies to understand geologic timescales, OSL may eliminate that need in environments with gypsum. Using OSL we aimed to identify the ages of punctuated climatic events that are linked to deposition of the gypsum rich dunes found in the study area. To accomplish this pursuit, systematic research of gypsum preparation protocols were required. Multiple experiments were undertaken to assess the effectiveness of mineral isolation and etching. Knowledge of gypsum behavior is of particular interest, as it is found in both lacustrine and marine environments and is typically less soluble than other evaporites found in both settings, such as sodium chloride. Gypsum has also been observed at several hundred meters water depth in the alkaline environment of the Arctic Ocean. Additionally, gypsum sand grains are accessible to researchers in geomorphic features like unconsolidated to semi-consolidated dunes, making them easier to sample for OSL analyses than gypsum or quartz found in an outcrop. Sampling strategy can be quickly determined for dunes that are exposed on all sides.

The focus of this study seeks to resolve discrepancies observed in the small body of literature on gypsum as an OSL chronometer. Relatively homogenous eolian gypsum sand grain samples with grain sizes ranging from >63 μm to <250 μm from two adjacent paleodunes (KNP-A and KNP-B) and one coppice dune (CD-5) were used to determine best preparation practices and identify if punctuated climatic events during the Holocene could be detected using gypsum. The sample site was selected for a case study on OSL dating techniques because previous work has constrained the maximum age of post-Lake Bonneville dune formation (~ 12 ka BP).

Preparation protocols, independently checked using various methods, were selected with minimal mineralogical impact and OSL sensitivity considerations in mind. Bulk composition and mineralogy of the sediment at various steps in sample preparation have been analyzed using X-Ray Diffraction, bulk elemental extraction, particle size analysis, Scanning Electron Microscopy and binocular microscopy. Etching experiments indicate that an air-dried, dry-sieved, and gypsum-rich fraction ($90-125$ μm) can be effectively isolated and etched in ~ 36 wt% HCl for 40 minutes. Of the various OSL measurement protocols attempted, we confirmed a modified single-aliquot regenerative-dose protocol produces detectable luminescence signals and equivalent doses (D_e) that are usable in age calculations. Age results are likely to be underestimated by approximately $0.5-0.8$ ka, based on comparison to a single quartz OSL sample (KNP-A1) with an age of 2.2 ka and its equivalent gypsum sample of 1.4 ka. This is the oldest age sampled from the stratigraphically lowest section of either KNP-A or KNP-B. Samples from KNP-B identify this smaller dune was deposited after KNP-A began developing. Age results from the stratigraphically lowest sample collected, KNP-B1, indicate deposition occurred at 0.88 ka. The active coppice dune (CD-5) gypsum OSL age is 0.09 ka. This study recommends further investigation into why the apparent discrepancy between gypsum and quartz OSL chronology exists.

A PDF of this thesis can be downloaded from: http://hdl.handle.net/2097/40275

Amber G. E. Hood

New Insights into Old Problems: The application of a multidisciplinary approach to the study of early Egyptian ceramic chronology, with a focus on luminescence dating

January 2017
University of Oxford, Oxford, UK

Degree: Ph.D.
Supervisors: Jean-Luc Schwenninger, E. Christiana Köhler, Christopher Bronk Ramsey

This thesis takes a multidisciplinary approach to the study of ancient Egyptian ceramics by applying scientific dating techniques alongside more traditional methods. It is the first study to apply OSL dating to an Egyptian ceramic assemblage, and it has done so by developing the minimum extrac-

tion technique (MET), which has made it possible to use OSL to sample, and thus analyse, ceramics housed in museums.

The MET is at present essential to the success of OSL dating of Egyptian ceramics, as the exportation ban on antiquities has prevented OSL analysis of field material.

For this thesis, using this new sampling technique, OSL has been applied to several assemblages from the Predynastic to the Early Dynastic period. Ceramics from Bêt Khallaf have been examined, with three phases being established: late Naqada III, First Intermediate Period, and the mediaeval Islamic period. Absolute dates have been determined for each phase and, where comparison is possible, have been found in good agreement with the historical chronology.

A set of vessels from Naqada, Ballas, and the Tomb of Djer at Abydos have been examined using OSL in conjunction with radiocarbon dating. Again, three phases of activity were discerned: late Naqada II, early Naqada III, and the first scientifically determined dates for a burning event in the Tomb of Djer (the New Kingdom).

The thesis also demonstrates how OSL can be used as a relative dating technique by analysing a collection of Wavy-Handled ceramics and wine jars from Turah and Hierakonpolis, finding that the OSL results agree well with the established relative chronology.

Finally, this thesis has also examined the applicability of cladistic analysis to the study of Egyptian ceramics. Cladistics is a technique borrowed from the biological sciences which offers a complimentary way to examine the evolution of ceramic types and forms, in particular the development of beer and wine jars.

A PDF of this thesis can be downloaded from: https://ora.ox.ac.uk/objects/uuid:508818b7-930b-4e06-890c-5c2dbb12fe42

Yue Hu

Lithic industries and chronology of Middle Paleolithic sites in Southwest China

July 2019

University of Wollongong, Wollongong, NSW 2522, Australia

Degree: Ph.D.

Supervisors: Bo Li, Ben Marwick, Richard Fullagar, Sam Lin, Richard G. Roberts

The characteristics and development of Palaeolithic in China and more broadly in East Asia have been hotly debated. At the centre of the debate is whether there were lithic technological changes in East Asia during the Middle and Late Pleistocene. It has been argued that the lithic industries in this region were dominated by simple core-flake production system until the Late Pleistocene when Upper Palaeothic forms appeared. The lack of advanced stone tool technology in East Asia would imply that hominin populations in this region were possibly culturally and genetically isolated during the early and middle Pleistocene. One of the main reasons that caused such a debate is the scarce of well-defined 'Middle Paleolithic' sites in East Asia, because many of these sites were excavated decades ago and, hence, lacked reliable chronology and detailed and systematic lithic study. To contribute to our understanding of Paleolithic culture in East Asia during the late Middle Pleistocene period, this study presents detailed lithic analysis and chronological study on two Paleolithic sites in Southwest China, Guanyindong and Tianhuadong caves.

In order to establish reliable chronological frameworks for the sites, the recently developed single-grain optically stimulated luminescence (OSL) techniques were applied to date quartz grains extracted from the artefact-bearing sediments from the sites. Since a part proportion of the quartz grains have saturated OSL signal, the standardised growth curve (SGC) method was applied to avoid underestimation in age due to truncated equivalent dose distribution. It shows that the SGC method can be successfully applied to date sediments from this region. OSL ages of 170 – 80 and 90 – 50 thousands years ago were obtained for the Guanyindong and Tianhuadong sites, respectively, which suggests that both sites should be assigned to Middle Palaeolithic period.

Evidence of complex systems of lithic production from the two studied sites are reported. Based on detailed analysis of over 2000 stone artefacts from the Guanyindong assemblage, a total of 45 stone artefacts were identified to be made with Levallois concept, including 11 cores, 31 flakes and 4 tools. Apart from Levallois, the lithic assemblages from the sites provide evidence of diverse lithic production systems, including Quina, Kombewa, and discoid systems, which shows that the late Middle Pleistocene inhabitants in this region had used a variety of tool-making strategies to adapt to climatic and ecological conditions, raw material availability and demographic contexts. These new findings are similar and contemporary to those typically found in west Eurasia, suggesting that during late Middle Pleistocene hominins in this area had the comparable abilities as those in Europe and Africa, and, thus, challenge the longstanding view that there is a lack of distinct progress in lithic technology during the Early and Middle Palaeolithic period in East Asia.

Jack Arthur Johnson

Case Studies in Geoarchaeometry

December 2018

University of Washington, Seattle, USA

Degree: Ph.D.

Supervisor: James K. Feathers

This dissertation consists of four standalone papers. Each paper addresses a distinct geoarchaeological challenge through the application of specialized technical methods and experimental data. New approaches to data gathering are developed, and familiar approaches are combined with new archaeological applications and software tools to yield new

lines of evidence useful for the examination of significant archaeological questions. The first paper uses portable X-ray fluorescence (PXRF) to measure elemental concentrations in sediments and ceramics, but identifies several serious issues with common instrumentation and practice, then develops novel protocols and software tools to address these issues. The second paper describes a successful test application of PXRF to the relative dating of rock varnish accumulations atop petroglyphs at Hole-in-the-Ground in southeastern Oregon. The third paper details the use of luminescence dating and Bayesian depositional modeling to create a robust multi-proxy site formation history at Bear Creek in Redmond, Washington. The fourth paper uses luminescence dating of sediments and Bayesian modeling to document over 2000 years of changes in El Niño- and earthquake-driven depositional activity in the Santa and Chao Valleys of Perú, and discusses the implications of these patterns for archaeological research in the region.

A PDF of this thesis can be downloaded from: http://hdl.handle.net/1773/43285

Anna A. Romanyukha

Retrospective and Real-Time Semiconductor Dosimetry: Applications to Geological Dating and Brachytherapy Quality Assurance

June 2019
University of Wollongong, Wollongong, Australia
Degree: Ph.D.
Supervisors: Richard G. Roberts, Anatoly Rosenfeld

In this thesis solid state semiconductor dosimetry is applied to the improvement of luminescence dating techniques (part 1) and quality assurance in high dose rate (HDR) brachytherapy (BT) cancer treatments (part 2).

The aim of part 1 is the development, testing, and application of a novel method to measure spatially resolved dose rates in sediment samples using the Timepix pixelated detector. The Timepix contains an array of 256×256 pixels, each 55×55 μm in size and with its own preamplifier, discriminator and digital counter, and is able to provide the position and pixel-by-pixel count rate of the incident radiation. The development of a method to measure sediment samples and derive spatially resolved dose rates is described, followed by its application to sediment samples from Liang Bua and Denisova Cave archeological sites.

Part 2 focuses on the application of real time in vivo dosimetry for HDR BT treatment verification. MOSkin dosimeters were selected due to their small size and capability of measuring steep dose gradients, such as those characteristic of the HDR source. Three MOSkins were placed on a rectal probe to verify doses to the rectal wall in gynecological BT treatments. A feasibility study and the in vivo application of the proposed method to patient treatments at the Istituto Nazionale dei Tumori (INT) are described. Furthermore, a system for real time tracking of the HDR source is proposed by embedding epitaxial diodes on the surface of a multichannel vaginal cylinder (MVC). The ability of the developed system to verify positions and dwell times of the HDR source was tested using simple dwell positions and dwell times, followed by the retrospective delivery of 10 clinical plans previously delivered to patients undergoing adjuvant vaginal cuff BT after hysterectomy at INT.

A PDF of this thesis can be downloaded from: https://ro.uow.edu.au/theses1/561/

Bibliography

Compiled by Sebastien Huot

From 16th May 2019 to 30th November 2019

Various geological applications

- aeolian

Buckland, C.E., Thomas, D.S.G., Bailey, R.M., 2019. Complex disturbance-driven reactivation of near-surface sediments in the largest dunefield in North America during the last 200 years. Earth Surface Processes and Landforms 44, 2794-2809. http://doi.org/10.1002/esp.4708

Carr, A.S., Hay, A.S., Powell, D.M., Livingstone, I., 2019. Testing post-IR IRSL luminescence dating methods in the southwest Mojave Desert, California, USA. Quaternary Geochronology 49, 85-91. http://doi.org/10.1016/j.quageo.2018.05.006

Chen, D., Pan, B., Hu, X., Wang, Y., Pan, X., Wang, W., Zhang, J., Pang, H., 2019. Formation age of Jiudong Sandy Land, in the western Hexi Corridor, NW China. Quaternary International 513, 47-55. http://doi.org/10.1016/j.quaint.2019.02.026

ChongYi, E., Jing, Z., ZongYan, C., YongJuan, S., YaJuan, Z., Ping, L., ManPing, S., YunKun, S., 2019. High resolution OSL dating of aeolian activity at Qinghai Lake, Northeast Tibetan Plateau. CATENA 183, 104180. http://doi.org/10.1016/j.catena.2019.104180

Ellerton, D., Rittenour, T., Miot da Silva, G., Gontz, A., Shulmeister, J., Hesp, P., Santini, T.C., Welsh, K.J., 2018. Late-Holocene cliff-top blowout activation and evolution in the Cooloola Sand Mass, south-east Queensland, Australia. The Holocene 28, 1697-1711. http://doi.org/10.1177/0959683618788679

Fitzsimmons, K.E., Spry, C., Stern, N., 2019. Holocene and recent aeolian reactivation of the Willandra Lakes lunettes, semi-arid southeastern Australia. The Holocene 29, 606-621. http://doi.org/10.1177/0959683618824790

Fuchs, M., Lomax, J., 2019. Stone pavements in arid environments: Reasons for De overdispersion and grain-size dependent OSL ages. Quaternary Geochronology 49, 191-198. http://doi.org/10.1016/j.quageo.2018.05.013

Kalińska, E., 2019. Understanding a continuous inland aeolian deposition: a closer look into a chronological and sedimentary record of the north-eastern European Sand Belt. Bulletin of Geography. Physical Geography Series 16, 31-43. http://doi.org/10.2478/bgeo-2019-0003

Kalińska, E., Hang, T., Jõeleht, A., Olo, S., Nartišs, M., Adamiec, G., 2019. Macro- and micro-scale study and chronology of Late Weichselian aeolian sediments in Estonia, north-eastern European Sand Belt. International Journal of Earth Sciences 108, 2021-2035. http://doi.org/10.1007/s00531-019-01746-2

Kruczkowska, B., Błaszkiewicz, M., Jonczak, J., Uzarowicz, Ł., Moska, P., Brauer, A., Bonk, A., Słowiński, M., 2020. The Late Glacial pedogenesis interrupted by aeolian activity in Central Poland – records from the Lake Gościąż catchment. CATENA 185, 104286. http://doi.org/10.1016/j.catena.2019.104286

Luo, W., Wang, Z., Lu, J., Yang, L., Qian, G., Dong, Z., Bateman, M.D., 2019. Mega-blowouts in Qinghai–Tibet Plateau: Morphology, distribution and initiation. Earth Surface Processes and Landforms 44, 449-458. http://doi.org/10.1002/esp.4507

Luo, W., Wang, Z., Lu, J., Yang, L., Qian, G., Dong, Z., Bateman, M.D., 2019. Mega-blowouts in Qinghai–Tibet Plateau: Morphology, distribution and initiation. Earth Surface Processes and Landforms 44, 449-458. http://doi.org/10.1002/esp.4507

Messineo, P.G., Tonello, M.S., Stutz, S., Tripaldi, A., Scheifler, N., Pal, N., Sánchez Vuichard, G., Navarro, D., 2019. Human occupation strategies and related environmental-climate during the middle and late Holocene in central Pampas of Argentina. The Holocene 29, 244-261. http://doi.org/10.1177/0959683618810407

Neudorf, C.M., Lian, O.B., McIntosh, P.D., Gingerich, T.B., Augustinus, P.C., 2019. Investigation into the OSL and TT-OSL signal characteristics of ancient (>100 ka) Tasmanian aeolian quartz and its utility as a geochronometer for understanding long-term climate-driven landscape change. Quaternary Geochronology 53, 101005. http://doi.org/10.1016/j.quageo.2019.101005

Rahimzadeh, N., Khormali, F., Gribenski, N., Tsukamoto, S., Kehl, M., Pint, A., Kiani, F., Frechen, M., 2019. Timing and development of sand dunes in the Golestan Province, northern Iran—Implications for the Late-Pleistocene history of the Caspian Sea. Aeolian Research 41, 100538. http://doi.org/10.1016/j.aeolia.2019.07.004

Ritter, B., Wennrich, V., Medialdea, A., Brill, D., King, G., Schneiderwind, S., Niemann, K., Fernández-Galego, E., Diederich, J., Rolf, C., Bao, R., Melles, M., Dunai, T.J., 2019. "Climatic fluctuations in the hyperarid core of the Atacama Desert during the past 215 ka". Scientific Reports 9, 5270. http://doi.org/10.1038/s41598-019-41743-8

Srivastava, A., Durcan, J.A., Thomas, D.S.G., 2019. Analysis of late Quaternary linear dune development in the Thar Desert, India. Geomorphology 344, 90-98. http://doi.org/10.1016/j.geomorph.2019.07.013

Srivastava, A., Thomas, D.S.G., Durcan, J.A., 2019. Holocene dune activity in the thar desert, India. Earth Surface Processes and Landforms 44, 1407-1418. http://doi.org/10.1002/esp.4583

Wacha, L., Montanari, A., Lomax, J., Fiebig, M., Lüthgens, C., Korbar, T., Koeberl, C., 2019. Last Glacial Maximum giant sand dunes on the island of Vis, Croatia, 542. in: Koeberl, C., Bice, D.M. (Eds.), 250 million years of earth history in central Italy: Celebrating 25 years of the geological observatory of Coldigioco. Geological Society of America, pp. 459-470. http://doi.org/10.1130/2019.2542(26)

Yang, L., Long, H., Cheng, H., He, Z., Hu, G., 2019. OSL dating of a mega-dune in the eastern Lake Qinghai basin (northeastern Tibetan Plateau) and its implications for Holocene aeolian activities. Quaternary Geochronology 49, 165-171. http://doi.org/10.1016/j.quageo.2018.02.005

Yang, X., Liang, P., Zhang, D., Li, H., Rioual, P., Wang, X., Xu, B., Ma, Z., Liu, Q., Ren, X., Hu, F., He, Y., Rao, G., Chen, N., 2019. Holocene aeolian stratigraphic sequences in the eastern portion of the desert belt (sand seas and sandy lands) in northern China and their palaeoenvironmental implications. Science China Earth Sciences 62, 1302-1315. http://doi.org/10.1007/s11430-018-9304-y

Zhang, Y., Huang, C.C., Tan, Z., Qiu, H., Chen, Y., Cuan, Y., Zhao, H., Tan, Z., Zou, M., Wang, J., Zhang, Y., 2019. Palaeoclimatic and palaeoenvironmental implications of late-Pleistocene aeolian sand in the Jin-Shaan Gorges of the Yellow River valley revealed by luminescence chronology. The Holocene 29, 964-974. http://doi.org/10.1177/0959683619831421

- cave

Arriolabengoa, M., Iriarte, E., Aranburu, A., Yusta, I., Arnold, L.J., Demuro, M., Arrizabalaga, A., 2018. Reconstructing the sedimentary history of Lezetxiki II cave (Basque Country, northern Iberian Peninsula) using micromorphological analysis. Sedimentary Geology 372, 96-111. http://doi.org/10.1016/j.sedgeo.2018.05.006

Deák, J., Preusser, F., Cattin, M.I., Castel, J.C., Chauvière, F.X., 2019. New data from the Middle Palaeolithic Cotencher cave (Swiss Jura): site formation, environment, and chronology. Quaternary Science Journal (Eiszeitalter & Gegenwart) 67, 41-72. http://doi.org/10.5194/egqsj-67-41-2019

Montanari, A., Lüthgens, C., Lomax, J., Mainiero, M., Mariani, S., Fiebig, M., 2019. Luminescence geochronology of Pleistocene slack-water deposits in the Frasassi hypogenic cave system, Italy, 542. in: Koeberl, C., Bice, D.M. (Eds.), 250 Million Years of Earth History in Central Italy: Celebrating 25 Years of the Geological Observatory of Coldigioco. Geological Society of America, pp. 411-428. http://doi.org/10.1130/2019.2542(23)

- coastal

Carvalho, R.C., Oliver, T.S.N., Woodroffe, C.D., 2019. Transition from marine to fluvial-dominated sediment supply at Shoalhaven prograded barrier, southeastern Australia. Geomorphology 341, 65-78. http://doi.org/10.1016/j.geomorph.2019.05.010

Erginal, A.E., Polymeris, G.S., Karataş, A., Giannoulatou, V., Şahiner, E., Meriç, N., Erenoğlu, O., Selim, H.H., Karabıyıkoğlu, M., 2019. Raised braided stream gravels on Mount Keldağ, Hatay (Eastern Mediterranean coast, Turkey): implications of transformation to beachrock and ensuing tectonic uplift. Mediterranean Geoscience Reviews 1, 45-53. http://doi.org/10.1007/s42990-019-00006-4

García, J.-L., Andrade, B., Calderón, M., Lüthgens, C., 2019. Multi-millennial scale climate variability during MIS 3 and MIS 2 inferred from luminescence dating of coastal sand dunes and buried paleosol sequences in central Chile, 32°S. Journal of Quaternary Science 34, 203-214. http://doi.org/10.1002/jqs.3092

Ge, W., Li, C., Xing, H., Li, L., Li, Y.-X., Rittenour, T., Hu, Z., 2019. Examining the chronology of transgressions since the late Pleistocene in the Fujian coast, southeastern China. Quaternary International 527, 34-43. http://doi.org/10.1016/j.quaint.2018.11.034

Hein, C.J., Shawler, J.L., De Camargo, J.M., Klein, A.H.D.F., Tenebruso, C., Fenster, M.S., 2019. The role of coastal sediment sinks in modifying longshore sand fluxes: Examples from the coasts of southern Brazil and the mid-atlantic USA, Coastal Sediments. WORLD SCIENTIFIC, pp. 2330-2344. http://doi.org/10.1142/9789811204487_0199

Jin, J., Huang, Y., Li, Z., Fan, X., Ling, Z., Li, Z., Liu, X., 2019. Optically stimulated luminescence dating of coastal sediments at Funing Bay, Southeastern China. Geochronometria 46, 15-24. http://doi.org/10.1515/geochr-2015-0103

Korsakova, O., Molodkov, A., Yelovicheva, Y., Kolka, V., 2019. Middle Pleistocene marine deposits on the Kola Peninsula (NW Russia). Quaternary International 509, 3-16. http://doi.org/10.1016/j.quaint.2018.09.019

Muñiz, F., Cáceres, L.M., Rodríguez-Vidal, J., Neto de Carvalho, C., Belo, J., Finlayson, C., Finlayson, G., Finlayson, S., Izquierdo, T., Abad, M., Jiménez-Espejo, F.J., Sugisaki, S., Gómez, P., Ruiz, F., 2019. Following the last Neanderthals: Mammal tracks in Late Pleistocene coastal dunes of Gibraltar (S Iberian Peninsula). Quaternary Science Reviews 217, 297-309. http://doi.org/10.1016/j.quascirev.2019.01.013

Mushkin, A., Katz, O., Porat, N., 2019. Overestimation of short-term coastal cliff retreat rates in the eastern Mediterranean resolved with a sediment budget approach. Earth Surface Processes and Landforms 44, 179-190. http://doi.org/10.1002/esp.4490

Nian, X., Zhang, W., Qiu, F., Qin, J., Wang, Z., Sun, Q., Chen, J., Chen, Z., Liu, N., 2019. Luminescence characteristics of quartz from Holocene delta deposits of the Yangtze River and their provenance implications. Quaternary Geochronology 49, 131-137. http://doi.org/10.1016/j.quageo.2018.04.010

Normand, R., Simpson, G., Herman, F., Biswas, R.H., Bahroudi, A., Schneider, B., 2019. Dating and morpho-stratigraphy of uplifted marine terraces in the Makran subduction zone (Iran). Earth Surf. Dynam. 7, 321-344. http://doi.org/10.5194/esurf-7-321-2019

Oliver, T.S.N., Tamura, T., Short, A.D., Woodroffe, C.D., 2019. Rapid shoreline progradation followed by vertical foredune building at Pedro Beach, southeastern Australia. Earth Surface Processes and Landforms 44, 655-666. http://doi.org/10.1002/esp.4510

Ott, R.F., Gallen, S.F., Wegmann, K.W., Biswas, R.H., Herman, F., Willett, S.D., 2019. Pleistocene terrace formation, Quaternary rock uplift rates and geodynamics of the Hellenic Subduction Zone revealed from dating of paleoshorelines on Crete, Greece. Earth and Planetary Science Letters 525, 115757. http://doi.org/10.1016/j.epsl.2019.115757

Sherwood, J.E., Bowler, J.M., Carey, S.P., Hellstrom, J., McNiven, I.J., Murray-Wallace, C.V., Prescott, J.R., Questiaux, D.G., Spooner, N.A., Williams, F.M., Woodhead, J.D., 2019. The Moyjil site, south-west Victoria, Australia: chronology. Proceedings of the Royal Society of Victoria 130, 32-49. http://doi.org/10.1071/RS18005

Surakiatchai, P., Songsangworn, E., Pailoplee, S., Choowong, M., Phantuwongraj, S., Chabangborn, A., Charusiri, P., 2019. Optically stimulated luminescence dating reveals rate of beach ridge and sand spit depositions from the upper Gulf of Thailand. Songklanakarin Journal of Science and Technology 41, 1136-1145. https://rdo.psu.ac.th/sjstweb/journal/41-5/23.pdf

Tamura, T., Cunningham, A.C., Oliver, T.S.N., 2019. Two-dimensional chronostratigraphic modelling of OSL ages from recent beach-ridge deposits, SE Australia. Quaternary Geochronology 49, 39-44. http://doi.org/10.1016/j.quageo.2018.03.003

Tamura, T., Oliver, T.S.N., Cunningham, A.C., Woodroffe, C.D., 2019. Recurrence of extreme coastal erosion in SE Australia beyond historical timescales inferred from beach ridge morphostratigraphy. Geophysical Research Letters 46, 4705-4714. http://doi.org/10.1029/2019gl083061

van den Biggelaar, D.F.A.M., Wallinga, J., van Balen, R.T., Kasse, C., Troelstra, S., Kluiving, S.J., 2019. High-resolution optical dating of Late Holocene storm surge deposits – a showcase from Schokland (Noordoostpolder, the Netherlands). Earth Surface Processes and Landforms 44, 886-899. http://doi.org/10.1002/esp.4542

- colluvial

Kanari, M., Katz, O., Weinberger, R., Porat, N., Marco, S., 2019. Evaluating earthquake-induced rockfall hazard near the Dead Sea Transform. Natural Hazards And Earth System Sciences 19, 889-906. http://doi.org/10.5194/nhess-19-889-2019

Kołodyńska-Gawrysiak, R., 2019. Holocene evolution of closed depressions and its relation to landscape dynamics in the loess areas of Poland. The Holocene 29, 543-564. http://doi.org/10.1177/0959683618824792

van der Meij, W.M., Reimann, T., Vornehm, V.K., Temme, A.J.A.M., Wallinga, J., van Beek, R., Sommer, M., 2019. Reconstructing rates and patterns of colluvial soil redistribution in agrarian (hummocky) landscapes. Earth Surface Processes and Landforms 44, 2408-2422. http://doi.org/10.1002/esp.4671

- earthquake (and fault related)

Arora, S., Malik, J.N., Sahoo, S., 2019. Paleoseismic evidence of a major earthquake event(s) along the hinterland faults: Pinjore Garden Fault (PGF) and Jhajra Fault (JF) in northwest Himalaya, India. Tectonophysics 757, 108-122. http://doi.org/10.1016/j.tecto.2019.01.001

del Río, I., Sawakuchi, A.O., González, G., 2019. Luminescence dating of sediments from central Atacama Desert, northern Chile. Quaternary Geochronology 53, 101002. http://doi.org/10.1016/j.quageo.2019.05.001

Gold, R.D., DuRoss, C.B., Delano, J.E., Jibson, R.W., Briggs, R.W., Mahan, S.A., Williams, R.A., Corbett, D.R., 2019. Four Major Holocene Earthquakes on the Reelfoot Fault Recorded by Sackungen in the New Madrid Seismic Zone, USA. Journal of Geophysical Research: Solid Earth 124, 3105-3126. http://doi.org/10.1029/2018jb016806

Kim, J.H., Ree, J.-H., Choi, J.-H., Chauhan, N., Hirose, T., Kitamura, M., 2019. Experimental investigations on dating the last earthquake event using OSL signals of quartz from fault gouges. Tectonophysics 769, 228191. http://doi.org/10.1016/j.tecto.2019.228191

Li, X., Feng, X., Li, X., Li, C., Zheng, W., Zhang, P., Pierce, I.K.D., Li, G., Li, C., Liu, Y., Ren, G., Luo, Q., 2019. Geological and geomorphological evidence for active faulting of the southern Liupanshan fault zone, NE Tibetan Plateau. Geomorphology 345, 106849. http://doi.org/10.1016/j.geomorph.2019.106849

Li, X., Zhang, P., Zheng, W., Feng, X., Li, C., Pierce, I.K.D., Xu, H., Li, X., Ai, M., Chen, G., Dong, J., Liu, J., Ren, G., 2018. Kinematics of late Quaternary slip along the Qishan-Mazhao fault: Implications for tectonic deformation on the southwestern Ordos, China. Tectonics 37, 2983-3000. http://doi.org/10.1029/2018tc005043

Little, T.A., Van Dissen, R., Kearse, J., Norton, K., Benson, A., Wang, N., 2018. Kekerengu Fault, New Zealand: Timing and size of Late Holocene surface ruptures. Bulletin of the Seismological Society of America 108, 1556-1572. http://doi.org/10.1785/0120170152

Pucci, S., Villani, F., Civico, R., Di Naccio, D., Porreca, M., Benedetti, L., Gueli, A., Stella, G., Baccheschi, P., Pantosti, D., 2019. Complexity of the 2009 L'Aquila earthquake causative fault system (Abruzzi Apennines, Italy) and effects on the Middle Aterno Quaternary basin arrangement. Quaternary Science Reviews 213, 30-66. http://doi.org/10.1016/j.quascirev.2019.04.014

Ren, J., Xu, X., Zhang, S., Ding, R., Liu, H., Liang, O., Zhao, J., 2019. Late Quaternary slip rates and Holocene paleoearthquakes of the eastern Yumu Shan fault, northeast Tibet: Implications for kinematic mechanism and seismic hazard. Journal of Asian Earth Sciences 176, 42-56. http://doi.org/10.1016/j.jseaes.2019.02.006

Shao, Y., Yuan, D., Oskin, M.E., Wang, P., Liu-Zeng, J., Li, C., Wu, Z., 2017. Historical (Yuan Dynasty) earthquake on the north Danghe Nanshan thrust, western Qilian Shan, China. Bulletin of the Seismological Society of America 107, 1175-1184. http://doi.org/10.1785/0120160289

Van Balen, R.T., Bakker, M.A.J., Kasse, C., Wallinga, J., Woolderink, H.A.G., 2019. A Late Glacial surface rupturing earthquake at the Peel Boundary fault zone, Roer Valley Rift System, the Netherlands. Quaternary Science Reviews 218, 254-266. http://doi.org/10.1016/j.quascirev.2019.06.033

Yang, H.L., Chen, J., Yao, L., Liu, C.R., Shimamoto, T., Thompson Jobe, J.A., 2019. Resetting of OSL/TL/ESR signals by frictional heating in experimentally sheared quartz gouge at seismic slip rates. Quaternary Geochronology 49, 52-56. http://doi.org/10.1016/j.quageo.2018.05.005

Zhang, Y.-P., Zheng, W.-J., Zhang, D.-L., Zhang, P.-Z., Yuan, D.-Y., Tian, Q.-Y., Zhang, B.-X., Liang, S.-M., 2019. Late Pleistocene left-lateral slip rates of the Gulang Fault and its tectonic implications in eastern Qilian Shan (NE Tibetan Plateau), China. Tectonophysics 756, 97-111. http://doi.org/10.1016/j.tecto.2019.02.013

Zinke, R., Dolan, J.F., Rhodes, E.J., Van Dissen, R., McGuire, C.P., Hatem, A.E., Brown, N.D., Langridge, R.M., 2019. Multimillennial Incremental Slip Rate Variability of the Clarence Fault at the Tophouse Road Site, Marlborough Fault System, New Zealand. Geophysical Research Letters 46, 717-725. http://doi.org/10.1029/2018gl080688

- fluvial

Alderson, D.M., Evans, M.G., Rothwell, J.J., Rhodes, E.J., Boult, S., 2019. Geomorphological controls on fluvial carbon storage in headwater peatlands. Earth Surface Processes and Landforms 44, 1675-1693. http://doi.org/10.1002/esp.4602

Aslan, A., Karlstrom, K.E., Kirby, E., Heizler, M.T., Granger, D.E., Feathers, J.K., Hanson, P.R., Mahan, S.A., 2019. Resolving time-space histories of Late Cenozoic bedrock incision along the Upper Colorado River, USA. Geomorphology 347, 106855. http://doi.org/10.1016/j.geomorph.2019.106855

Bender, A.M., Lease, R.O., Haeussler, P.J., Rittenour, T., Corbett, L.B., Bierman, P.R., Caffee, M.W., 2019. Pace and process of active folding and fluvial incision across the Kantishna Hills anticline, Central Alaska. Geophysical Research Letters 46, 3235-3244. http://doi.org/10.1029/2018gl081509

Carling, P.A., Leclair, S.F., 2019. Alluvial stratification styles in a large, flash-flood influenced dryland river: The Luni River, Thar Desert, north-west India. Sedimentology 66, 102-128. http://doi.org/10.1111/sed.12487

Chamberlain, E.L., Wallinga, J., 2019. Seeking enlightenment of fluvial sediment pathways by optically stimulated luminescence signal bleaching of river sediments and deltaic deposits. Earth Surface Dynamics 7, 723-736. http://doi.org/10.5194/esurf-7-723-2019

Dave, A.K., Courty, M.-A., Fitzsimmons, K.E., Singhvi, A.K., 2019. Revisiting the contemporaneity of a mighty river and the Harappans: Archaeological, stratigraphic and chronometric constraints. Quaternary Geochronology 49, 230-235. http://doi.org/10.1016/j.quageo.2018.05.002

del Val, M., Duval, M., Medialdea, A., Bateman, M.D., Moreno, D., Arriolabengoa, M., Aranburu, A., Iriarte, E., 2019. First chronostratigraphic framework of fluvial terrace systems in the eastern Cantabrian margin (Bay of Biscay, Spain). Quaternary Geochronology 49, 108-114. http://doi.org/10.1016/j.quageo.2018.07.001

Dutta, S., Mujtaba, S.A.I., Bhavani, R., Raza, M.A., Chunchekar, R., Sadiq, M., 2020. Responses of Indian Summer Monsoon Dynamics and Late Quaternary Fluvial Development: Records from Yamuna River Valley, NW-Himalaya, in: Goel, P.S., Ravindra, R., Chattopadhyay, S. (Eds.), Climate Change and the White World. Springer International Publishing, Cham, pp. 187-218. http://doi.org/10.1007/978-3-030-21679-5_13

Erturaç, M.K., Şahiner, E., Zabcı, C., Okur, H., Polymeris, G.S., Meriç, N., İkiel, C., 2019. Fluvial response to rising levels of the Black Sea and to climate changes during the Holocene: Luminescence geochronology of the Sakarya terraces. The Holocene 29, 941-952. http://doi.org/10.1177/0959683619831428

Fu, X., Cohen, T.J., Fryirs, K., 2019. Single-grain OSL dating of fluvial terraces in the upper Hunter catchment, southeastern Australia. Quaternary Geochronology 49, 115-122. http://doi.org/10.1016/j.quageo.2018.06.002

Gao, H., Li, Z., Liu, F., Wu, Y., Li, P., Zhao, X., Li, F., Guo, J., Liu, C., Pan, B., Jia, H., 2020. Terrace formation and river valley development along the lower Taohe River in central China. Geomorphology 348, 106885. http://doi.org/10.1016/j.geomorph.2019.106885

Gao, L., Long, H., Zhang, P., Tamura, T., Feng, W., Mei, Q., 2019. The sedimentary evolution of Yangtze River delta since MIS3: A new chronology evidence revealed by OSL dating. Quaternary Geochronology 49, 153-158. http://doi.org/10.1016/j.quageo.2018.03.010

Garon, H., Voinchet, P., Bahain, J.J., Despriée, J., Courcimault, G., Tissoux, H., Falguères, C., 2017. Datation ESR de quartz fluviatiles : nouvelles données chronologiques pour le secteur « intermédiaire » de la vallée de la Creuse (Indre, région Centre, France). Quaternaire 28, 73-85. http://doi.org/10.4000/quaternaire.7838

Graves, B.P., Ralph, T.J., Hesse, P.P., Westaway, K.E., Kobayashi, T., Gadd, P.S., Mazumder, D., 2019. Macro-charcoal accumulation in floodplain wetlands: Problems and prospects for reconstruction of fire regimes and environmental conditions. PLOS ONE 14, e0224011. http://doi.org/10.1371/journal.pone.0224011

Gutiérrez, F., Sevil, J., Silva, P.G., Roca, E., Escosa, F., 2019. Geomorphic and stratigraphic evidence of Quaternary diapiric activity enhanced by fluvial incision. Navarrés salt wall and graben system, SE Spain. Geomorphology 342, 176-195. http://doi.org/10.1016/j.geomorph.2019.06.002

He, Z., Long, H., Yang, L., Zhou, J., 2019. Luminescence dating of a fluvial sequence using different grain size fractions and implications on Holocene flooding activities in Weihe Basin, central China. Quaternary Geochronology 49, 123-130. http://doi.org/10.1016/j.quageo.2018.05.007

Huang, M., Zhu, C., Ma, C., Yang, Z., Liu, Y., Jia, T., 2020. The Hongqiaocun Site: The earliest evidence of ancient flood sedimentation of the water conservancy facilities in the Chengdu Plain, China. CATENA 185, 104296. http://doi.org/10.1016/j.catena.2019.104296

Larsen, A., May, J.-H., Carah, X., 2019. Late Quaternary biotic and abiotic controls on long-term sediment flux in a northern Australian tropical river system. Earth Surface Processes and Landforms 44, 2494-2509. http://doi.org/10.1002/esp.4652

Lauer, T., Frechen, M., Fischer, P., 2017. Luminescence dating of the Lower Middle Terrace site at Brühl, southern Lower Rhine Embayment – a first dating approach. Zeitschrift der Deutschen Gesellschaft für Geowissenschaften 168, 105-114. http://doi.org/10.1127/zdgg/2017/0109

Lichtenberger, A., Raja, R., Seland, E.H., Kinnaird, T., Simpson, I.A., 2019. Urban-Riverine Hinterland Synergies in Semi-Arid Environments: Millennial-Scale Change, Adaptations, and Environmental Responses at Gerasa/Jerash. Journal of Field Archaeology 44, 333-351. http://doi.org/10.1080/00934690.2019.1625619

Lu, H., Cheng, L., Wang, Z., Zhang, T., Lü, Y., Zhao, J., Li, Y., Zheng, X., 2018. Latest Quaternary rapid river incision across an inactive fold in the northern Chinese Tian Shan foreland. Quaternary Science Reviews 179, 167-181. http://doi.org/10.1016/j.quascirev.2017.10.017

Lüthgens, C., Neuhuber, S., Grupe, S., Payer, T., Peresson, M., Fiebig, M., 2017. Geochronological investigations using a combination of luminescence and cosmogenic nuclide burial dating of drill cores from the Vienna Basin. Zeitschrift der Deutschen Gesellschaft für Geowissenschaften 168, 115-140. http://doi.org/10.1127/zdgg/2017/0081

Mahadev, Singh, A.K., Jaiswal, M.K., 2019. Application of luminescence age models to heterogeneously bleached quartz grains from flood deposits in Tamilnadu, southern India: Reconstruction of past flooding. Quaternary International 513, 95-106. http://doi.org/10.1016/j.quaint.2019.02.037

Murton, J.B., Bateman, M.D., Telka, A.M., Waller, R., Whiteman, C., Kuzmina, S., 2017. Early to mid Wisconsin fluvial deposits and palaeoenvironment of the Kidluit Formation, Tuktoyaktuk Coastlands, western Arctic Canada. Permafrost and Periglacial Processes 28, 523-533. http://doi.org/10.1002/ppp.1946

Ramírez-Herrera, M.T., Gaidzik, K., Forman, S., Kostoglodov, V., Bürgmann, R., Johnson, C.W., 2018. Relating the long-term and short-term vertical deformation across a transect of the forearc in the central Mexican subduction zone. Geosphere 14, 419-439. http://doi.org/10.1130/ges01446.1

Resmi, M.R., Achyuthan, H., 2018. Northeast monsoon variations during the Holocene inferred from palaeochannels and active channels of the Palar River basin, Southern Peninsular India. The Holocene 28, 895-913. http://doi.org/10.1177/0959683617752839

Storozum, M.J., Mo, D., Wang, H., Ren, X., Zhang, Y., Kidder, T.R., 2017. Anthropogenic origins of a late Holocene, basin-wide unconformity in the middle reaches of the Yellow River, the Luoyang Basin, Henan Province, China. Quaternary Research 87, 423-441. http://doi.org/10.1017/qua.2017.10

Townsend, K.F., Nelson, M.S., Rittenour, T.M., Pederson, J.L., 2019. Anatomy and evolution of a dynamic arroyo system, Kanab Creek, southern Utah, USA. GSA Bulletin 131, 2094-2109. http://doi.org/10.1130/B35195.1

Vayssière, A., Rué, M., Recq, C., Gardère, P., Thamó-Bozsó, E., Castanet, C., Virmoux, C., Gautier, E., 2019. Lateglacial changes in river morphologies of northwestern Europe: An example of a smooth response to climate forcing (Cher River, France). Geomorphology 342, 20-36. http://doi.org/10.1016/j.geomorph.2019.05.019

Viveen, W., Zevallos-Valdivia, L., Sanjurjo-Sanchez, J., 2019. The influence of centennial-scale variations in the South American summer monsoon and base-level fall on Holocene fluvial systems in the Peruvian Andes. Global and Planetary Change 176, 1-22. http://doi.org/10.1016/j.gloplacha.2019.03.001

Voinchet, P., Yin, G., Falguères, C., Liu, C., Han, F., Sun, X., Bahain, J.-J., 2019. Dating of the stepped quaternary fluvial terrace system of the Yellow River by electron spin resonance (ESR). Quaternary Geochronology 49, 278-282. http://doi.org/10.1016/j.quageo.2018.08.001

Wang, F., Nian, X., Wang, J., Zhang, W., Peng, G., Ge, C., Dong, C., Qu, J., Li, D., 2018. Multiple dating approaches applied to the recent sediments in the Yangtze River (Changjiang) subaqueous delta. The Holocene 28, 858-866. http://doi.org/10.1177/0959683617752847

Xiang, F., Huang, H., Ogg, J.G., Zhu, H., Kang, D., 2020. Quaternary sediment characteristics and paleoclimate implications of deposits in the Three Gorges and Yichang areas of the Yangtze River. Geomorphology 351, 106981. http://doi.org/10.1016/j.geomorph.2019.106981

Yang, H., Yang, X., Huang, W., Li, A., Hu, Z., Huang, X., Yang, H., 2020. 10Be and OSL dating of Pleistocene fluvial terraces along the Hongshuiba River: Constraints on tectonic and climatic drivers for fluvial downcutting across the NE Tibetan Plateau margin, China. Geomorphology 348, 106884. http://doi.org/10.1016/j.geomorph.2019.106884

Zhao, H., Liu, Z., Song, L., Wang, C., Li, S.-H., 2019. OSL dating of flood sediments in the North China Plain. Quaternary Geochronology 49, 101-107. http://doi.org/10.1016/j.quageo.2018.07.010

- glacial and periglacial

Fisher, T.G., Horton, J., Lepper, K., Loope, H., 2018. Aeolian activity during Late Glacial time, with an example from Mongo, Indiana, USA. Canadian Journal of Earth Sciences 56, 175-182. http://doi.org/10.1139/cjes-2018-0127

Gaar, D., Graf, H.R., Preusser, F., 2019. New chronological constraints on the timing of Late Pleistocene glacier advances in northern Switzerland. Quaternary Science Journal (Eiszeitalter & Gegenwart) 68, 53-73. http://doi.org/10.5194/egqsj-68-53-2019

Levy, J.S., Rittenour, T.M., Fountain, A.G., O'Connor, J.E., 2017. Luminescence dating of paleolake deltas and glacial deposits in Garwood Valley, Antarctica: Implications for climate, Ross ice sheet dynamics, and paleolake duration. Geological Society of America Bulletin 129, 1071-1084. http://doi.org/10.1130/B31539.1

Mendelová, M., Hein, A.S., Rodés, Á., Smedley, R.K., Xu, S., 2020. Glacier expansion in central Patagonia during the Antarctic Cold Reversal followed by retreat and stabilisation during the Younger Dryas. Quaternary Science Reviews 227, 106047. http://doi.org/10.1016/j.quascirev.2019.106047

Möller, P., Benediktsson, Í.Ö., Anjar, J., Bennike, O., Bernhardson, M., Funder, S., Håkansson, L.M., Lemdahl, G., Licciardi, J.M., Murray, A.S., Seidenkrantz, M.-S., 2019. Data set on sedimentology, palaeoecology and chronology of Middle to Late Pleistocene deposits on the Taimyr Peninsula, Arctic Russia. Data in Brief 25, 104267. http://doi.org/10.1016/j.dib.2019.104267

Nawaz Ali, S., Dubey, J., Morthekai, P., Sharma, A., Singh, R., Prizomwala, S., 2019. Climate forcing and the initiation of glacier advance during MIS-2 in the North Sikkim Himalaya, India. Journal of Asian Earth Sciences 174, 381-388. http://doi.org/10.1016/j.jseaes.2019.02.005

Rana, N., Sharma, S., Ali, S.N., Singh, S., Shukla, A.D., 2019. Investigating the sensitivity of glaciers to climate variability since the MIS-2 in the upper Ganga catchment (Saraswati valley), Central Himalaya. Geomorphology 346, 106854. http://doi.org/10.1016/j.geomorph.2019.106854

Rice, J.M., Ross, M., Paulen, R.C., Kelley, S.E., Briner, J.P., Neudorf, C.M., Lian, O.B., 2019. Refining the ice flow chronology and subglacial dynamics across the migrating Labrador Divide of the Laurentide Ice Sheet with age constraints on deglaciation. Journal of Quaternary Science 34, 519-535. http://doi.org/10.1002/jqs.3138

Smedley, R.K., Buylaert, J.P., Újvári, G., 2019. Comparing the accuracy and precision of luminescence ages for partially-bleached sediments using single grains of K-feldspar and quartz. Quaternary Geochronology 53, 101007. http://doi.org/10.1016/j.quageo.2019.101007

Vandenberghe, J., French, H.M., Jin, H., Wang, X., Yi, S., He, R., 2019. The extent of permafrost during the Last Permafrost Maximum (LPM) on the Ordos Plateau, north China. Quaternary Science Reviews 214, 87-97. http://doi.org/10.1016/j.quascirev.2019.04.019

- lacustrine

Adams, K.D., Rhodes, E.J., 2019. Late Holocene paleohydrology of Walker Lake and the Carson Sink in the western Great Basin, Nevada, USA. Quaternary Research 92, 165-182. http://doi.org/10.1017/qua.2018.151

An, F., Lai, Z., Liu, X., Wang, Y., Chang, Q., Lu, B., Yang, X., 2018. Luminescence chronology and radiocarbon reservoir age determination of lacustrine sediments from the Heihai lake, Ne Qinghai-Tibetan Plateau and its paleoclimate implications. Journal of Earth Science 29, 695-706. http://doi.org/10.1007/s12583-017-0972-9

Carr, A.S., Hay, A.S., Powell, D.M., Livingstone, I., 2019. Testing post-IR IRSL luminescence dating methods in the southwest Mojave Desert, California, USA. Quaternary Geochronology 49, 85-91. http://doi.org/10.1016/j.quageo.2018.05.006

Chen, F., Feng, J.-L., Hu, H.-P., Zhang, J.-F., Gao, S.-P., Liu, X.-M., 2017. Potential forcing mechanisms of Holocene lake-level changes at Nam Co, Tibetan Plateau: Inferred from the stable isotopic composition of shells of the gastropod Radix. The Holocene 27, 594-604. http://doi.org/10.1177/0959683616670247

Chen, T., Lai, Z., Liu, S., Wang, Y., Wang, Z.-t., Miao, X., An, F., Yu, L., Han, F., 2019. Luminescence chronology and palaeoenvironmental significance of limnic relics from the Badain Jaran Desert, northern China. Journal of Asian Earth Sciences 177, 240-249. http://doi.org/10.1016/j.jseaes.2019.03.024

Cohen, T.J., Meyer, M.C., May, J.-H., 2018. Identifying extreme pluvials in the last millennia using optical dating of single grains of quartz from shorelines on Australia's largest lake. The Holocene 28, 150-165. http://doi.org/10.1177/0959683617715700

Diaz, N., Armitage, S.J., Verrecchia, E.P., Herman, F., 2019. OSL dating of a carbonate island in the Chobe Enclave, NW Botswana. Quaternary Geochronology 49, 172-176. http://doi.org/10.1016/j.quageo.2018.03.001

Lapointe, F., Francus, P., Stoner, J.S., Abbott, M.B., Balascio, N.L., Cook, T.L., Bradley, R.S., Forman, S.L., Besonen, M., St-Onge, G., 2019. Chronology and sedimentology of a new 2.9 ka annually laminated record from South Sawtooth Lake, Ellesmere Island. Quaternary Science Reviews 222, 105875. http://doi.org/10.1016/j.quascirev.2019.105875

Long, H., Tsukamoto, S., Buylaert, J.-P., Murray, A.S., Jain, M., Frechen, M., 2019. Late Quaternary OSL chronologies from the Qinghai Lake (NE Tibetan Plateau): Inter-comparison of quartz and K-feldspar ages to assess the pre-depositional bleaching. Quaternary Geochronology 49, 159-164. http://doi.org/10.1016/j.quageo.2018.05.003

Nowacki, D., Langan, C.C.M., Kadereit, A., Pint, A., Wunderlich, J., 2019. 'Lake Gorgana' - A paleolake in the Lower Danube Valley revealed using multi-proxy and regionalisation approaches. Quaternary International 511, 107-123. http://doi.org/10.1016/j.quaint.2018.09.021

Píšková, A., Roman, M., Bulínová, M., Pokorný, M., Sanderson, D., Cresswell, A., Lirio, J.M., Coria, S.H., Nedbalová, L., Lami, A., Musazzi, S., Van de Vijver, B., Nývlt, D., Kopalová, K., 2019. Late-Holocene palaeoenvironmental changes at Lake Esmeralda (Vega Island, Antarctic Peninsula) based on a multi-proxy analysis of laminated lake sediment. The Holocene 29, 1155-1175. http://doi.org/10.1177/0959683619838033

Valero-Garcés, B.L., González-Sampériz, P., Gil-Romera, G., Benito, B.M., Moreno, A., Oliva-Urcia, B., Aranbarri, J., García-Prieto, E., Frugone, M., Morellón, M., Arnold, L.J., Demuro, M., Hardiman, M., Blockley, S.P.E., Lane, C.S., 2019. A multi-dating approach to age-modelling long continental records: The 135 ka El Cañizar de Villarquemado sequence (NE Spain). Quaternary Geochronology 54, 101006. http://doi.org/10.1016/j.quageo.2019.101006

Zhang, Y., Huang, C.C., Shulmeister, J., Guo, Y., Liu, T., Kemp, J., Patton, N.R., Liu, L., Chen, Y., Zhou, Q., Cuan, Y., Zhao, H., Wang, N., 2019. Formation and evolution of the Holocene massive landslide-dammed lakes in the Jishixia Gorges along the upper Yellow River: No relation to China's Great Flood and the Xia Dynasty. Quaternary Science Reviews 218, 267-280. http://doi.org/10.1016/j.quascirev.2019.06.011

- loess

Barta, G., Bradák, B., Novothny, Á., Markó, A., Szeberényi, J., Kiss, K., Kovács, J., 2018. The influence of paleogeomorphology on the stable isotope signals of paleosols. Geoderma 330, 221-231. http://doi.org/10.1016/j.geoderma.2018.05.033

Constantin, D., Veres, D., Panaiotu, C., Anechitei-Deacu, V., Groza, S.M., Begy, R., Kelemen, S., Buylaert, J.P., Hambach, U., Marković, S.B., Gerasimenko, N., Timar-Gabor, A., 2019. Luminescence age constraints on the Pleistocene-Holocene transition recorded in loess sequences across SE Europe. Quaternary Geochronology 49, 71-77. http://doi.org/10.1016/j.quageo.2018.07.011

Li, X., Han, Z., Lu, H., Chen, Y., Li, Y., Yuan, X., Zhou, Y., Jiang, M., Lv, C., 2018. Onset of Xiashu loess deposition in southern China by 0.9 Ma and its implications for regional aridification. Science China Earth Sciences 61, 256-269. http://doi.org/10.1007/s11430-017-9134-2

Li, Y., Song, Y., Yin, Q., Han, L., Wang, Y., 2019. Orbital and millennial northern mid-latitude westerlies over the last glacial period. Climate Dynamics 53, 3315-3324. http://doi.org/10.1007/s00382-019-04704-5

Lü, T., Sun, J., Gong, Z., 2018. Optical dating of eolian deposits since the last interglacial along the northern margin of the Chinese Loess Plateau. Journal of Asian Earth Sciences 155, 154-163. http://doi.org/10.1016/j.jseaes.2017.11.017

Qin, J., Zhou, L., 2018. Luminescence dating of the Zeketai loess section in the Ili Basin, northwestern China: Methodological considerations. Journal of Asian Earth Sciences 155, 146-153. http://doi.org/10.1016/j.jseaes.2017.11.018

Su, Q., Kirby, E., Ren, Z., Zhang, P., Zhang, H., Manopkawee, P., Lei, Q., 2020. Chronology of the Yellow River terraces at Qingtong Gorge (NE Tibet): Insights into evolution of the Yellow River since the Middle Pleistocene. Geomorphology 349, 106889. http://doi.org/10.1016/j.geomorph.2019.106889

Tian, S., Sun, J., Lü, L., Cao, M., Zhang, Z., Lü, T., 2019. Optically stimulated luminescence dating of late Quaternary loess deposits in the coastal region of North China: Provenance and paleoclimatic implications. Quaternary Science Reviews 218, 160-177. http://doi.org/10.1016/j.quascirev.2019.06.022

Torre, G., Gaiero, D.M., Sawakuchi, A.O., Río, I.d., Coppo, R., 2019. Revisiting the chronology and environmental conditions for the accretion of late Pleistocene-early Holocene Pampean loess (Argentina). Quaternary Science Reviews 213, 105-119. http://doi.org/10.1016/j.quascirev.2019.04.018

Wang, H., 2019. First preliminary evidence of Holocene loess in the Illinois River valley. Quaternary Science Reviews 216, 124-126. http://doi.org/10.1016/j.quascirev.2019.06.018

Wang, L., Jia, J., Li, G., Li, Z., Wang, X., Chen, F., 2018. Fine-grained quartz OSL dating chronology of loess sequence from southern Tajikistan: Implications for climate change in arid central Asia during MIS 2. Journal of Asian Earth Sciences 155, 116-123. http://doi.org/10.1016/j.jseaes.2017.11.001

Wang, L., Jia, J., Zhao, H., Liu, H., Duan, Y., Xie, H., Zhang, D.D., Chen, F., 2019. Optical dating of Holocene paleosol development and climate changes in the Yili Basin, arid central Asia. The Holocene 29, 1068-1077. http://doi.org/10.1177/0959683619831432

Wu, J., Lu, H., Yi, S., Xu, Z., Gu, Y., Liang, C., Cui, M., Sun, X., 2019. Establishing a high-resolution luminescence chronology for the Zhenbeitai sand-loess section at Yulin, North-Central China. Quaternary Geochronology 49, 78-84. http://doi.org/10.1016/j.quageo.2018.03.013

Zha, X., Huang, C., Pang, J., Li, Y., Liu, J., Cuan, Y., Wang, N., 2019. Sedimentary records of holocene palaeo-mudflow events in Tianshui basin of the western Loess Plateau, China. Quaternary International 521, 129-137. http://doi.org/10.1016/j.quaint.2019.06.027

Zhang, J., Li, S.-H., Sun, J., Hao, Q., 2018. Fake age hiatus in a loess section revealed by OSL dating of calcrete nodules. Journal of Asian Earth Sciences 155, 139-145. http://doi.org/10.1016/j.jseaes.2017.11.016

Zhang, Y., Chang Huang, C., Tan, Z., Chen, Y., Qiu, H., Huang, C., Li, Y., Zhang, Y., Li, X., Shulmeister, J., Patton, N., Liu, L., Zhu, Y., Wang, N., 2019. Prehistoric and historic overbank floods in the Luoyang Basin along the Luohe River, middle Yellow River basin, China. Quaternary International 521, 118-128. http://doi.org/10.1016/j.quaint.2019.06.023

Zhao, Q., Ding, M., Peng, S., Zhang, W., Song, B., Zhou, R., Yue, J., Liang, M., Zhang, D., 2019. High resolution OSL dating of the late Quaternary loess from Central Shandong Mountains in eastern China and the paleoclimatic implications. IOP Conference Series: Earth and Environmental Science 349, 012037. http://doi.org/10.1088/1755-1315/349/1/012037

- marine

López, G.I., Goodman-Tchernov, B.N., Porat, N., 2018. OSL over-dispersion: A pilot study for the characterisation of extreme events in the shallow marine realm. Sedimentary Geology 378, 35-51. http://doi.org/10.1016/j.sedgeo.2018.09.002

- meteorites

Sears, D.W.G., Sehlke, A., Friedrich, J.M., Rivers, M.L., Ebel, D.S., 2018. X-ray computed tomography of extraterrestrial rocks eradicates their natural radiation record and the information it contains. Meteoritics & Planetary Science 53, 2624-2631. http://doi.org/10.1111/maps.13183

- soil

Larsen, A., May, J.-H., Carah, X., 2019. Late Quaternary biotic and abiotic controls on long-term sediment flux in a northern Australian tropical river system. Earth Surface Processes and Landforms 44, 2494-2509. http://doi.org/10.1002/esp.4652

Rashidi, Z., Sohbati, R., Karimi, A., Farpoor, M.H., Khormali, F., Thompson, W., Murray, A., 2019. Constraining the timing of palaeosol development in Iranian arid environments using OSL dating. Quaternary Geochronology 49, 92-100. http://doi.org/10.1016/j.quageo.2018.04.006

Román-Sánchez, A., Reimann, T., Wallinga, J., Vanwalleghem, T., 2019. Bioturbation and erosion rates along the soil-hillslope conveyor belt, part 1: Insights from single-grain feldspar luminescence. Earth Surface Processes and Landforms 44, 2051-2065. http://doi.org/10.1002/esp.4628

von Suchodoletz, H., Tinapp, C., Lauer, T., Glaser, B., Stäuble, H., Kühn, P., Zielhofer, C., 2019. Distribution of Chernozems and Phaeozems in Central Germany during the Neolithic period. Quaternary International 511, 166-184. http://doi.org/10.1016/j.quaint.2017.10.041

- surface exposure dating

al Khasawneh, S., Murray, A., Abudanah, F., 2019. A first radiometric chronology for the Khatt Shebib megalithic structure in Jordan using the luminescence dating of rock surfaces. Quaternary Geochronology 49, 205-210. http://doi.org/10.1016/j.quageo.2018.02.007

al Khasawneh, S., Murray, A., Thomsen, K., AbuAzizeh, W., Tarawneh, M., 2019. Dating a near eastern desert hunting trap (kite) using rock surface luminescence dating. Archaeological and Anthropological Sciences 11, 2109-2119. http://doi.org/10.1007/s12520-018-0661-3

Brown, N.D., Moon, S., 2019. Revisiting erosion rate estimates from luminescence profiles in exposed bedrock surfaces using stochastic erosion simulations. Earth and Planetary Science Letters 528, 115842. http://doi.org/10.1016/j.epsl.2019.115842

Gliganic, L.A., Meyer, M.C., Sohbati, R., Jain, M., Barrett, S., 2019. OSL surface exposure dating of a lithic quarry in Tibet: Laboratory validation and application. Quaternary Geochronology 49, 199-204. http://doi.org/10.1016/j.quageo.2018.04.012

Lehmann, B., Herman, F., Valla, P.G., King, G.E., Biswas, R.H., 2019. Evaluating post-glacial bedrock erosion and surface exposure duration by coupling in situ optically stimulated luminescence and 10Be dating. Earth Surface Dynamics 7, 633-662. http://doi.org/10.5194/esurf-7-633-2019

Liu, J., Cui, F., Murray, A.S., Sohbati, R., Jain, M., Gao, H., Li, W., Li, C., Li, P., Zhou, T., Chen, J., 2019. Resetting of the luminescence signal in modern riverbed cobbles along the course of the Shiyang River, China. Quaternary Geochronology 49, 184-190. http://doi.org/10.1016/j.quageo.2018.04.004

Sellwood, E.L., Guralnik, B., Kook, M., Prasad, A.K., Sohbati, R., Hippe, K., Wallinga, J., Jain, M., 2019. Optical bleaching front in bedrock revealed by spatially-resolved infrared photoluminescence. Scientific Reports 9, 2611. http://doi.org/10.1038/s41598-019-38815-0

Souza, P.E., Sohbati, R., Murray, A.S., Kroon, A., Clemmensen, L.B., Hede, M.U., Nielsen, L., 2019. Luminescence dating of buried cobble surfaces from sandy beach ridges: a case study from Denmark. Boreas 48, 841-855. http://doi.org/10.1111/bor.12402

- tephra

K, G., Achyuthan, H., Jaiswal, M.K., 2019. The Toba tephra as a late Quaternary stratigraphic marker: Investigations in the Sagileru river basin, Andhra Pradesh, India. Quaternary International 513, 107-123. http://doi.org/10.1016/j.quaint.2019.03.032

- volcanic

Ayala-Arenas, J.S., Cano, N.F., Rivera-Porras, M., Gonzales-Lorenzo, C.D., Watanabe, S., 2019. Dating volcanic ash and pumice stones from volcano El Misti, Peru, by thermoluminescence. Quaternary International 512, 1-5. http://doi.org/10.1016/j.quaint.2018.11.013

Zawacki, E.E., Clarke, A.B., Arrowsmith, J.R., Bonadonna, C., Lynch, D.J., 2019. Tecolote volcano, Pinacate volcanic field (Sonora, Mexico): A case of highly explosive basaltic volcanism and shifting eruptive styles. Journal of Volcanology and Geothermal Research 379, 23-44. http://doi.org/10.1016/j.jvolgeores.2019.04.011

Archaeology applications

al Khasawneh, S., Murray, A., Khalil, L., 2019. Luminescence dating of a transitional Chalcolithic/Bronze Age site in Jordan. Archaeological and Anthropological Sciences 11, 4347-4353. http://doi.org/10.1007/s12520-019-00813-8

al Khasawneh, S., Murray, A., Thomsen, K., AbuAzizeh, W., Tarawneh, M., 2019. Dating a near eastern desert hunting trap (kite) using rock surface luminescence dating. Archaeological and Anthropological Sciences 11, 2109-2119. http://doi.org/10.1007/s12520-018-0661-3

Anderson, S.L., Feathers, J.K., 2019. Applying luminescence dating of ceramics to the problem of dating Arctic archaeological sites. Journal of Archaeological Science 112, 105030. http://doi.org/10.1016/j.jas.2019.105030

Antoine, P., Moncel, M.-H., Voinchet, P., Locht, J.-L., Amselem, D., Hérisson, D., Hurel, A., Bahain, J.-J., 2019. The earliest evidence of Acheulian occupation in Northwest Europe and the rediscovery of the Moulin Quignon site, Somme valley, France. Scientific Reports 9, 13091. http://doi.org/10.1038/s41598-019-49400-w

Armitage, S.J., Krishna, A., Parker, L.E., King, G.E., 2019. Optically stimulated luminescence dating of heat retainer hearths from the Sahara: Insights into signal accumulation and measurement. Quaternary Geochronology 49, 249-253. http://doi.org/10.1016/j.quageo.2018.03.004

Atlıhan, M.A., Koralay, T., Sahiner, E., 2018. Luminescence dating and mineralogical investigations of bricks from Erikli basilica in Stratonikeia ancient city (SW-Turkey). Mediterranean Archaeology and Archaeometry 18, 77-91. http://doi.org/10.5281/zenodo.1069527

Bailiff, I.K., Jankowski, N., Gerrard, C.M., Gutiérrez, A., Wilkinson, K.N., 2019. Luminescence dating of sediment mounds associated with shaft and gallery irrigation systems. Journal of Arid Environments 165, 34-45. http://doi.org/10.1016/j.jaridenv.2019.02.004

Bartz, M., Arnold, L.J., Demuro, M., Duval, M., King, G.E., Rixhon, G., Álvarez Posada, C., Parés, J.M., Brückner, H., 2019. Single-grain TT-OSL dating results confirm an Early Pleistocene age for the lower Moulouya River deposits (NE Morocco). Quaternary Geochronology 49, 138-145. http://doi.org/10.1016/j.quageo.2018.04.007

Carter, T., Contreras, D.A., Holcomb, J., Mihailović, D.D., Karkanas, P., Guérin, G., Taffin, N., Athanasoulis, D., Lahaye, C., 2019. Earliest occupation of the Central Aegean (Naxos), Greece: Implications for hominin and *Homo sapiens'* behavior and dispersals. Science Advances 5, eaax0997. http://doi.org/10.1126/sciadv.aax0997

Crassard, R., Hilbert, Y.H., Preusser, F., Wulf, G., Schiettecatte, J., 2019. Middle Palaeolithic occupations in central Saudi Arabia during MIS 5 and MIS 7: new insights on the origins of the peopling of Arabia. Archaeological and Anthropological Sciences 11, 3101-3120. http://doi.org/10.1007/s12520-018-0743-2

Davis, L.G., Madsen, D.B., Becerra-Valdivia, L., Higham, T., Sisson, D.A., Skinner, S.M., Stueber, D., Nyers, A.J., Keen-Zebert, A., Neudorf, C., Cheyney, M., Izuho, M., Iizuka, F., Burns, S.R., Epps, C.W., Willis, S.C., Buvit, I., 2019. Late Upper Paleolithic occupation at Cooper's Ferry, Idaho, USA, ~16,000 years ago. Science 365, 891-897. http://doi.org/10.1126/science.aax9830

Demuro, M., Arnold, L.J., Aranburu, A., Gómez-Olivencia, A., Arsuaga, J.-L., 2019. Single-grain OSL dating of the Middle Palaeolithic site of Galería de las Estatuas, Atapuerca (Burgos, Spain). Quaternary Geochronology 49, 254-261. http://doi.org/10.1016/j.quageo.2018.02.006

Duval, M., Fang, F., Suraprasit, K., Jaeger, J.-J., Benammi, M., Chaimanee, Y., Cibanal, J.I., Grün, R., 2019. Direct ESR dating of the Pleistocene vertebrate assemblage from Khok Sung locality, Nakhon Ratchasima Province, Northeast Thailand. Palaeontologia Electronica 22.3.69, 1-25. http://doi.org/10.26879/941

Falguères, C., Ghaleb, B., Tombret, O., Ben Arous, E., Richard, M., Moigne, A.M., Saos, T., Frouin, M., Caparros, M., Barroso-Ruiz, C., 2019. ESR/U-series dates on Equus teeth from the Middle Pleistocene Acheulean site of Cueva del Angel, Spain. Quaternary Geochronology 49, 297-302. http://doi.org/10.1016/j.quageo.2018.02.003

Feathers, J., More, G.M., Quinteros, P.S., Burkholder, J.E., 2019. IRSL dating of rocks and sediments from desert geoglyphs in coastal Peru. Quaternary Geochronology 49, 177-183. http://doi.org/10.1016/j.quageo.2018.07.009

Groza, S.M., Hambach, U., Veres, D., Vulpoi, A., Händel, M., Einwögerer, T., Simon, U., Neugebauer-Maresch, C., Timar-Gabor, A., 2019. Optically stimulated luminescence ages for the Upper Palaeolithic site Krems-Wachtberg, Austria. Quaternary Geochronology 49, 242-248. http://doi.org/10.1016/j.quageo.2018.04.005

Gueli, A.M., Garro, V., Pasquale, S., Stella, G., 2018. Chronology of the crypt of Sant'Agata La Vetere In Catania obtained by thermoluminescence. Mediterranean Archaeology and Archaeometry 18, 27-35. http://doi.org/10.5281/zenodo.1069516

Guibert, P., Urbanová, P., Lanos, P., Prigent, D., 2018. The detection of material reuse in ancient construction What is the role of dating methods? Ædificare: Revue internationale d'histoire de la construction 2, 89-117. http://doi.org/10.15122/isbn.978-2-406-09276-6.p.0089

Han, F., Shao, Q., Bahain, J.-J., Sun, X., Yin, G., 2019. Coupled ESR and U-series dating of Middle Pleistocene hominin site Bailongdong cave, China. Quaternary Geochronology 49, 291-296. http://doi.org/10.1016/j.quageo.2018.02.004

Hu, Y., Marwick, B., Zhang, J.-F., Rui, X., Hou, Y.-M., Yue, J.-P., Chen, W.-R., Huang, W.-W., Li, B., 2019. Late Middle Pleistocene Levallois stone-tool technology in southwest China. Nature 565, 82-85. http://doi.org/10.1038/s41586-018-0710-1

Jacobs, Z., Li, B., Shunkov, M.V., Kozlikin, M.B., Bolikhovskaya, N.S., Agadjanian, A.K., Uliyanov, V.A., Vasiliev, S.K., O'Gorman, K., Derevianko, A.P., Roberts, R.G., 2019. Timing of archaic hominin occupation of Denisova Cave in southern Siberia. Nature 565, 594-599. http://doi.org/10.1038/s41586-018-0843-2

Javel, J.-B., Urbanová, P., Guibert, P., Gaillard, H., 2019. Chronological study of the Saint-Jean-Baptiste de la Cité chapel in Périgueux, France: the contribution of mortar luminescence dating to the history of local Christianity, in: Vecchiattini, R. (Ed.), Archeologia dell'Architettura, XXIV, 2019 – La datazione delle malte in architettura tra archeologia e archeometria. All'Insegna del Giglio, pp. 97-114. www.insegnadelgiglio.it

Jin, J., Huang, Y., Zhang, Y., Li, Z., Fan, X., Ling, Z., Zheng, F., Cheng, Y., Xu, X., Li, Z., Zhang, W., 2019. Optically stimulated luminescence ages of the Hengyu site and their implications for anthropogenic

activities in the Fuzhou Basin, South China. Journal of Quaternary Science 34, 548-557. http://doi.org/10.1002/jqs.3143

Kadowaki, S., Tamura, T., Sano, K., Kurozumi, T., Maher, L.A., Wakano, J.Y., Omori, T., Kida, R., Hirose, M., Massadeh, S., Henry, D.O., 2019. Lithic technology, chronology, and marine shells from Wadi Aghar, southern Jordan, and Initial Upper Paleolithic behaviors in the southern inland Levant. Journal of Human Evolution 135, 102646. http://doi.org/10.1016/j.jhevol.2019.102646

Kang, P.-Y., 2019. Age determination of the Neolithic Joohyondong Cave site in the Democratic People's Republic of Korea. Journal of Archaeological Science: Reports 24, 796-803. http://doi.org/10.1016/j.jasrep.2019.02.014

Lahaye, C., Guérin, G., Gluchy, M., Hatté, C., Fontugne, M., Clemente-Conte, I., Santos, J.C., Villagran, X.S., Da Costa, A., Borges, C., Guidon, N., Boëda, E., 2019. Another site, same old song: The Pleistocene-Holocene archaeological sequence of Toca da Janela da Barra do Antonião-North, Piauí, Brazil. Quaternary Geochronology 49, 223-229. http://doi.org/10.1016/j.quageo.2018.03.006

Łanczont, M., Madeyska, T., Hołub, B., Komar, M., Mroczek, P., Standzikowski, K., Valde-Nowak, P., Kraszewska, A., Cieśla, M., Skłucki, J., 2019. Late Glacial environment and human settlement of the Central Western Carpathians: A case study of the Nowa Biała 1 open-air site (Podhale Region, southern Poland). Quaternary International 512, 113-132. http://doi.org/10.1016/j.quaint.2019.02.036

Lukich, V., Porat, N., Faershtein, G., Cowling, S., Chazan, M., 2019. New chronology and stratigraphy for Kathu Pan 6, South Africa. Journal of Paleolithic Archaeology 2, 235-257. http://doi.org/10.1007/s41982-019-00031-7

Maíllo-Fernández, J.-M., Marín, J., Solano-Megías, I., Uribelarrea, D., Martín-Perea, D., Aramendi, J., Medialdea, A., Arteaga, C., Pernas-Hernández, M., Gidna, A., Neogi, S., Baudot, E., Narváez, C., Mabulla, A., 2019. Victoria Cabrera Site: A Middle Stone Age site at Olduvai Gorge, Tanzania. Quaternary International 526, 129-154. http://doi.org/10.1016/j.quaint.2019.07.032

Mejia-Bernal, J.R., Ayala-Arenas, J.S., Cano, N.F., Rios-Orihuela, J.F., Gonzales-Lorenzo, C.D., Watanabe, S., 2020. Dating and determination of firing temperature of ancient potteries from Yumina archaeological site, Arequipa, Peru. Applied Radiation and Isotopes 155, 108930. http://doi.org/10.1016/j.apradiso.2019.108930

Méndez-Quintas, E., Demuro, M., Arnold, L.J., Duval, M., Pérez-González, A., Santonja, M., 2019. Insights into the late stages of the Acheulean technocomplex of Western Iberia from the Arbo site (Galicia, Spain). Journal of Archaeological Science: Reports 27, 101934. http://doi.org/10.1016/j.jasrep.2019.101934

Mercier, N., Martin, L., Kreutzer, S., Moineau, V., Cliquet, D., 2019. Dating the palaeolithic footprints of 'Le Rozel' (Normandy, France). Quaternary Geochronology 49, 271-277. http://doi.org/10.1016/j.quageo.2017.12.005

Mien, N.Q., Bac, N.Q., Loat, B.V., Hung, V.A., 2019. Thermoluminesence and Radiocarbon Dates in the Brick Structures of GoThap Site in the Lower Mekong Delta Basin. International Journal of Archaeology 7, 17-23. http://doi.org/10.11648/j.ija.20190701.13

Moreno, D., Duval, M., Rubio-Jara, S., Panera, J., Bahain, J.J., Shao, Q., Pérez-González, A., Falguères, C., 2019. ESR dating of Middle Pleistocene archaeo-paleontological sites from the Manzanares and Jarama river valleys (Madrid basin, Spain). Quaternary International 520, 23-38. http://doi.org/10.1016/j.quaint.2017.09.003

Moroni, A., Boschian, G., Crezzini, J., Montanari-Canini, G., Marciani, G., Capecchi, G., Arrighi, S., Aureli, D., Berto, C., Freguglia, M., Araujo, A., Scaramucci, S., Hublin, J.J., Lauer, T., Benazzi, S., Parenti, F., Bonato, M., Ricci, S., Talamo, S., Segre, A.G., Boschin, F., Spagnolo, V., 2019. Late Neandertals in central Italy. High-resolution chronicles from Grotta dei Santi (Monte Argentario - Tuscany). Quaternary Science Reviews 217, 130-151. http://doi.org/10.1016/j.quascirev.2018.11.021

Nasab, H.V., Berillon, G., Jamet, G., Hashemi, M., Jayez, M., Khaksar, S., Anvari, Z., Guérin, G., Heydari, M., Kharazian, M.A., Puaud, S., Bonilauri, S., Zeitoun, V., Sévêque, N., Khatooni, J.D., Khaneghah, A.A., 2019. The open-air Paleolithic site of Mirak, northern edge of the Iranian Central Desert (Semnan, Iran): Evidence of repeated human occupations during the late Pleistocene. Comptes Rendus Palevol 18, 465-478. http://doi.org/10.1016/j.crpv.2019.02.005

Noppradit, P., Symanczyk, A., Zöller, L., Brückner, H., Stock, F., 2019. Methodological approach for dating harbor sediments by using luminescence dating—a case study in Ephesus, Western Turkey. Archaeological and Anthropological Sciences 11, 3143-3153. http://doi.org/10.1007/s12520-018-0739-y

Panzeri, L., Caroselli, M., Galli, A., Lugli, S., Martini, M., Sibilia, E., 2019. Mortar OSL and brick TL dating: The case study of the UNESCO world heritage site of Modena. Quaternary Geochronology 49, 236-241. http://doi.org/10.1016/j.quageo.2018.03.005

Puttagan, T., Chawchai, S., Surakiatchai, P., Chalorsantisakul, S., Preusser, F., 2019. Luminescence dating of brick constructions being part of Songkhla City Wall, Southern Thailand. Archaeological and Anthropological Sciences 11, 5393-5403. http://doi.org/10.1007/s12520-019-00878-5

Real, C., Eixea, A., Sanchis, A., Morales, J.V., Klasen, N., Zilhão, J., Villaverde, V., 2018. Abrigo de la Quebrada Level IV (Valencia, Spain): Interpreting a Middle Palaeolithic Palimpsest from a Zooarchaeological and Lithic Perspective. Journal of Paleolithic Archaeologyhttp://doi.org/10.1007/s41982-018-0012-z

Richard, M., Falguères, C., Pons-Branchu, E., Foliot, L., Guillem, P.M., Martínez-Valle, R., Eixea, A., Villaverde, V., 2019. ESR/U-series chronology of early Neanderthal occupations at Cova Negra (Valencia, Spain). Quaternary Geochronology 49, 283-290. http://doi.org/10.1016/j.quageo.2018.05.004

Richard, M., Falguères, C., Valladas, H., Ghaleb, B., Pons-Branchu, E., Mercier, N., Richter, D., Conard, N.J., 2019. New electron spin resonance (ESR) ages from Geißenklösterle Cave: A chronological study of the Middle and early Upper Paleolithic layers. Journal of Human Evolution 133, 133-145. http://doi.org/10.1016/j.jhevol.2019.05.014

Rodrigues, A.L., Dias, M.I., Valera, A.C., Rocha, F., Prudêncio, M.I., Marques, R., Cardoso, G., Russo, D., 2019. Geochemistry, luminescence and innovative dose rate determination of a Chalcolithic calcite-rich negative feature. Journal of Archaeological Science: Reports 26, 101887. http://doi.org/10.1016/j.jasrep.2019.101887

Sahnouni, M., Parés, J.M., Duval, M., Cáceres, I., Harichane, Z., van der Made, J., Pérez-González, A., Abdessadok, S., Kandi, N., Derradji, A., Medig, M., Boulaghraif, K., Semaw, S., 2018. 1.9-million- and 2.4-million-year-old artifacts and stone tool–cutmarked bones from Ain Boucherit, Algeria. Science 362, 1297-1301. http://doi.org/10.1126/science.aau0008

Sánchez-Pardo, J.C., Blanco-Rotea, R., Sanjurjo-Sánchez, J., Barrientos-Rodríguez, V., 2019. Reusing stones in medieval churches: a multidisciplinary approach to San Martiño de Armental (NW Spain). Archaeological and Anthropological Sciences 11, 2073-2096. http://doi.org/10.1007/s12520-018-0655-1

Scerri, E.M.L., Shipton, C., Clark-Balzan, L., Frouin, M., Schwenninger, J.-L., Groucutt, H.S., Breeze, P.S., Parton, A., Blinkhorn, J., Drake, N.A., Jennings, R., Cuthbertson, P., Omari, A.A., Alsharekh, A.M., Petraglia, M.D., 2018. The expansion of later Acheulean hominins into the Arabian Peninsula. Scientific Reports 8, 17165. http://doi.org/10.1038/s41598-018-35242-5

Schaarschmidt, M., Fu, X., Li, B., Marwick, B., Khaing, K., Douka, K., Roberts, R.G., 2019. pIRIR and IR-RF dating of archaeological deposits at Badahlin and Gu Myaung Caves – First luminescence ages for Myanmar. Quaternary Geochronology 49, 262-270. http://doi.org/10.1016/j.quageo.2018.01.001

Schmidt, C., Anghelinu, M., Hambach, U., Veres, D., Lehmkuhl, F., 2020. Reassessing the timeframe of Upper Palaeolithic deposits in the Ceahlău Basin (Eastern Carpathians, Romania): Geochronological and archaeological implications. Quaternary Geochronology 55, 101020. http://doi.org/10.1016/j.quageo.2019.101020

Strebler, D., Brill, D., Richter, J., Brückner, H., 2019. Using DRAC in complex geometries - TL dating of heated flints from Taibeh, Jordan. Quaternary Geochronology 49, 4-7. http://doi.org/10.1016/j.quageo.2018.07.002

Theodorakopoulou, K., Kyriakopoulos, K., Stamoulis, K., Rizza, M., Athanassas, C.D., Sulpizio, R., Alçiçek, M.C., 2019. Chronological evidence for a pre-Minoan age of pyroclastic deposits on Anafi Island, Cyclades, Greece. Mediterranean Geoscience Reviews 1, 17-24. http://doi.org/10.1007/s42990-019-00005-5

Urbanová, P., 2019. Luminescence dating of mortars by “single grain” procedure and its potential for building archaeology, in: Vecchiattini, R. (Ed.), Archeologia dell'Architettura, XXIV, 2019 – La datazione delle malte in architettura tra archeologia e archeometria. All’Insegna del Giglio, pp. 81-96. www.insegnadelgiglio.it

Vejrostová, L., Lisá, L., Parma, D., Bajer, A., Hajnalová, M., Kočárová, R., Moska, P., Pacina, J., 2019. Human-induced prehistoric soil buried in the flood plain of Svratka River, Czech Republic. The Holocene 29, 565-577. http://doi.org/10.1177/0959683618824785

Weiss, M., Lauer, T., Wimmer, R., Pop, C.M., 2018. The variability of the Keilmesser-concept: A case study from central Germany. Journal of Paleolithic Archaeology 1, 202-246. http://doi.org/10.1007/s41982-018-0013-y

Wiśniewski, A., Lauer, T., Chłoń, M., Pyżewicz, K., Weiss, M., Badura, J., Kalicki, T., Zarzecka-Szubińska, K., 2019. Looking for provisioning places of shaped tools of the late Neanderthals: A study of a Micoquian open-air site, Pietraszyn 49a (southwestern Poland). Comptes Rendus Palevol 18, 367-389. http://doi.org/10.1016/j.crpv.2019.01.003

Zander, A., Strebler, D., Classen, E., Rethemeyer, J., Brückner, H., 2019. Roman traces in Germania magna: New thermoluminescence and pIRIR290 data from a lime kiln at Bergisch Gladbach, Germany. Archaeometry 61, 506-518. http://doi.org/10.1111/arcm.12435

Zhang, H., Chang, F., Li, H., Peng, G., Duan, L., Meng, H., Yang, X., Wei, Z., 2018. OSL and AMS 14C age of the most complete mammoth fossil skeleton from northeastern China and its paleoclimate significance. Radiocarbon 61, 347-358. http://doi.org/10.1017/RDC.2018.48

Zhang, J.-F., Li, Y.-Y., Han, Y.-S., Wang, J.-K., 2019. Luminescence dating of weathered sediments from the Paleolithic site of Fengshuzui in northern Hunan province, China. Quaternary Geochronology 49, 211-217. http://doi.org/10.1016/j.quageo.2018.07.003

Zhang, X.L., Ha, B.B., Wang, S.J., Chen, Z.J., Ge, J.Y., Long, H., He, W., Da, W., Nian, X.M., Yi, M.J., Zhou, X.Y., Zhang, P.Q., Jin, Y.S., Bar-Yosef, O., Olsen, J.W., Gao, X., 2018. The earliest human occupation of the high-altitude Tibetan Plateau 40 thousand to 30 thousand years ago. Science 362, 1049-1051. http://doi.org/10.1126/science.aat8824

Various ESR applications

Antoine, P., Moncel, M.-H., Voinchet, P., Locht, J.-L., Amselem, D., Hérisson, D., Hurel, A., Bahain, J.-J., 2019. The earliest evidence of Acheulian occupation in Northwest Europe and the rediscovery of the Moulin Quignon site, Somme valley, France. Scientific Reports 9, 13091. http://doi.org/10.1038/s41598-019-49400-w

del Val, M., Duval, M., Medialdea, A., Bateman, M.D., Moreno, D., Arriolabengoa, M., Aranburu, A., Iriarte, E., 2019. First chronostratigraphic framework of fluvial terrace systems in the eastern Cantabrian margin (Bay of Biscay, Spain). Quaternary Geochronology 49, 108-114. http://doi.org/10.1016/j.quageo.2018.07.001

Duval, M., Fang, F., Suraprasit, K., Jaeger, J.-J., Benammi, M., Chaimanee, Y., Cibanal, J.I., Grün, R., 2019. Direct ESR dating of the Pleistocene vertebrate assemblage from Khok Sung locality, Nakhon Ratchasima Province, Northeast Thailand. Palaeontologia Electronica 22.3.69, 1-25. http://doi.org/10.26879/941

Falguères, C., Ghaleb, B., Tombret, O., Ben Arous, E., Richard, M., Moigne, A.M., Saos, T., Frouin, M., Caparros, M., Barroso-Ruiz, C., 2019. ESR/U-series dates on Equus teeth from the Middle Pleistocene Acheulean site of Cueva del Angel, Spain. Quaternary Geochronology 49, 297-302. http://doi.org/10.1016/j.quageo.2018.02.003

Gao, H., Li, Z., Liu, F., Wu, Y., Li, P., Zhao, X., Li, F., Guo, J., Liu, C., Pan, B., Jia, H., 2020. Terrace formation and river valley development along the lower Taohe River in central China. Geomorphology 348, 106885. http://doi.org/10.1016/j.geomorph.2019.106885

Garon, H., Voinchet, P., Bahain, J.J., Despriée, J., Courcimault, G., Tissoux, H., Falguères, C., 2017. Datation ESR de quartz fluviatiles : nouvelles données chronologiques pour le secteur « intermédiaire » de la vallée de la Creuse (Indre, région Centre, France). Quaternaire 28, 73-85. http://doi.org/10.4000/quaternaire.7838

Han, F., Shao, Q., Bahain, J.-J., Sun, X., Yin, G., 2019. Coupled ESR and U-series dating of Middle Pleistocene hominin site Bailongdong cave, China. Quaternary Geochronology 49, 291-296. http://doi.org/10.1016/j.quageo.2018.02.004

Kaya-Keleş, Ş., Polymeris, G.S., Meriç, N., 2019. A component resolved study on the stable signal of Merck α-quartz: Tentative correlation among TL peaks, OSL components and EPR signals. Nuclear Instruments and Methods in Physics Research Section B: Beam Interactions with Materials and Atoms 458, 44-56. http://doi.org/10.1016/j.nimb.2019.07.029

Korsakova, O., Molodkov, A., Yelovicheva, Y., Kolka, V., 2019. Middle Pleistocene marine deposits on the Kola Peninsula (NW Russia). Quaternary International 509, 3-16. http://doi.org/10.1016/j.quaint.2018.09.019

Mejia-Bernal, J.R., Ayala-Arenas, J.S., Cano, N.F., Rios-Orihuela, J.F., Gonzales-Lorenzo, C.D., Watanabe, S., 2020. Dating and determination of firing temperature of ancient potteries from Yumina archaeological site, Arequipa, Peru. Applied Radiation and Isotopes 155, 108930. http://doi.org/10.1016/j.apradiso.2019.108930

Méndez-Quintas, E., Demuro, M., Arnold, L.J., Duval, M., Pérez-González, A., Santonja, M., 2019. Insights into the late stages of the Acheulean technocomplex of Western Iberia from the Arbo site (Galicia, Spain). Journal of Archaeological Science: Reports 27, 101934. http://doi.org/10.1016/j.jasrep.2019.101934

Möller, P., Benediktsson, Í.Ö., Anjar, J., Bennike, O., Bernhardson, M., Funder, S., Håkansson, L.M., Lemdahl, G., Licciardi, J.M., Murray, A.S., Seidenkrantz, M.-S., 2019. Data set on sedimentology, palaeoecology and chronology of Middle to Late Pleistocene deposits on the Taimyr Peninsula, Arctic Russia. Data in Brief 25, 104267. http://doi.org/10.1016/j.dib.2019.104267

Moreno, D., Duval, M., Rubio-Jara, S., Panera, J., Bahain, J.J., Shao, Q., Pérez-González, A., Falguères, C., 2019. ESR dating of Middle Pleistocene archaeo-paleontological sites from the Manzanares and Jarama river valleys (Madrid basin, Spain). Quaternary International 520, 23-38. http://doi.org/10.1016/j.quaint.2017.09.003

Richard, M., Falguères, C., Pons-Branchu, E., Foliot, L., Guillem, P.M., Martínez-Valle, R., Eixea, A., Villaverde, V., 2019. ESR/U-series chronology of early Neanderthal occupations at Cova Negra (Valencia, Spain). Quaternary Geochronology 49, 283-290. http://doi.org/10.1016/j.quageo.2018.05.004

Richard, M., Falguères, C., Valladas, H., Ghaleb, B., Pons-Branchu, E., Mercier, N., Richter, D., Conard, N.J., 2019. New electron spin resonance (ESR) ages from Geißenklösterle Cave: A chronological study of the Middle and early Upper Paleolithic layers. Journal of Human Evolution 133, 133-145. http://doi.org/10.1016/j.jhevol.2019.05.014

Sahnouni, M., Parés, J.M., Duval, M., Cáceres, I., Harichane, Z., van der Made, J., Pérez-González, A., Abdessadok, S., Kandi, N., Derradji, A., Medig, M., Boulaghraif, K., Semaw, S., 2018. 1.9-million- and 2.4-million-year-old artifacts and stone tool–cutmarked bones from Ain Boucherit, Algeria. Science 362, 1297-1301. http://doi.org/10.1126/science.aau0008

Voinchet, P., Yin, G., Falguères, C., Liu, C., Han, F., Sun, X., Bahain, J.-J., 2019. Dating of the stepped quaternary fluvial terrace system of the Yellow River by electron spin resonance (ESR). Quaternary Geochronology 49, 278-282. http://doi.org/10.1016/j.quageo.2018.08.001

Xiang, F., Huang, H., Ogg, J.G., Zhu, H., Kang, D., 2020. Quaternary sediment characteristics and paleoclimate implications of deposits in the Three Gorges and Yichang areas of the Yangtze River. Geomorphology 351, 106981. http://doi.org/10.1016/j.geomorph.2019.106981

Yang, H.L., Chen, J., Yao, L., Liu, C.R., Shimamoto, T., Thompson Jobe, J.A., 2019. Resetting of OSL/TL/ESR signals by frictional heating in experimentally sheared quartz gouge at seismic slip rates. Quaternary Geochronology 49, 52-56. http://doi.org/10.1016/j.quageo.2018.05.005

Basic research

Arnold, L.J., Demuro, M., Spooner, N.A., Prideaux, G.J., McDowell, M.C., Camens, A.B., Reed, E.H., Parés, J.M., Arsuaga, J.L., Bermúdez de Castro, J.M., Carbonell, E., 2019. Single-grain TT-OSL bleaching characteristics: Insights from modern analogues and OSL dating comparisons. Quaternary Geochronology 49, 45-51. http://doi.org/10.1016/j.quageo.2018.01.004

Chauhan, N., Singhvi, A.K., 2019. Changes in the optically stimulated luminescence (OSL) sensitivity of single grains of quartz during the measurement of natural OSL: Implications for the reliability of optical ages. Quaternary Geochronology 53, 101004. http://doi.org/10.1016/j.quageo.2019.101004

Correcher, V., Garcia-Guinea, J., Boronat, C., Gómez-Ros, J.M., 2019. Radiation effect on the UV-green thermally stimulated luminescence emission of a natural Na-rich aluminosilicate. Radiation Physics and Chemistry 164, 108383. http://doi.org/10.1016/j.radphyschem.2019.108383

Correcher, V., Garcia-Guinea, J., Rodriguez-Lazcano, Y., 2018. Thermally stimulated luminescence of a natural layered double hydroxide. Journal of Thermal Analysis and Calorimetry 133, 1253-1257. http://doi.org/10.1007/s10973-018-7205-z

del Río, I., Sawakuchi, A.O., Giordano, D., Mineli, T.D., Nogueira, L., Abede, T., Atencio, D., 2019. Athermal stability, bleaching behavior and dose response of luminescence signals from almandine and kyanite. Ancient TL 37, 11-21. http://ancienttl.org/ATL_37-1_2019/ATL_37-1_delRio_p11-1.pdf

Faershtein, G., Guralnik, B., Lambert, R., Matmon, A., Porat, N., 2018. Investigating the thermal stability of TT-OSL main source trap. Radiation Measurements 119, 102-111. http://doi.org/10.1016/j.radmeas.2018.09.010

Faershtein, G., Porat, N., Matmon, A., 2019. Natural saturation of OSL and TT-OSL signals of quartz grains from Nilotic origin. Quaternary Geochronology 49, 146-152. http://doi.org/10.1016/j.quageo.2018.04.002

Fiorentino, S., Vandini, M., Chinni, T., Caccia, M., Martini, M., Galli, A., 2019. Colourants and opacifiers of mosaic glass tesserae from Khirbet al-Mafjar (Jericho, Palestine): addressing technological issues by a multi-analytical approach and evaluating the potentialities of thermoluminescence and optically stimulated luminescence dating. Archaeological and Anthropological Sciences 11, 337-359. http://doi.org/10.1007/s12520-017-0555-9

Friedrich, J., Kreutzer, S., Schmidt, C., 2018. Making the invisible visible: observing the UV-reversal effect in quartz using radiofluorescence. Journal of Physics D: Applied Physics 51, 335105. http://doi.org/10.1088/1361-6463/aacfd0

Galli, A., Caccia, M., Martini, M., Panzeri, L., Maspero, F., Fiorentino, S., Vandini, M., Sibilia, E., 2019. Applying the "pre-bleached with blue LEDs" protocol to date Umayyad mosaic tesserae by thermoluminescence. Quaternary Geochronology 49, 218-222. http://doi.org/10.1016/j.quageo.2018.05.014

Hu, G., Li, S.-H., 2019. Simplified procedures for optical dating of young sediments using quartz. Quaternary Geochronology 49, 31-38. http://doi.org/10.1016/j.quageo.2018.03.009

Kaya-Keleş, Ş., Polymeris, G.S., Meriç, N., 2019. A component resolved study on the stable signal of Merck α-quartz: Tentative correlation among TL peaks, OSL components and EPR signals. Nuclear Instruments and Methods in Physics Research Section B: Beam Interactions with Materials and Atoms 458, 44-56. http://doi.org/10.1016/j.nimb.2019.07.029

King, G.E., Burow, C., Roberts, H.M., Pearce, N.J.G., 2018. Age determination using feldspar: Evaluating fading-correction model performance. Radiation Measurements 119, 58-73. http://doi.org/10.1016/j.radmeas.2018.07.013

Majgier, R., Biernacka, M., Palczewski, P., Mandowski, A., Polymeris, G.S., 2019. Investigation on thermally assisted optically stimulated luminescence (TA – OSL) signal in various sodium chloride samples. Applied Radiation and Isotopes 143, 98-106. http://doi.org/10.1016/j.apradiso.2018.10.019

Mesady, I.A.E., 2019. Investigation on bleaching of infrared radiofluoroscence signal with optimized power of LEDs to match the standard solar spectrum. International Journal of Advanced Research and Publications 3, 227-233. http://www.ijarp.org/published-research-papers/june2019/Investigation-On-Bleaching-Of-Infrared-Radiofluoroscence-Signal-With-Optimized-Power-Of-Leds-To-Match-The-Standard-Solar-Spectrum.pdf

Monti, A.M., Fasoli, M., Panzeri, L., Martini, M., 2019. Investigation of the spectrally resolved TL peaks of quartz in the 70°C–220°C temperature region. Radiation Measurements 127, 106141. http://doi.org/10.1016/j.radmeas.2019.106141

Morthekai, P., Biswas, R.H., Singhvi, A.K., 2019. Charge transport in band-tail states of irradiated alkali feldspar I: Super-Arrhenius kinetics. Physica B: Condensed Matter 561, 103-110. http://doi.org/10.1016/j.physb.2019.03.002

Polymeris, G.S., Şahiner, E., Aşlar, E., Kitis, G., Meriç, N., 2018. Deconvolution of isothermal TA – OSL decay curves from sedimentary quartz using combinations of various contemporary models. Radiation Measurements 119, 93-101. http://doi.org/10.1016/j.radmeas.2018.09.009

Rui, X., Li, B., Guo, Y.J., Zhang, J.F., Yuan, B.Y., Xie, F., 2019. Variability in the thermal stability of OSL signal of single-grain quartz from the Nihewan Basin, North China. Quaternary Geochronology 49, 25-30. http://doi.org/10.1016/j.quageo.2018.04.011

Schmidt, C., Simmank, O., Kreutzer, S., 2019. Time-resolved optically stimulated luminescence of quartz in the nanosecond time domain. Journal of Luminescence 213, 376-387. http://doi.org/10.1016/j.jlumin.2019.05.042

Schmidt, C., Woda, C., 2019. Quartz thermoluminescence spectra in the high-dose range. Physics and Chemistry of Minerals 46, 861-875. http://doi.org/10.1007/s00269-019-01046-w

Sellwood, E.L., Guralnik, B., Kook, M., Prasad, A.K., Sohbati, R., Hippe, K., Wallinga, J., Jain, M., 2019. Optical bleaching front in bedrock revealed by spatially-resolved infrared photoluminescence. Scientific Reports 9, 2611. http://doi.org/10.1038/s41598-019-38815-0

Sfampa, I.K., Polymeris, G.S., Pagonis, V., Kitis, G., 2019. Correlation between isothermal Tl and Irsl in K-Feldspars of various types. Radiation Physics and Chemistry 165, 108386. http://doi.org/10.1016/j.radphyschem.2019.108386

Singh, L.L., Singh, A.N., 2017. An expression for the lifetime in second order kinetics. International Journal of Electronics, Electrical and Computational System 6, 524-528.

Tribolo, C., Kreutzer, S., Mercier, N., 2019. How reliable are our beta-source calibrations? Ancient TL 37, 1-10. http://ancienttl.org/ATL_37-1_2019/ATL_37-1_Tribolo_p1-10.pdf

Williams, O.M., Spooner, N.A., Smith, B.W., Moffatt, J.E., 2018. Extended duration optically stimulated luminescence in quartz. Radiation Measurements 119, 42-51. http://doi.org/10.1016/j.radmeas.2018.09.005

Yang, H.L., Chen, J., Yao, L., Liu, C.R., Shimamoto, T., Thompson Jobe, J.A., 2019. Resetting of OSL/TL/ESR signals by frictional heating in experimentally sheared quartz gouge at seismic slip rates. Quaternary Geochronology 49, 52-56. http://doi.org/10.1016/j.quageo.2018.05.005

Zhang, J., Li, S.-H., 2019. Constructions of standardised growth curves (SGCs) for IRSL signals from K-feldspar, plagioclase and polymineral fractions. Quaternary Geochronology 49, 8-15. http://doi.org/10.1016/j.quageo.2018.05.015

Dose rate issues

Diaz, N., Armitage, S.J., Verrecchia, E.P., Herman, F., 2019. OSL dating of a carbonate island in the Chobe Enclave, NW Botswana. Quaternary Geochronology 49, 172-176. http://doi.org/10.1016/j.quageo.2018.03.001

Duval, M., Fang, F., Suraprasit, K., Jaeger, J.-J., Benammi, M., Chaimanee, Y., Cibanal, J.I., Grün, R., 2019. Direct ESR dating of the Pleistocene vertebrate assemblage from Khok Sung locality, Nakhon Ratchasima Province, Northeast Thailand. Palaeontologia Electronica 22.3.69, 1-25. http://doi.org/10.26879/941

Moreno, D., Duval, M., Rubio-Jara, S., Panera, J., Bahain, J.J., Shao, Q., Pérez-González, A., Falguères, C., 2019. ESR dating of Middle Pleistocene archaeo-paleontological sites from the Manzanares and Jarama river valleys (Madrid basin, Spain). Quaternary International 520, 23-38. http://doi.org/10.1016/j.quaint.2017.09.003

Rodrigues, A.L., Dias, M.I., Valera, A.C., Rocha, F., Prudêncio, M.I., Marques, R., Cardoso, G., Russo, D., 2019. Geochemistry, luminescence and innovative dose rate determination of a Chalcolithic calcite-rich negative feature. Journal of Archaeological Science: Reports 26, 101887. http://doi.org/10.1016/j.jasrep.2019.101887

Strebler, D., Brill, D., Richter, J., Brückner, H., 2019. Using DRAC in complex geometries - TL dating of heated flints from Taibeh, Jordan. Quaternary Geochronology 49, 4-7. http://doi.org/10.1016/j.quageo.2018.07.002

Dosimetry

Jakathamani, S., Annalakshmi, O., Menon, S.N., Kadam, S.Y., Jose, M.T., Venkatraman, B., 2019. Ceramic resistors as optically stimulated luminescent retrospective dosimeters. Radiation Physics and Chemistry 165, 108436. http://doi.org/10.1016/j.radphyschem.2019.108436

Majgier, R., Rääf, C.L., Mandowski, A., Bernhardsson, C., 2019. OSL properties in various forms of KCl and NaCl samples after exposure to ionizing radiation. Radiation Protection Dosimetry 184, 90-97. http://doi.org/10.1093/rpd/ncy189

Waldner, L., Bernhardsson, C., 2018. Physical and dosimetric properties of NaCl pellets made in-house for the use in prospective optically stimulated luminescence dosimetry applications. Radiation Measurements 119, 52-57. http://doi.org/10.1016/j.radmeas.2018.09.001

Beyond quartz and K-feldspar: non-traditional minerals

- almandine and kyanite

del Río, I., Sawakuchi, A.O., Giordano, D., Mineli, T.D., Nogueira, L., Abede, T., Atencio, D., 2019. Athermal stability, bleaching behavior and dose response of luminescence signals from almandine and kyanite. Ancient TL 37, 11-21. http://ancienttl.org/ATL_37-1_2019/ATL_37-1_delRio_p11-1.pdf

- flint

Schmidt, C., Anghelinu, M., Hambach, U., Veres, D., Lehmkuhl, F., 2020. Reassessing the timeframe of Upper Palaeolithic deposits in the Ceahlău Basin (Eastern Carpathians, Romania): Geochronological and archaeological implications. Quaternary Geochronology 55, 101020. http://doi.org/10.1016/j.quageo.2019.101020

Strebler, D., Brill, D., Richter, J., Brückner, H., 2019. Using DRAC in complex geometries - TL dating of heated flints from Taibeh, Jordan. Quaternary Geochronology 49, 4-7. http://doi.org/10.1016/j.quageo.2018.07.002

Instruments

Autzen, M., Poolton, N.R.J., Murray, A.S., Kook, M., Buylaert, J.P., 2019. A new automated system for combined luminescence and exo-electron measurements. Nuclear Instruments and Methods in Physics Research Section B: Beam Interactions with Materials and Atoms 443, 90-99. http://doi.org/10.1016/j.nimb.2019.01.030

Drew, S.M., Gross, D.S., Hollingsworth, W.E., Baraniak, T., Zall, C.M., Mann, K.R., 2019. Overdriven pulsed light emitting diodes: An inexpensive excitation source for time-resolved luminescence lifetime measurements. Journal of Chemical Education 96, 1046-1050. http://doi.org/10.1021/acs.jchemed.8b01024

França, L.V.S., Oliveira, L.C., Baffa, O., 2019. Development of a thermoluminescence and radioluminescence integrated spectrometer. Measurement 134, 492-499. http://doi.org/10.1016/j.measurement.2018.10.101

Pawlyta, J., Tudyka, K., Bluszcz, A., Adamiec, G., 2019. A method of testing the uniformity of planar radioactive α and β sources used in luminescence readers. Radiation Measurements 129, 106201. http://doi.org/10.1016/j.radmeas.2019.106201

Prajapati, M.K., Singh, U., 2018. Theoretical study of laser stimulated thermoluminescence using CO2 laser. International Journal of Current Engineering And Scientific Research 5, 456-459. http://troindia.in/journal/ijcesr/vol5iss1part2/456-459.pdf

- portable instruments

Lichtenberger, A., Raja, R., Seland, E.H., Kinnaird, T., Simpson, I.A., 2019. Urban-Riverine Hinterland Synergies in Semi-Arid Environments: Millennial-Scale Change, Adaptations, and Environmental Responses at Gerasa/Jerash. Journal of Field Archaeology 44, 333-351. http://doi.org/10.1080/00934690.2019.1625619

Porat, N., López, G.I., Lensky, N., Elinson, R., Avni, Y., Elgart-Sharon, Y., Faershtein, G., Gadot, Y., 2019. Using portable OSL reader to obtain a time scale for soil accumulation and erosion in archaeological terraces, the Judean Highlands, Israel. Quaternary Geochronology 49, 65-70. http://doi.org/10.1016/j.quageo.2018.04.001

Rodrigues, A.L., Dias, M.I., Valera, A.C., Rocha, F., Prudêncio, M.I., Marques, R., Cardoso, G., Russo, D., 2019. Geochemistry, luminescence and innovative dose rate determination of a Chalcolithic calcite-rich negative feature. Journal of Archaeological Science: Reports 26, 101887. http://doi.org/10.1016/j.jasrep.2019.101887

Stone, A., Bateman, M.D., Burrough, S.L., Garzanti, E., Limonta, M., Radeff, G., Telfer, M.W., 2019. Using a portable luminescence reader for rapid age assessment of aeolian sediments for reconstructing dunefield landscape evolution in southern Africa. Quaternary Geochronology 49, 57-64. http://doi.org/10.1016/j.quageo.2018.03.002

Turner, S., Bolòs, J., Kinnaird, T., 2018. Changes and continuities in a Mediterranean landscape: a new interdisciplinary approach to understanding historic character in western Catalonia. Landscape Research 43, 922-938. http://doi.org/10.1080/01426397.2017.1386778

Computer coding

Codilean, A.T., Munack, H., Cohen, T.J., Saktura, W.M., Gray, A., Mudd, S.M., 2018. OCTOPUS: an open cosmogenic isotope and luminescence database. Earth System Science Data 10, 2123-2139. http://doi.org/10.5194/essd-10-2123-2018

Philippe, A., Guérin, G., Kreutzer, S., 2019. BayLum - An R package for Bayesian analysis of OSL ages: An introduction. Quaternary Geochronology 49, 16-24. http://doi.org/10.1016/j.quageo.2018.05.009

Strebler, D., Riedesel, S., King, G., Brill, D., Brückner, H., 2019. LumReader: Designing your luminescence experiment with R. Radiation Measurements 129, 106143. http://doi.org/10.1016/j.radmeas.2019.106143

Review

Chamberlain, E.L., Wallinga, J., 2019. Seeking enlightenment of fluvial sediment pathways by optically stimulated luminescence signal bleaching of river sediments and deltaic deposits. Earth Surface Dynamics 7, 723-736. http://doi.org/10.5194/esurf-7-723-2019

Smedley, R.K., Skirrow, G.K.A., 2020. Luminescence Dating in Fluvial Settings: Overcoming the Challenge of Partial Bleaching, in: Herget, J., Fontana, A. (Eds.), Palaeohydrology: Traces, Tracks and Trails of Extreme Events. Springer International Publishing, Cham, pp. 155-168. http://doi.org/10.1007/978-3-030-23315-0_8

Urbanová, P., 2019. Luminescence dating of mortars by "single grain" procedure and its potential for building archaeology, in: Vecchiattini, R. (Ed.), Archeologia dell'Architettura, XXIV, 2019 – La datazione delle malte in architettura tra archeologia e archeometria. All'Insegna del Giglio, pp. 81-96. www.insegnadelgiglio.it

Books

Handbook of Luminescence Dating. Edited by Mark D. Bateman. Whittles Publishing. 416pp. 2019. ISBN 978-184995-395-5

Conference Announcements: JpGU-AGU 2020

2020 JpGU-AGU Joint Meeting: Trapped-charge Dating Session

JpGU AGU2020
24–28 MAY
CHIBA, JAPAN

JpGU - AGU Joint Meeting 2020
For a Borderless World of Geoscience
Japan Geoscience Union, American Geophysical Union
24-28 MAY 2020
Makuhari Messe, Chiba, Japan

Session : **Innovative Applications of Trapped-Charge Dating to Quaternary Geochronology**

Abstract Deadline : **18 February, 2020**

Session Date: 27 May 2020

Convener: Toru Tamura, Shin Toyoda, Yuji Ishii, Sumiko Tsukamoto

Conference webpage : http://www.jpgu.org/meeting_j2020/

Session abstract:
Trapped-Charge Dating (TCD) is a general term for absolute dating methods that use trapped electrons in crystal lattice, such as optically-stimulated luminescence (OSL) and electron spin resonance (ESR) dating. TCD presented one of the most successful progresses in geoscience and archaeology over the last 20 years, and still has a great potential in innovative applications. Technical progresses in optical dating of quartz and feldspar grains enables determination of depositional ages in a broad range from 10 to 500,000 years. Rock surface dating provides a way to determine surface exposure ages as well as burial ages of gravels. Thermochronometry with TCD is a state of the art method to determine the degradation and uplift rates on high temporal resolution. Further efforts have been made on TCD for extracting chronological information of past seismic activities. Innovative IRPL (infrared photoluminescence) method has also recently been invented. This session covers a wide range of TCD applications to problems in Quaternary geochronology as well as its technical advances. Comprehensive reviews on successful TCD applications and contributions of unestablished, challenging researches are also welcome.

For further details please contact Toru Tamura (toru.tamura@aist.go.jp)

Conference Announcements: ISA 2020

43rd International Symposium on Archaeometry (ISA 2020)

The 43rd International Symposium on Archaeometry (ISA 2020) will be held in Lisbon, Portugal, from May 18 to May 22, 2020, organized by Instituto Superior Técnico. Universidade de Lisboa.

The aim of the Symposium is to promote the development and use of scientific techniques, for the extraction of archaeological and historical information from the cultural heritage and the paleoenvironment.

Date: 18th to 22nd May 2020
Location: IST, Congress Centre, Lisbon (Portugal)

For more information visit the webpage
https://www.isa2020-lisboa.pt/index.php

or contact
isa2020@isa2020-lisboa.pt

Conference Announcements: NWLDW 2021

2021 New World Luminescence Dating Workshop

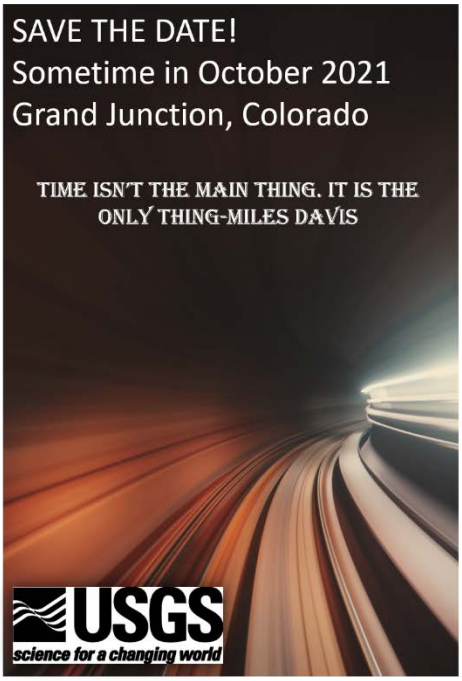

For more information please contact

Shannon Mahan (smahan@usgs.gov)
or
Harrison Gray (hgray@usgs.gov)

Book Announcements: Handbook of Luminescence Dating

Note: Ancient TL does not endorse this product nor encourage readers to buy the book. However, we realize it will be a useful and interesting product to many in the luminescence and ESR community.

Information from the publisher:

Book Announcements: Whittles Publishing
www.whittlespublishing.com

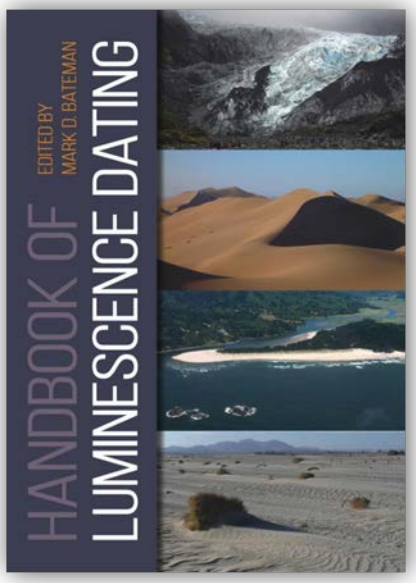

Handbook of Luminescence Dating

Edited by Mark D. Bateman

- An accessible guide for archaeologists and Quaternary scientists and geologists
- In depth explanations of challenges and issues arising from applying luminescence dating in specific environmental and archaeological contexts
- Fully illustrated case studies show the range of approaches adopted and the reliability and precision of resultant ages
- Provides guidance on interpreting luminescence ages and using them in chronological frameworks

Contents: Principles and history of luminescence dating; From sampling to reporting; Incorporating luminescence ages into chronometric frameworks; Applications in aeolian environments; Applications in loessic environments; Applications in glacial and periglacial environments; Applications in fluvial and hillslope environments; Applications in coastal and marine environments; Applications of luminescence dating to active tectonic contexts; Applications in archaeological contexts; Rock surface burial and exposure dating; Future developments in luminescence dating

ISBN 978-184995-395-5 240 x 170mm 416pp over 130 photographs, diagrams, charts, etc.
colour throughout hardback £90

Full information is available at
http://www.whittlespublishing.com/Handbook_of_Luminescence_Dating

Announcements: Inter-Laboratory Comparison

Inter-laboratory comparison to measure the elemental concentration or specific activity of uranium, radium, thorium and potassium in sediment

Various OSL labs in the New World luminescence dating community have recently decided to perform a small inter-laboratory comparison, specifically to measure the element concentration of uranium, radium, thorium and potassium in sediment. The measurement can be any desired method: ICP-MS, XRF, gamma spectrometry, alpha or beta counting, or atomic emissions (flame photometer). We just need as many labs to participate as possible so we can see the wide range of precision and accuracy for a natural sample. We would like to keep the project open to other labs in North and South America, as well as around the World for participation. Simply raise your hand to let us know your interest!

As we are all aware, the last wide-scale inter-lab comparison (Murray et al., 2015) ended on a perplexing note: the measurement of the equivalent dose had good reproducibility between labs, with an average relative standard error (RSE) between 2 and 3 %. Unexpectedly, however, the (simple) measurement of uranium, radium, thorium and potassium was far more dispersed, ranging from 3 to 13 % RSE. Perhaps this was a sign that we have neglected the bottom half of the age equation for too long! The only way to revolve this is to repeat the exercise, with the hope of identifying something that we have neglected.

We have recently retrieved two buckets of sand from a Colorado River terrace at a quarry in Grand Junction (Colorado) USA. Our purpose in collecting this massive, naturally homogenized, silty sand was two-fold: A larger aim will be to return to that quarry next year for an inter-laboratory comparison with portable gamma spectrometers at a natural site that we can all access and a secondary aim is to collect some of this sand and standardize it at the USGS Reference Sediment Laboratory for distribution to all that would like to measure the K, U, and Th activities or elements. The sample would be split, processed, and bottled at the USGS Reference Laboratory with QA/QC procedures. We anticipate producing about 200 uniquely numbered bottles of approximately 200 g of sample which would go out to labs that expressed an interest in helping the community study. If there is sufficient interest, then the sample will be measured by a certified laboratory (perhaps several?). This would provide us with an independent base of reference to which we can objectively compare our individual performance against. We plan to present the results, anonymized, in the LED2020 meeting.

For the labs in North America, Grand Junction is of great interest because for the past 40 years the US Department of Energy has maintained various horizontal pads and vertical wells for the purpose of calibration of portable gamma detectors. Earlier this autumn, we united five laboratories at this site, during the same weekend. Due to unforeseen reasons, we could not access the quarry during that weekend, sadly, but in the future we plan to hold community calibrations there as well. After a hard day of calibration, we can retire to several nearby vineyards to discuss the science.

Coordinators: Sebastien Huot shuot@illinois.edu and Shannon Mahan smahan@usgs.gov

Murray, A., Buylaert, J.-P., Thiel, C., 2015. A luminescence dating intercomparison based on a Danish beach-ridge sand. Radiation Measurements 81, 32-38. http://doi.org/10.1016/j.radmeas.2015.02.012

Announcements: Various Ancient TL matters

Ancient TL adopts the Creative Commons Attribution 4.0 License

Starting with the current issue (Vol. 37, No. 2) Ancient TL articles are published under the **Creative Commons Attribution 4.0 License**. By submitting a manuscript authors automatically agree that their article is distributed under the Creative Commons Attribution 4.0 License. More information can be found under

https://creativecommons.org/licenses/by/4.0/

or

ancienttl.org

New Databases for measurement procedures and calibration sites

In summer 2019 Ancient TL made available an overview of freely available tools for trapped charge (dating) data analysis (see http://ancienttl.org/software.htm). Our goal is to add to this service by adding two new databases

1. ***A collection of calibration sites for dosimetry measurements*:** Portable gamma spectrometers and other dosimetry methods need to be calibrated on a regular basis, but information about suitable sites is usually spread by word of mouth. Goal is to list calibration sites by continent and to make available pertinent information to any interested user. This can include anything from government provided calibration pads, to field sites, to brick stacks in a laboratory.
2. ***A list of measurement procedures*:** The number of measurement procedures for quartz, feldspar and other minerals is growing by the months and it is increasingly difficult to keep track. Review articles are quickly outdated. Our goal is to provide an overview of different measurement procedures starting from MAAD, SARA and SAR to IRPL

The software was compiled and is updated by Sebastian Kreutzer. **Ancient TL is looking for volunteers to help in a similar way with the two lists above.**
Please contact Regina DeWitt (dewittr@ecu.edu) for more information.

Ancient TL

ISSN 0735-1348

Aims and Scope

Ancient TL is a journal devoted to Luminescence dating, Electron Spin Resonance (ESR) dating, and related techniques. It aims to publish papers dealing with experimental and theoretical results in this field, with a minimum of delay between submission and publication. Ancient TL also publishes a current bibliography, thesis abstracts, letters, and miscellaneous information, e.g., announcements for meetings.

Frequency

Two issues per annum in June and December

Submission of articles to Ancient TL

Ancient TL has a reviewing system in which direct dialogue is encouraged between reviewers and authors. For instructions to authors and information on how to submit to Ancient TL, please visit the website at:
http://ancienttl.org/TOC1.htm

Journal Enquiries

For enquiries please contact the editor:
Regina DeWitt, Department of Physics, East Carolina University, Howell Science Complex, 1000 E. 5th Street, Greenville, NC 27858, USA; Tel: +252-328-4980; Fax: +252-328-0753 (dewittr@ecu.edu)

Subscriptions to Ancient TL

Ancient TL Vol. 32 No.2 December 2014 was the last issue to be published in print. Past and current issues are available for download free of charge from the Ancient TL website:
http://ancienttl.org/TOC4.htm